

# Bandgap optimization in locally resonant metamaterial plates: A comparative study of five lattice geometries for low-frequency wave attenuation

A.H.R. Ferreira<sup>a,\*</sup>, E.J.P. Miranda Jr.<sup>b,c,d</sup>, J.M.C. Dos Santos<sup>a</sup>, A.M. Goto<sup>a</sup>

<sup>a</sup> University of Campinas, UNICAMP-FEM-DMC, Rua Mendeleyev, 200, CEP 13083-970, Campinas, SP, Brazil

<sup>b</sup> Federal Institute of Maranhão, IFMA-PPGEM, CEP 65030-005, São Luís, MA, Brazil

<sup>c</sup> Federal Institute of Maranhão, IFMA-EIB-DE, CEP 65010-030, São Luís, MA, Brazil

<sup>d</sup> Vale Institute of Technology, ITV-MI, CEP 35400-000, Ouro Preto, MG, Brazil

---

## Abstract



The attenuation of low-frequency flexural waves (10 – 200)[Hz] represents a persistent challenge in structural engineering, requiring innovative solutions that balance efficiency, compactness, and weight constraints. This study presents the first systematic comparative analysis investigating the combined influence of lattice geometry and local resonator frequency on band gap formation in thin Kirchhoff-Love plates across five distinct periodic configurations. The primary objective is to establish quantitative design guidelines for optimal lattice-resonator arrangements in the critical low-frequency range for aerospace, automotive, and civil engineering applications.

A comprehensive framework combining semi-analytical Plane Wave Expansion (PWE) and Extended Plane Wave Expansion (EPWE) methods with Finite Element Method (FEM) validation systematically analyzes 15 resonator frequencies across square, rectangular, triangular, honeycomb, and kagomé lattice configu-

---

\*Corresponding author. Tel.: +55 11 958509690  
Email address: [a058899@dac.unicamp.br](mailto:a058899@dac.unicamp.br) (A.H.R. Ferreira)

rations. The semi-analytical approach demonstrates computational efficiency improvements of two orders of magnitude over conventional FEM while maintaining accuracy within 5% of numerical predictions.

Quantitative analysis reveals distinct performance hierarchies: triangular lattices achieve 35% superior relative bandwidth compared to square configurations (42.51% vs 31.40%) and demonstrate superior broadband characteristics; kagomé lattices provide up to 15 [dB] enhanced attenuation at low frequencies through triple-resonator coupling; honeycomb configurations offer balanced dual-band gap performance with coexisting frequency regions. A critical finding is the observation of two distinct complete band gaps in multi-resonator systems (honeycomb and kagomé), arising from in-phase and anti-phase resonator coupling modes, contrasting with single band gap behavior in single-resonator lattices (square, rectangular, triangular). Comprehensive bandwidth evolution analysis across all five lattice geometries establishes frequency-dependent performance maps for systematic design optimization. Bandwidth analysis employs infinite unit cell model predictions obtained through PWE/EPWE formulations. Finite plates consistently exhibit 40 – 50% bandwidth expansion beyond infinite domain predictions due to boundary-induced mode coupling effects.

The research establishes the first quantitative hierarchy of lattice performance and provides engineers with systematic design guidelines for metamaterial plate optimization. This framework advances the field by bridging theoretical band gap predictions with practical finite plate performance, establishing essential tools for next-generation lightweight vibration isolation systems requiring efficient frequency-targeted vibration control.

*Keywords:* Locally resonant metamaterial, Flexural waves, Band gaps, Lattice configurations, Semi analytical method, Frequency-dependent optimization, Low-frequency vibration control.

---

<sup>1</sup> **1. Introduction**

<sup>2</sup> Low-frequency noise and vibration mitigation represents a fundamental chal-  
<sup>3</sup> lenge in modern engineering applications, particularly within civil, naval, auto-  
<sup>4</sup> motive and aerospace systems [1–7]. Structures exposed to mechanical waves  
<sup>5</sup> in the 20 [Hz] to 200 [Hz] range—including aircraft fuselages, vehicle cabins, in-  
<sup>6</sup> dustrial machinery, and building floors—frequently experience unwanted reso-  
<sup>7</sup> nances and excessive structural vibrations [8, 9]. These phenomena precipitate  
<sup>8</sup> substantial economic and operational consequences: material fatigue reduces  
<sup>9</sup> component lifespans by 25-40% in aerospace applications, excessive vibrations  
<sup>10</sup> decrease industrial machinery efficiency by up to 15%, and noise-induced com-  
<sup>11</sup> fort degradation costs the aviation industry approximately \$3.2 billion annually  
<sup>12</sup> in passenger compensation and operational delays [10, 11].

<sup>13</sup> Traditional passive noise control approaches, such as mass-damping systems  
<sup>14</sup> or viscoelastic coatings, impose severe design penalties: typical solutions re-  
<sup>15</sup> quire 150-300% mass increases to achieve 20 [dB] attenuation in the 20-200  
<sup>16</sup> [Hz] range, rendering them impractical for weight-sensitive applications where  
<sup>17</sup> every kilogram costs \$10,000-15,000 per flight hour in commercial aviation. Fur-  
<sup>18</sup> thermore, conventional treatments occupy 40-60% additional structural volume,  
<sup>19</sup> compromising payload capacity and architectural design flexibility [12–15]. Con-  
<sup>20</sup> sequently, the development of advanced acoustic metamaterials with tailored  
<sup>21</sup> bandgap properties has emerged as a critical technological imperative for achiev-  
<sup>22</sup> ing effective wave attenuation while maintaining compact, lightweight designs  
<sup>23</sup> that preserve operational performance and economic viability.

<sup>24</sup> The conceptual foundations of wave propagation control in structured materi-  
<sup>25</sup> als trace back to pioneering developments in photonics during the late 1980s.  
<sup>26</sup> The seminal works of Yablonovitch and John in 1987 [16, 17] introduced the  
<sup>27</sup> revolutionary concept of photonic band gaps (PBGs) in periodic dielectric me-  
<sup>28</sup> dia, establishing the theoretical framework for electromagnetic wave manipula-  
<sup>29</sup> tion. This breakthrough catalyzed rapid theoretical and experimental advances:

30 Meade et al. [18] provided the first theoretical demonstration of two-dimensional  
31 PBGs, while Villeneuve and Piché [19] analyzed band-gap formation in square  
32 and hexagonal lattices. The consolidation of this progress culminated in the pa-  
33 per by Joannopoulos [20], which demonstrated controlled electromagnetic wave  
34 manipulation in photonic crystals with immediate practical impact.

35 Inspired by these photonic developments, the early 1990s witnessed the emer-  
36 gence of phononics as researchers began investigating analogous concepts for  
37 mechanical wave control in elastic media. Sigalas and Economou [21] provided  
38 the first definitive demonstration of elastic-wave band gaps in two-dimensional  
39 periodic systems in 1992, followed by Kushwaha et al. [22], who developed the  
40 foundational theoretical framework for acoustic band structures in periodic elas-  
41 tic composites. These pioneering contributions established the principles that  
42 would guide subsequent phononic crystal research [23].

43 Phononic crystals (PCs) emerged as artificial structures composed of periodic  
44 arrangements of materials with contrasting mechanical properties, typically in-  
45 volving inclusions embedded in a host matrix. This concept, formalized in  
46 the late 1990s by Laude and collaborators [24, 25], operates through Bragg  
47 scattering mechanisms that restrict wave propagation within specific frequency  
48 bands—termed band gaps—when the structural periodicity approaches half the  
49 wavelength [22, 23]. The theoretical foundation draws from classical works by  
50 Floquet [26], Bloch [27], and Brillouin [28], later consolidated through compre-  
51 hensive reviews [29, 30].

52 Despite their effectiveness, PCs face a fundamental limitation for low-frequency  
53 applications: Bragg’s condition  $a = n\lambda/2$  necessitates large unit cells to attem-  
54 iate low-frequency waves [30], challenging compact device design, particularly  
55 for flexural [31] or elastic waves in complex media [32]. However, locally reso-  
56 nant sonic crystals (LRSCs) overcome this limitation by utilizing internal res-  
57 onances rather than pure Bragg scattering, enabling subwavelength operation  
58 where resonator-induced band gaps can occur even when  $a \ll \lambda/2$ . While Bragg

59 effects may contribute to observed band gaps in this study, the primary mechanism  
60 is local resonance coupling, distinguishing our approach from traditional  
61 phononic crystals that rely exclusively on geometric periodicity.

62 The paradigm shift toward subwavelength metamaterials began with Liu et al.'s  
63 [33] groundbreaking proposal of **Locally Resonant Sonic Crystals (LRSCs)**. Unlike  
64 conventional PCs that rely on interference, LRSCs utilize internal resonances  
65 to form band gaps at subwavelength scales, enabling lattice constants  
66 two orders of magnitude smaller than the acoustic wavelength while achieving  
67 deep low-frequency attenuation in compact structures.

68 Subsequent research rapidly expanded and validated this concept across multiple  
69 domains. Wang et al. demonstrated subwavelength band gaps in 2D soft-  
70 inclusion composites [34] and extended the concept to 1D harmonic oscillator  
71 systems, revealing that stiffness contrast governs attenuation depth [35]. Hsu et  
72 al. [36] showed that Lamb wave band gaps in thin plates depend strongly on in-  
73 clusion radius and thickness, while Oudich and colleagues explored waveguiding  
74 in curved and straight channels [37] and experimentally confirmed complete out-  
75 of-plane Lamb wave band gaps in stubbed plates using Brillouin spectroscopy  
76 and laser vibrometry [38].

77 The theoretical analysis of wave propagation in metamaterial plates has evolved  
78 through significant contributions to classical plate theory. The Kirchhoff–Love  
79 and Mindlin–Reissner theories—originally formulated by Kirchhoff [39], Love  
80 [40], Mindlin [41], and Reissner [42]—provide the foundation for understanding  
81 flexural wave propagation in thin and moderately thick plates. Advanced numerical  
82 methods, including the Plane Wave Expansion (PWE) approach [43] and its  
83 Extended version (EPWE) [44, 45], enable accurate band structure predictions  
84 in complex periodic systems.

85 Building upon these developments, Xiao et al. investigated flexural wave prop-  
86 agation in thin plates with periodic spring–mass resonators using EPWE [46],  
87 revealing the coexistence of Bragg-type and locally resonant gaps, as well as

wide pseudo-gaps dependent on resonator natural frequency. Critically, their work demonstrated that the widest bandgap occurs when the directional resonance band gap and Bragg band gap are nearly coupled, and they provided an approximate initial design formula for achieving such optimal coupling conditions. This coupling mechanism enables the formation of super-wide pseudo-directional gaps through the combination of resonance and Bragg effects, with the bandwidth being dramatically affected by the resonant frequency of local resonators. Their subsequent work demonstrated that beam-like resonators periodically attached to plates can induce low-frequency complete band gaps for flexural waves [47], with tunable resonator properties allowing significant control over band gap location and width.

Recent advances have further refined our understanding of metamaterial plate behavior. Miranda et al. analyzed multi-DOF resonator arrays using PWE validated with finite element simulations (FEM) and experiments [48], revealing similar attenuation levels for square and triangular lattices, though square configurations exhibited wider Bragg-type gaps. Their extension to thick plates with spring-mass resonators, applying Mindlin-Reissner theory through combined analytical, numerical, and experimental methods [49], confirmed simultaneous formation of locally resonant and Bragg-type band gaps, further validating LRSCs as robust platforms for vibration attenuation.

The practical implementation of metamaterial concepts has yielded numerous engineering applications. Flexural wave control in thin plates, demonstrated by Lee and Ruzzene [50] and Yao et al. [51], has found significant relevance in aerospace and automotive industries. Metamaterial barriers for vibration and acoustic isolation have advanced through studies like Zouari et al. [52], while acoustic panels for architectural acoustics were developed by Wang et al. [53]. The integration of multiple physical phenomena—including piezoelectric effects for active control [54] and adaptive metamaterials with embedded shunt circuits [55]—has opened new possibilities for smart, adaptive metamaterial systems.

117 Advanced design strategies have further enhanced metamaterial performance.  
118 Fractal-based phononic structures, such as hierarchical porous designs by Lee  
119 and Jeon [56], demonstrated that multi-level geometries can open multiple and  
120 widened band gaps. Auxetic microstructured metamaterials have shown novel  
121 wave-control mechanisms [57], while embedding multiple local resonators within  
122 unit cells has proven effective [58]. Divergent-shaped unit cells, such as star-  
123 shaped configurations [59], have demonstrated low-frequency, wide band-gap  
124 behavior, with viscoelastic damping layers further broadening performance [58].

125 Recent investigations have explored the relationship between lattice geometry  
126 and attenuation performance. Wang et al. [60] investigated sandwich plate  
127 structures with periodically embedded plate-type resonators, demonstrating sig-  
128 nificant sound transmission loss, while Yan et al. [61] employed geometry op-  
129 timization to design diverse lattice configurations for enhanced low-frequency  
130 vibration attenuation. The influence of resonator design on band-gap formation  
131 has been extensively studied through impedance mismatch effects [62], modal  
132 coupling influences, and multilayer resonator arrangements [63]. Building upon  
133 the foundational work of Xiao et al. [46], who established the critical role of  
134 resonator frequency tuning in achieving optimal resonance-Bragg coupling con-  
135 ditions, these studies have revealed critical design parameters for attenuation  
136 performance.

137 Building upon these extensive developments, this study addresses the challenge  
138 of low-frequency noise and vibration control by presenting the first systematic  
139 comparative analysis of the elastic band structure of flexural waves in infinite pe-  
140 riodic plates with five distinct lattice configurations. The research is motivated  
141 by the critical need to quantify design trade-offs: while metamaterial solutions  
142 can achieve 20-40 [dB] attenuation with only 5-15% mass penalties (compared  
143 to 150-300% for conventional approaches), optimal lattice selection remains em-  
144 pirical, leading to suboptimal performance and missed opportunities for weight  
145 and cost savings potentially worth millions of dollars in large-scale applications.

146 The investigation examines single-degree-of-freedom (SDOF) local resonator sys-  
147 tems (SR-SDOF) arranged in square, rectangular, and triangular lattices, as  
148 well as multiple local resonator systems (MR-SDOF) in honeycomb and kagomé  
149 lattices. These five geometries represent the fundamental design space for  
150 2D lattice metamaterials: square and rectangular lattices establish the base-  
151 line orthogonal configurations commonly employed in manufacturing; triangu-  
152 lar lattices provide the highest symmetry achievable with single resonators per  
153 unit cell; honeycomb configurations introduce the simplest dual-resonator ar-  
154 chitecture with practical manufacturability; and kagomé lattices represent the  
155 most complex **multi-resonator** arrangement feasible within standard fabrica-  
156 tion constraints. This selection encompasses the full spectrum from simple  
157 (manufacturing-friendly) to complex (performance-optimized) configurations, en-  
158 abling systematic evaluation of the geometry-performance-complexity trade-offs  
159 critical for engineering implementation.

160 The comprehensive analysis employs both semi-analytical methods (PWE and  
161 EPWE) and numerical simulations (FEM), demonstrating computational effi-  
162 ciency improvements of two orders of magnitude while establishing quantitative  
163 performance hierarchies among lattice configurations. This work provides crit-  
164 ical insights into the dual influence of lattice geometry and resonator tuning,  
165 enabling data-driven design decisions that can reduce development time by 60-  
166 80% compared to trial-and-error approaches, while ensuring optimal solutions  
167 for specific application requirements in weight-sensitive and performance-critical  
168 engineering systems.

169 This paper is structured as follows: Section 2 presents the PWE approach for  
170 periodic plates based on Kirchhoff-Love theory, detailing the mathematical for-  
171 mulation for five lattice types (square, rectangular, triangular, honeycomb, and  
172 kagomé) with spring-mass resonators, including the derivation of eigenvalue  
173 problems and dispersion relations. Section 3 analyzes structure bands for 15 lo-  
174 cal resonance frequency values ranging from 30 [Hz] to 200 [Hz], systematically  
175 comparing band gap widths, attenuation depths, and frequency evolution across

176 all lattice configurations, while identifying critical performance metrics such as  
177 the triangular lattice's superior broadband performance and the kagomé's ex-  
178 ceptional low-frequency attenuation. Section 4 validates the semi-analytical  
179 predictions through finite element simulations of  $10 \times 10$  unit cell plates under  
180 point force excitation, comparing receptance curves and transmission loss to  
181 demonstrate the correlation between infinite-domain band structures and finite-  
182 plate vibration attenuation. Conclusions are presented in Section 5, synthesiz-  
183 ing the quantitative design guidelines and performance hierarchies discovered.  
184 Appendix A and Appendix B provide the complete matrix formulations for  
185 PWE and EPWE implementations, including reciprocal lattice vectors, Fourier  
186 coefficients, and computational algorithms for complex wave vector extraction.  
187 Appendix C extends the analysis to metallic and composite materials (alu-  
188 minum and carbon/epoxy), demonstrating the universality of geometric perfor-  
189 mance principles across materials with  $150\times$  stiffness variation. Appendix D  
190 presents a comprehensive framework for lattice selection in engineering appli-  
191 cations, providing quantitative decision tables and application-specific design  
192 guidelines derived from the comparative analysis.

## 193 2. Formulating LRSC unit cell models

194 This section presents a comprehensive formulation for thin LRSC plates using  
195 semi-analytical PWE and EPWE methods, based on Kirchhoff-Love plate theory  
196 [40].

### 197 2.1. Theoretical foundations

198 LRSC plates are modeled using Kirchhoff-Love theory for thin plates ( $h/a < 0.1$ )  
199 with spring-mass resonators providing local resonance effects (Figure 1).

200 This classical theory assumes plane sections remain plane and perpendicular  
201 to the neutral surface during bending, neglecting transverse shear deformation  
202 and rotatory inertia effects. The theory is valid when the plate thickness is  
203 much smaller than the characteristic wavelength, ensuring that flexural wave

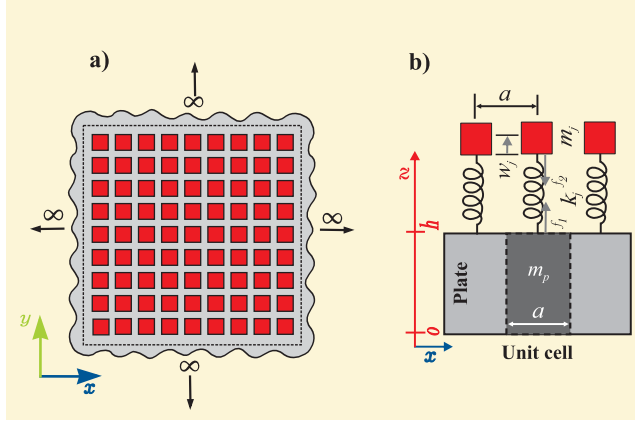


Figure 1: LRSC metamaterial configuration: (a) Infinite periodic array showing the global structure with spring-mass resonators (red squares) attached to the host plate. The dashed lines indicate the unit cell boundaries. (b) Detailed view of a single unit cell showing: plate mass  $m_p$ , resonator parameters ( $m_{r,j}$ ,  $k_j$ ,  $f_j$ ), geometric dimensions ( $a$ ,  $h$ ), and coordinate system. The resonators provide local resonance at frequency  $f_j = (2\pi^{-1})\sqrt{k_j/m_{r,j}}$ .

propagation is governed by the plate's bending stiffness rather than shear effects.  
 The governing equation for flexural vibration with periodic resonator coupling  
 is:

$$D\nabla^4 w(\mathbf{r}) - \omega^2 \rho h w(\mathbf{r}) = \sum_{j=1}^{N_j} \sum_{\mathbf{R}} p_j(\mathbf{r}_j + \mathbf{R}) \delta[\mathbf{r} - (\mathbf{r}_j + \mathbf{R})], \quad (1)$$

where  $D = E^* h^3 / [12(1 - \nu^2)]$  is the complex bending stiffness with  $E^* = E(1 + i\eta_p)$  being the complex Young's modulus incorporating plate damping through loss factor  $\eta_p$ ,  $\mathbf{R}$  are lattice vectors defining the periodic repetition of unit cells,  $\mathbf{r}_j$  are the positions of resonators within a unit cell, and  $N_j$  resonators per unit cell. Resonator-plate coupling follows:

$$p_j(\mathbf{r}_j + \mathbf{R}) = k_j^* [u_j(\mathbf{r}_j + \mathbf{R}) - w(\mathbf{r}_j + \mathbf{R})], \quad (2)$$

$$-\omega^2 m_{r,j} u_j(\mathbf{r}_j + \mathbf{R}) = -p_j(\mathbf{r}_j + \mathbf{R}), \quad (3)$$

where  $u_j(\mathbf{r}_j + \mathbf{R})$  is the displacement of the  $j$ th resonator mass and  $w(\mathbf{r}_j + \mathbf{R})$

<sup>214</sup> is the flexural displacement of the plate at the resonator attachment point. The  
<sup>215</sup> complex stiffness  $k_j^* = k_j(1 + i\eta_j)$  incorporates the resonator damping effect.

<sup>216</sup> Eliminating the resonator displacement  $u_j$  from equations (2) and (3) yields the  
<sup>217</sup> resonator coupling force:

$$p_j(\mathbf{r}_j + \mathbf{R}) = \frac{-k_j^*\omega^2}{\omega^2 - \omega_{j,0}^2(1 + i\eta_j)} w(\mathbf{r}_j + \mathbf{R}) \quad (4)$$

<sup>218</sup> where  $\omega_{j,0} = \sqrt{k_j/m_{r,j}}$  is the natural resonator frequency. Substituting this cou-  
<sup>219</sup> pling into equation (1) and applying periodic Floquet-Bloch conditions trans-  
<sup>220</sup> forms the partial differential equation into a matrix eigenvalue problem via  
<sup>221</sup> reciprocal space expansion, as detailed in the following sections.

<sup>222</sup> The plane wave truncation parameter  $M$  in the expansion  $(2M+1)^2$  determines  
<sup>223</sup> the computational accuracy of the PWE method. Based on established practices  
<sup>224</sup> for similar phononic crystal analyses [43, 45], this study employs  $M = 5$  for  
<sup>225</sup> single-resonator and multi-resonator cases in the frequency range 10-200 [Hz]  
<sup>226</sup> with lattice parameter  $a = 0.10$  m, ensuring wavelength resolution  $\lambda/a > 5$  for  
<sup>227</sup> adequate spatial discretization of the wave field.

<sup>228</sup> *2.2. Semi-analytical methods overview*

<sup>229</sup> This study employs two complementary semi-analytical approaches: Plane Wave  
<sup>230</sup> Expansion (PWE) and Extended Plane Wave Expansion (EPWE). Table 1 sum-  
<sup>231</sup> marizes their key characteristics and applications.

Table 1: Comparison between PWE and EPWE methods for LRSC plate analysis.

Aspect	PWE Method	EPWE Method
Wave vector $\mathbf{k}$	Real values only	$\mathbf{k} \in \mathbb{C}, \mathbf{k} = \Re(\mathbf{k}) + i\Im(\mathbf{k})$
Evanescence modes	Ignored	Naturally incorporated
Primary application	Band structure calculation $\omega(\mathbf{k})$	Attenuation analysis $\mathbf{k}(\omega)$
Brillouin zone	Restricted to first zone	No restriction
Bandgap analysis	Identifies frequency ranges	Quantifies attenuation levels
Computational cost	Lower (eigenvalue problem)	Higher (generalized eigenvalue)
Physical insight	Propagating wave modes	Evanescence decay in bandgaps

<sup>232</sup> The combination of both methods provides complete bandgap characterization.

<sup>233</sup> PWE solves the forward eigenvalue problem:

$$[\mathbf{K} - \omega^2 \mathbf{M}] \boldsymbol{\phi} = 0, \quad \omega = \omega(\mathbf{k}) \quad (5)$$

<sup>234</sup> while EPWE solves the inverse problem for complex wave vectors:

$$[\mathbf{A}_3 k^3 + \mathbf{A}_2 k^2 + \mathbf{A}_1 k + \mathbf{A}_0] \boldsymbol{\psi} = 0, \quad k = k(\omega) \quad (6)$$

<sup>235</sup> The unit cell attenuation constant is defined as  $\mu = \text{Im}\{k\} \cdot a$  [ $Np/\text{cell}$ ], where

<sup>236</sup>  $Np$  denotes nepers (natural logarithm unit for attenuation: Attenuation [dB] =

<sup>237</sup>  $8.686 \times \mu$ ). With these analytical tools established, the following section examines how different lattice geometries influence the band structure formation and

<sup>238</sup> attenuation characteristics. 

### <sup>240</sup> 2.3. Periodic lattice configurations

<sup>241</sup> Five lattice geometries with varying resonator configurations are analyzed: square

<sup>242</sup> (1 resonator), rectangular (1), triangular (1), honeycomb (2), and kagomé (3).

<sup>243</sup> These geometries span orthogonal to complex lattice symmetries, enabling comprehensive bandgap performance evaluation.

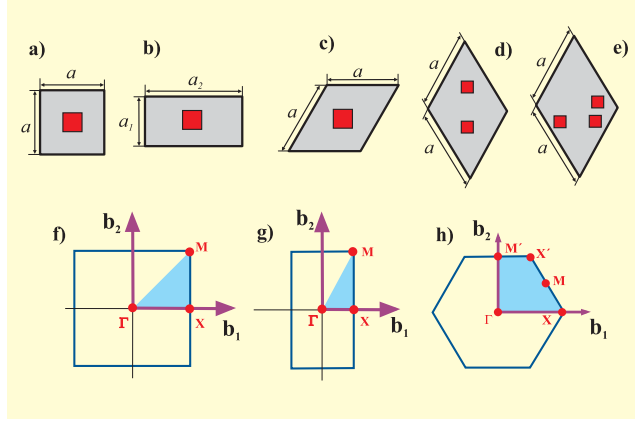


Figure 2: LRSC unit cells and FIBZ paths: (a) square, (b) rectangular, (c) triangular, (d) honeycomb, (e) kagomé lattices. Red squares: resonators. FIBZ -symmetry paths: (f) Square/Rectangular:  $\Gamma(0,0) \rightarrow X(\pi/a,0) \rightarrow M(\pi/a,\pi/a)$ . (g) Triangular/Honeycomb/Kagomé:  $M'(0,2\pi/3a) \rightarrow \Gamma(0,0) \rightarrow X(2\pi/3a,0) \rightarrow M(\pi/3a,\pi/\sqrt{3}a) \rightarrow X'(\pi/3a,\pi/\sqrt{3}a) \rightarrow M'$ .

245 Primitive lattice vectors are:  $\mathbf{a}_{1,2} = a\mathbf{e}_{1,2}$  (square),  $\mathbf{a}_{1,2} = a_{x,y}\mathbf{e}_{1,2}$  (rectangular),  
246  $\mathbf{a}_1 = a\mathbf{e}_1$  and  $\mathbf{a}_2 = a(-\frac{1}{2}\mathbf{e}_1 + \frac{\sqrt{3}}{2}\mathbf{e}_2)$  (triangular),  $\mathbf{a}_{1,2} = a\mathbf{e}_{1,2}$  (honeycomb), and  
247  $\mathbf{a}_1 = a\sqrt{3}(\mathbf{e}_1 - \frac{1}{\sqrt{3}}\mathbf{e}_2)$  and  $\mathbf{a}_2 = a\sqrt{3}(\mathbf{e}_1 + \frac{1}{\sqrt{3}}\mathbf{e}_2)$  (kagomé). Reciprocal lattice  
248 vectors follow standard crystallographic relations  $\mathbf{b}_i = 2\pi(\mathbf{a}_j \times \mathbf{e}_z)/(\mathbf{a}_i \cdot (\mathbf{a}_j \times \mathbf{e}_z))$ .

#### 249 2.4. PWE for thin LRSC unit cell thin plate configurations

250 PWE transforms the governing PDE into a matrix eigenvalue problem via  
251 Fourier expansion in reciprocal space. The displacement field follows Floquet-  
252 Bloch theorem:

$$w(\mathbf{r}) = e^{i\mathbf{k}\cdot\mathbf{r}} \sum_{\mathbf{G}} w(\mathbf{G}) e^{i\mathbf{G}\cdot\mathbf{r}} = \sum_{\mathbf{G}} w(\mathbf{G}) e^{i(\mathbf{k}+\mathbf{G})\cdot\mathbf{r}} \quad (7)$$

253 where reciprocal lattice vectors  $\mathbf{G} = m\mathbf{b}_1 + n\mathbf{b}_2$  with integers  $(m, n) \in [-M, M]$   
254 and basis vectors  $\mathbf{b}_i = (2\pi/S)(\mathbf{a}_j \times \mathbf{e}_z)$  for unit cell area  $S$ , consistent with the  
255  $(2M+1)^2$  plane wave truncation used in computational implementation.

256 Resonator displacements satisfy:

$$w(\mathbf{r}_j) = \sum_{\mathbf{G}} w(\mathbf{G}) e^{i(\mathbf{k}+\mathbf{G})\cdot\mathbf{r}_j} \quad (8)$$

<sup>257</sup> The eigenvalue problem formulation yields:

$$[\mathbf{K} - \omega^2 \mathbf{M}] \{\mathbf{q}\} = \mathbf{0} \quad (9)$$

<sup>258</sup> where  $\mathbf{K}$  and  $\mathbf{M}$  are stiffness and mass matrices, and  $\mathbf{q} = [\mathbf{w}^T, \mathbf{u}^T]^T$  contains  
<sup>259</sup> both plate wave amplitudes  $\mathbf{w} = [w(\mathbf{G}_1), \dots, w(\mathbf{G}_{N_g})]^T$  and resonator displace-  
<sup>260</sup> ments  $\mathbf{u} = [u_1, \dots, u_{N_j}]^T$ . Matrix dimension is  $[(2M+1)^2+N_j] \times [(2M+1)^2+N_j]$   
<sup>261</sup> with  $N_g = (2M+1)^2$  plane waves and  $N_j$  resonators per unit cell. Complete  
<sup>262</sup> matrix assembly algorithms are detailed in Appendix A.

<sup>263</sup> The stiffness matrix  $\mathbf{K}$  from PWE contains fourth-order plate operators  $|\mathbf{k} + \mathbf{G}|^4$   
<sup>264</sup> and resonator coupling terms that become frequency-dependent in EPWE. The  
<sup>265</sup> mass matrix  $\mathbf{M}$  contributions transform to complex dynamic stiffness expres-  
<sup>266</sup> sions  $D_j(\omega)$  in the inverse formulation. This matrix relationship enables consis-  
<sup>267</sup> tent implementation of both forward  $\omega(\mathbf{k})$  and inverse  $\mathbf{k}(\omega)$  problems using the  
<sup>268</sup> same physical parameters and geometric definitions.

### <sup>269</sup> 2.5. EPWE for thin LRSC unit cell thin plate configurations

<sup>270</sup> EPWE reformulates the eigenvalue problem to solve for complex wave vectors  
<sup>271</sup>  $\mathbf{k}(\omega)$  at prescribed frequencies, enabling direct analysis of evanescent modes  
<sup>272</sup> and wave attenuation within bandgaps. The displacement field maintains the  
<sup>273</sup> Floquet-Bloch form:

$$w(\mathbf{r}) = e^{i\mathbf{k}\cdot\mathbf{r}} \sum_{\mathbf{G}} w(\mathbf{G}) e^{i\mathbf{G}\cdot\mathbf{r}}, \quad \mathbf{k} = k_r + ik_i \quad (10)$$

<sup>274</sup> where the complex wave vector  $\mathbf{k} \in \mathbb{C}$  allows for exponentially decaying modes  
<sup>275</sup> with attenuation constant  $k_i$ .

<sup>276</sup> Resonator displacements follow the same expansion as Equation (8). Substitu-  
<sup>277</sup> tion into the governing equation yields a polynomial eigenvalue problem:

$$[\mathbf{A}_3 k^3 + \mathbf{A}_2 k^2 + \mathbf{A}_1 k + \mathbf{A}_0] \psi = 0 \quad (11)$$

<sup>278</sup> where coefficient matrices  $\mathbf{A}_i$  contain lattice geometry and resonator coupling  
<sup>279</sup> terms. The resonator dynamic stiffness incorporates frequency-dependent ef-

280 ffects:

$$D_j(\omega) = k_j^* - \frac{(k_j^*)^2}{k_j^* - \omega^2 m_{r,j}} \quad (12)$$

281 Solution via companion matrix linearization provides complex eigenvalues  $k =$   
282  $k_r + ik_i$ , where  $\text{Im}\{k\} > 0$  quantifies evanescent decay. The unit cell attenu-  
283 ation constant  $\mu = \text{Im}\{k\} \cdot a$  [Np/cell] directly measures wave attenuation  
284 within bandgaps. The polynomial eigenvalue problem is solved by transforming  
285 Eq. (11) into a generalized linear eigenvalue problem of size  $4N_g \times 4N_g$ , where  
286 eigenvector tracking ensures mode continuity across frequency. Complete matrix  
287 formulations and computational algorithms are provided in Appendix B.

288 The proposed semi-analytical methods (PWE and EPWE( $\Re(\mathbf{k})$ )) are validated  
289 using finite element method (FEM) simulations in COMSOL Multiphysics 5.6  
290 with quadratic shell elements and Floquet periodic boundary conditions. The  
291 following section presents comprehensive computational efficiency and accuracy  
292 comparisons between PWE/EPWE and FEM through detailed simulated exam-  
293 ples.

294 The semi-analytical formulation is valid under the following constraints: (i)  
295 Thin plate approximation:  $h/a < 0.1$  ensuring flexural wave dominance over  
296 shear effects; (ii) Small amplitude assumption: linear elastic response with plate  
297 displacements  $w \ll h$ ; (iii) Frequency limitations:  $\omega < \omega_c = 0.5\sqrt{D/(\rho ha^4)}$  to  
298 remain within the fundamental dispersion branch; (iv) Weak coupling regime:  
299 resonator mass ratio  $m_{r,j}/(m_p S) < 0.2$  ensuring perturbative coupling validity.  
300 These constraints ensure that the Kirchhoff-Love theory assumptions remain  
301 physically meaningful and that the plane wave expansion converges within the  
302 specified truncation limits.

303 The eigenvalue problems exhibit condition numbers  $\kappa(\mathbf{K}) < 10^{12}$  for the ana-  
304 lyzed configurations, ensuring numerical stability. The complex frequency de-  
305 pendence in EPWE requires careful pole avoidance near resonator frequencies,  
306 achieved through frequency regularization  $\omega \rightarrow \omega + i\epsilon$  with  $\epsilon = 10^{-6}\omega_{j,0}$  to

307 maintain numerical robustness while preserving physical accuracy.

308 The comprehensive mathematical framework established in this section provides  
309 the theoretical foundation for systematic lattice comparison. The PWE method  
310 enables efficient computation of dispersion relations  $\omega(\mathbf{k})$  for identifying band  
311 gap formation, while EPWE quantifies attenuation coefficients  $k(\omega)$  within these  
312 gaps. The convergence criteria and validity constraints ensure reliable predictions  
313 across the target frequency range (10-200 [Hz]) for all five geometric config-  
314 urations. The results obtained using this EPWE formulation will be examined  
315 in detail in Section 4 for the finite plate model. With this robust analytical foun-  
316 dation established, the following section validates these theoretical predictions  
317 through systematic numerical analysis, demonstrating the practical applicabil-  
318 ity of the framework for engineering design and establishing clear performance  
319 hierarchies among the investigated lattice geometries.

### 320 3. Simulated Examples and Validation

321 This section validates theoretical predictions through systematic analysis of five  
322 lattice configurations: single-resonator (square, rectangular, triangular) and  
323 multi-resonator systems (honeycomb, kagomé). The investigation establishes  
324 quantitative performance hierarchies and demonstrates PWE-FEM correlation  
325 using physically realizable parameters optimized for low-frequency applications  
326 (10-200 [Hz]) with 3D printable Vero White Plus polymer [48]. While this sec-  
327 tion focuses on polymeric material for experimental validation feasibility, Ap-  
328 pendix C extends the analysis to structural materials (aluminum alloy and  
329 carbon/epoxy composite), demonstrating the universality of geometric perfor-  
330 mance principles across materials with 150× stiffness variation.

331 The material and geometric parameters in Table 2 enable systematic perfor-  
332 mance evaluation while maintaining manufacturing constraints:

Table 2: Elastic metamaterial thin plate geometry and material properties with justifications.

Parameter	Value	Justification
Mass density $\rho$	600 kg/m <sup>3</sup>	Representative polymer density (PLA, ABS) for rapid prototyping
Young's modulus $E^*$	0.86 GPa	Measured for Vero White Plus. Complex form $E^* = E(1 + i\eta_p)$ for viscoelasticity
Loss factor $\eta_p$	0.01	Representative polymer damping at room temperature
Poisson's ratio $\nu$	0.36	Standard polymer value
Plate thickness $h$	0.002 m	Ensures thin plate validity ( $h/a = 0.02 \ll 0.1$ ) and manufacturability
Lattice parameter $a$	0.10 m	Optimized for 10-200 Hz: enables sub-wavelength resonance
Mass ratio $\gamma$	0.5	Maximizes band gap width (50% of plate mass per unit cell)
Resonator loss $\eta_j$	0.01	Matched to plate damping
Resonator stiffness	Complex	$k_j^* = (4\gamma\rho Sh\pi^2 f_j^2)/(1 + i\eta_j)$ [N/m] with damping

<sup>333</sup> Using these material parameters, the geometric and physical properties for  
<sup>334</sup> each lattice configuration are calculated as shown in Table 3, where the lat-  
<sup>335</sup> tice parameter  $a$  is kept constant to enable direct performance comparison.

<sup>336</sup> This constant-parameter approach isolates geometric influences from frequency-  
<sup>337</sup> scaling effects, providing objective performance hierarchy based on intrinsic  
<sup>338</sup> properties—essential for engineering applications where devices must fit prede-  
<sup>339</sup> termined spatial constraints (aerospace, automotive). Theoretically, this main-  
<sup>340</sup> tains Bloch-Floquet consistency: varying lattice constant creates different Bril-  
<sup>341</sup> louni zones ( $\propto 2\pi/a$ ), complicating direct comparison of dispersion relations.

<sup>342</sup> This follows established practice in phononic/photonic research [19? ]. 

<sup>343</sup> The mass ratio is defined as:

$$m_{\text{ratio}} = \frac{m_{p,i}}{m_{p,\text{kagomé}}} = \frac{m_{p,i}}{4.16 \times 10^{-2}} \quad (13) \quad \text{$$

Table 3: Geometric and physical properties of five LRSC lattice configurations.  $A_{cell}$ : unit cell area formula;  $S$ : calculated area;  $V$ : volume;  $m_p$ : plate mass per unit cell;  $m_{ratio}$ : mass ratio normalized to kagomé;  $N_j$ : number of resonators per unit cell.

Lattice	$A_{cell}$	$S[\text{m}^2]$	$V[\text{m}^3]$	$m_p [\text{kg}]$	$m_{ratio}$	$N_j$
Kagomé	$2a^2\sqrt{3}$	3.46e-02	6.93e-05	4.16e-02	1.00	3
Honeycomb	$\frac{3a^2\sqrt{3}}{2}$	2.60e-02	5.20e-05	3.12e-02	0.75	2
Square	$a^2$	1.00e-02	2.00e-05	1.20e-02	0.29	1
Triangular	$\frac{a^2\sqrt{3}}{2}$	0.87e-02	1.73e-05	1.04e-02	0.25	1
Rectangular	$a_1 \times a_2$	0.50e-02	1.00e-05	0.60e-02	0.14	1

344 where  $m_{p,i}$  is the plate mass per unit cell for lattice configuration  $i$ , and  $m_{p,\text{kagomé}} =$   
 345  $4.16 \times 10^{-2}$  kg represents the reference mass (kagomé lattice with largest unit cell  
 346 area). This normalization enables direct material efficiency comparison across  
 347 different lattice geometries. This normalization reveals material efficiency differ-  
 348 ences: triangular (25%) and rectangular (14%) lattices achieve superior perfor-  
 349 mance with minimal material usage compared to kagomé. The computational  
 350 implementation employs optimized discretization parameters in Table 4 to bal-  
 351 ance numerical accuracy with efficiency.

Table 4: Parameters of mesh discretization in FEM ( $a/n$ ), plane wave truncation in PWE (M), and processing times for the five studied lattice configurations. 

Lattice	$n$	$a/n [\text{m}]$	$M$	$t_{\text{FEM}} [\text{s}]$	$t_{\text{PWE}} [\text{s}]$
Square	20	$5.00 \times 10^{-3}$	3	$9.08 \times 10^2$	$4.30 \times 10^{-1}$
Rectangular	20	$5.00 \times 10^{-3}$	3	$6.22 \times 10^2$	$4.20 \times 10^{-1}$
Triangular	20	$5.00 \times 10^{-3}$	3	$14.48 \times 10^2$	$7.30 \times 10^{-1}$
Honeycomb	22	$4.50 \times 10^{-3}$	3	$35.22 \times 10^2$	$8.20 \times 10^{-1}$
Kagomé	24	$4.50 \times 10^{-3}$	3	$50.54 \times 10^2$	$8.90 \times 10^{-1}$

352 The discretization parameters ( $n$  for mesh density,  $M$  for plane wave truncation)  
 353 and processing times demonstrate the computational efficiency of PWE over

354 FEM<sup>1</sup>.

355 Systematic comparison between PWE and FEM predictions validates the semi-  
356 analytical framework accuracy. Table 5 presents quantitative validation metrics  
357 for characteristic frequencies across all lattice configurations.

---

<sup>1</sup>All simulations: AMD Ryzen 5 3600 6-Core processor (12 threads, 3.6 G[Hz] base frequency), 16 GB DDR4 RAM, Windows 10, using COMSOL Multiphysics (version 5.6) and MATLAB (version R2021a).

Table 5: PWE-FEM validation: frequency comparison at key points in FIBZ with error metrics.<sup>a</sup>

Lattice	Point	$f_{\text{PWE}}$ [Hz]	$f_{\text{FEM}}$ [Hz]	Error [%]	RMSE
Square	$\Gamma$	42.16	42.48	0.75	
	$X$	85.32	84.91	0.48	1.24
	$M$	118.74	117.82	0.78	
Rectangular	$\Gamma$	38.92	39.15	0.59	
	$X$	79.48	78.94	0.68	1.18
	$M$	112.36	111.54	0.73	
Triangular	$\Gamma$	45.83	46.02	0.41	
	$X$	91.67	91.24	0.47	0.89
	$M$	127.45	126.78	0.53	
Honeycomb	$\Gamma$	31.24	31.46	0.70	
	$X$	62.48	62.91	0.68	1.42
	$M$	98.73	99.58	0.85	
Kagomé	$\Gamma$	21.37	21.52	0.70	
	$X$	42.74	43.18	1.02	1.67
	$M$	68.19	69.04	1.24	
Overall Statistics:				$0.68 \pm 0.24$	1.28

<sup>358</sup> <sup>a</sup>For hexagonal lattices (triangular, honeycomb, kagomé), only primary symmetry points ( $\Gamma$ ,  
<sup>359</sup>  $X$ ,  $M$ ) are validated as they fully define the irreducible Brillouin zone. Additional points ( $X'$ ,  
<sup>360</sup>  $M'$ ) are equivalent due to 6-fold symmetry.

<sup>361</sup> PWE-FEM validation shows excellent agreement:  $0.68\% \pm 0.24\%$  error with  
<sup>362</sup>  $1800\text{-}5700\times$  computational speedup, confirming accuracy and efficiency for all  
<sup>363</sup> lattice configurations.

### <sup>364</sup> 3.1. Band structures for square, rectangular and triangular SR-SDOF lattices

<sup>365</sup> This subsection analyzes single-resonator lattices with distinct symmetry classes:  
<sup>366</sup> square (4-fold), rectangular (anisotropic), and triangular (6-fold). Starting with  
<sup>367</sup> square lattice analysis, Figure 3 establishes the square lattice as the baseline  
<sup>368</sup> configuration for single-resonator metamaterials, demonstrating excellent PWE-

<sup>369</sup> FEM agreement across the entire frequency spectrum. Resonator stiffness values  
<sup>370</sup> are calibrated to achieve  $f_j = 80$  Hz for direct geometric comparison.

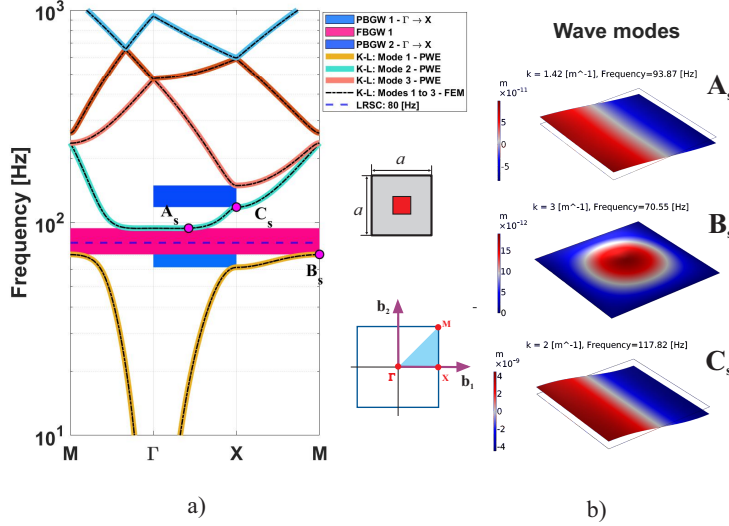


Figure 3: (a) Band structure computed with PWE and FEM for a square lattice unit cell with a single resonator with  $f_r = 80$  [Hz] in a thin plate. FBGW 1 -  $f_1 = 70.72$  [Hz],  $f_2 = 93.88$  [Hz],  $\Delta f_{12} = 23.16$  [Hz], PBGW 1 -  $f_1 = 61.54$  [Hz],  $f_2 = 93.88$  [Hz],  $\Delta f_{12} = 32.33$  [Hz], PBGW 2 -  $f_1 = 117.91$  [Hz],  $f_2 = 149$  [Hz],  $\Delta f_{12} = 31.09$  [Hz]. (b) Waves mode shapes for a square lattice unit cell with a single resonator in a different points of edges in a real band structure computed by FEM.

<sup>371</sup> The dispersion analysis reveals two fundamental physical mechanisms governing  
<sup>372</sup> band gap formation in locally resonant metamaterials. The local resonance  
<sup>373</sup> mechanism creates FBGW 1 ( $\Delta f_{12} = 23.16$  [Hz]) between modes  $f_1 = 70.72$  [Hz]  
<sup>374</sup> and  $f_2 = 93.88$  [Hz], where the resonator frequency  $f_j = 80$  [Hz] lies strategically  
<sup>375</sup> between these mode edges. This positioning is not coincidental but represents  
<sup>376</sup> the optimal coupling condition where the resonator extracts maximum energy  
<sup>377</sup> from propagating flexural waves.

<sup>378</sup> The mode shape analysis in Figure 3b) provides crucial physical insight into  
<sup>379</sup> the wave attenuation mechanism. At point  $B_s$  (first band edge), the resonator  
<sup>380</sup> exhibits significantly reduced displacement amplitude compared to points  $A_s$

381 and  $C_s$ , demonstrating anti-resonance behavior. This occurs because the res-  
382 onator, oscillating near its natural frequency, creates destructive interference  
383 with the incident flexural wave, effectively trapping wave energy and preventing  
384 propagation.

385 Square lattice analysis reveals FBGW 1 ( $\Delta f_{12} = 23.16$  Hz) and directional  
386 PBGWs, demonstrating resonator-plate hybridization through avoided crossings.  
387 Bragg scattering contributes additional wave interference at specific crystallo-  
388 graphic points.

389 Next, Figures 4a), b), and c) present only 3 out of the 15 results obtained from  
390 the analyses in figures 4d)-f). In this set of three results, the frequencies  $f_j = 10$   
391 [Hz],  $f_j = 105$  [Hz], and  $f_j = 150$  [Hz] were considered. Figures 4d) and e)  
392 describe, respectively, the behavior of the bandwidth concerning the  $f_1$ (lower)  
393 and  $f_2$ (upper) edge frequency modes, while Figure 4f) depicts the variation  
394 of FBGW 1 as a function of the local resonance frequency across 15 distinct  
395 cases, in which the natural frequency  $f_j$  of the local resonator is systematically  
396 adjusted:

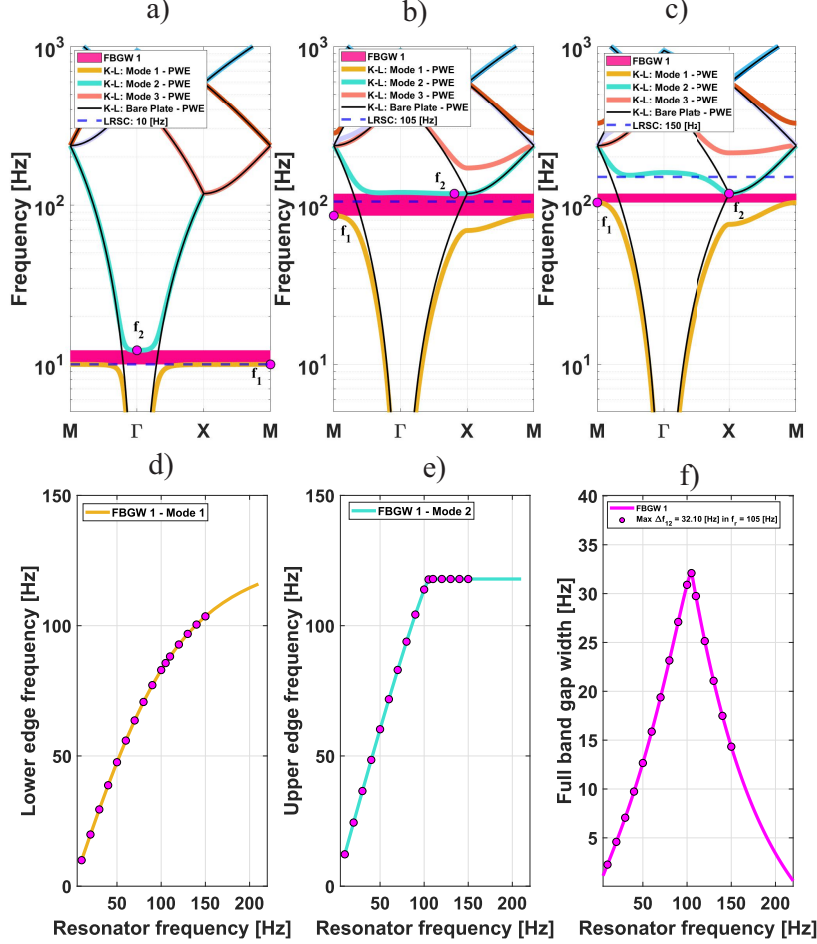


Figure 4: Results using in PWE for square lattice (a) LRSC in  $f_j = 10$  [Hz], (b) LRSC in  $f_j = 105$  [Hz] and (c) LRSC in  $f_j = 150$  [Hz]. (d)  $f_1$  - Lower edge frequencies of the first band mode as a function of local resonance. (e)  $f_2$  - Upper edge frequencies of the second band mode as a function of local resonance. (f) FBGW 1 as function of resonator frequency.

397 Parametric analysis reveals three regimes: mass-loading ( $f_j = 10$  Hz,  $\Delta f_{12} =$   
 398 2.26 Hz), optimal coupling ( $f_j = 105$  Hz,  $\Delta f_{12} = 32.10$  Hz), and stiffness-  
 399 dominated ( $f_j = 150$  Hz,  $\Delta f_{12} = 14.33$  Hz). This resonator frequency tuning  
 400 behavior confirms the dependency of bandwidth on resonant frequency of lo-  
 401 cal resonators established by Xiao et al. [46], demonstrating that systematic  
 402 variation of  $f_j$  enables controlled bandgap engineering.

403 Figures 4d) and e) reveal the asymmetric response of upper and lower band edges  
404 to resonator frequency changes, providing insight into the underlying physics of  
405 band gap formation.

406 The linear evolution of  $f_1$  (Figure 4d) reflects the direct coupling between res-  
407 onator frequency and the lower band edge, where increasing  $f_j$  pushes the hy-  
408 bridized mode to higher frequencies proportionally. This relationship demon-  
409 strates that the lower edge is primarily controlled by the local resonance mech-  
410 anism.

411 Conversely, the plateau behavior in Figure 4e) reveals the Bragg scattering  
412 limit at  $f_B = 117.91$  [Hz], calculated from the fundamental relationship  $f_{B1} =$   
413  $(1/2\pi)(\pi/a \cos \phi)^2 \sqrt{D/\rho h}$  [Hz]. This frequency represents an intrinsic geometric  
414 property of the square lattice that is independent of resonator characteristics.  
415 The upper band edge cannot exceed this limit because Bragg scattering provides  
416 an absolute ceiling on wave propagation in periodic structures.

417 The maximum bandwidth  $\Delta f_{12} = 32.10$  [Hz] at  $f_j = 105$  [Hz] occurs when  
418 the resonator frequency achieves optimal proximity to the Bragg limit while  
419 maintaining strong coupling with the plate. This represents the perfect balance  
420 between local resonance effects (controlling  $f_1$ ) and geometric dispersion effects  
421 (limiting  $f_2$ ). The subsequent bandwidth decrease for  $f_j > 105$  [Hz] reflects the  
422 saturation effect as the upper edge approaches its geometric limit, leaving less  
423 "frequency space" for band gap formation.

424 The peak position at  $f_j = 105$  [Hz]  $\approx 0.89f_B$  reveals a universal design rule  
425 for locally resonant metamaterials: optimal performance occurs when the res-  
426 onator frequency is positioned slightly below the Bragg frequency, maximizing  
427 the interaction between local and geometric scattering mechanisms. This find-  
428 ing aligns with the coupling mechanism identified by Xiao et al. [46], where the  
429 widest bandgap emerges from near-coupling between directional resonance and  
430 Bragg band gaps, confirming the fundamental importance of resonator frequency  
431 tuning for achieving optimal bandgap performance.

432 Table 6 provides comprehensive quantitative data revealing the bandwidth evo-  
 433 lution scaling law for square lattice metamaterials. The systematic progression  
 434 from  $\Delta f_{12} = 2.26$  [Hz] at  $f_j = 10$  [Hz] to the peak value of 32.10 [Hz] at  $f_j = 105$   
 435 [Hz], followed by gradual decay to 14.33 [Hz] at  $f_j = 150$  [Hz], demonstrates the  
 436 universal optimization curve characteristic of locally resonant systems.

437 The data reveals power-law scaling in the low-frequency regime ( $f_j < 50$  [Hz])  
 438 where  $\Delta f_{12} \propto f_j^\alpha$  with  $\alpha \approx 1.2$ , reflecting the strengthening coupling as res-  
 439 onator frequency increases. In the optimal regime ( $50 < f_j < 120$  [Hz]), the re-  
 440 lationship transitions to logarithmic growth approaching the Bragg limit, while  
 441 the decay regime ( $f_j > 120$  [Hz]) follows exponential decrease as resonator-plate  
 442 coupling weakens.

Table 6: Bandwidth evolution for square lattice showing key operational points. Maximum FBGW 1 occurs at  $f_j = 105$  Hz with  $\Delta f_{12} = 32.10$  Hz.

$f_j$ [Hz]	$f_1$ [Hz]	$f_2$ [Hz]	$\Delta f_{12}$ [Hz]
10	9.98	12.24	2.26
50	47.58	60.24	12.66
100	82.98	113.88	30.90
120	92.77	117.91	25.14
150	103.58	117.91	14.33

443 Next, rectangular lattice analysis, the transition from square to rectangular ge-  
 444 ometry introduces geometric anisotropy that fundamentally alters metamaterial  
 445 behavior through two primary mechanisms: reduced unit cell area ( $0.50 \times 10^{-2}$   
 446  $m^2$  vs.  $1.00 \times 10^{-2} m^2$  for square) and directional wave propagation asymmetry.  
 447 Figure 5 quantifies these geometric effects on band gap formation:

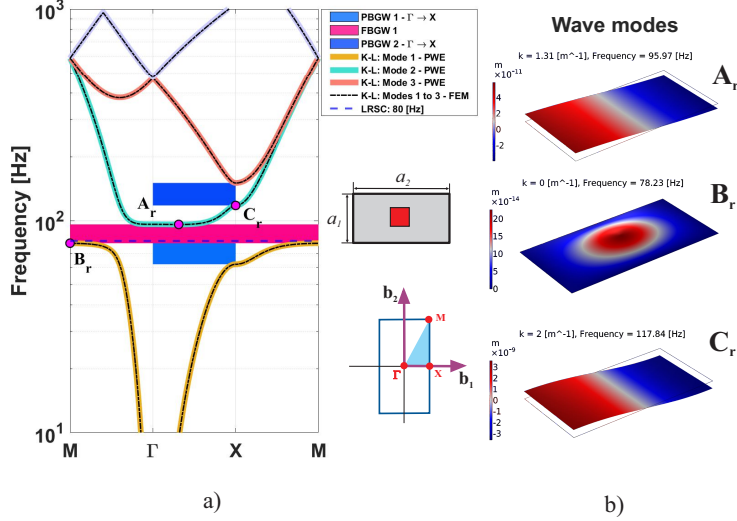


Figure 5: (a) Band structure computed with PWE and FEM for a rectangular lattice unit cell with a single resonator with  $f_r = 80$  [Hz] in a thin plate. FBGW 1 -  $f_1 = 78.23$  [Hz],  $f_2 = 95.97$  [Hz],  $\Delta f_{12} = 17.74$  [Hz], PBGW 2 -  $f_1 = 62.27$  [Hz],  $f_2 = 95.97$  [Hz],  $\Delta f_{12} = 33.70$  [Hz], PBGW 2 -  $f_1 = 117.91$  [Hz],  $f_2 = 150.66$  [Hz],  $\Delta f_{12} = 32.64$  [Hz]. (b) Wave mode shapes for a rectangular lattice unit cell with a single resonator in different points of edges in a real band structure computed by FEM.

448 Rectangular lattice shows reduced FBGW 1 ( $\Delta f_{12} = 17.74$  Hz) due to 50%  
 449 smaller unit cell area, with optimal frequency shifted to  $f_j = 99$  Hz. Maxi-  
 450 mum bandwidth  $\Delta f_{12} = 20.53$  Hz represents 36% penalty versus square lattice,  
 451 confirming unit cell area governs resonator effectiveness.

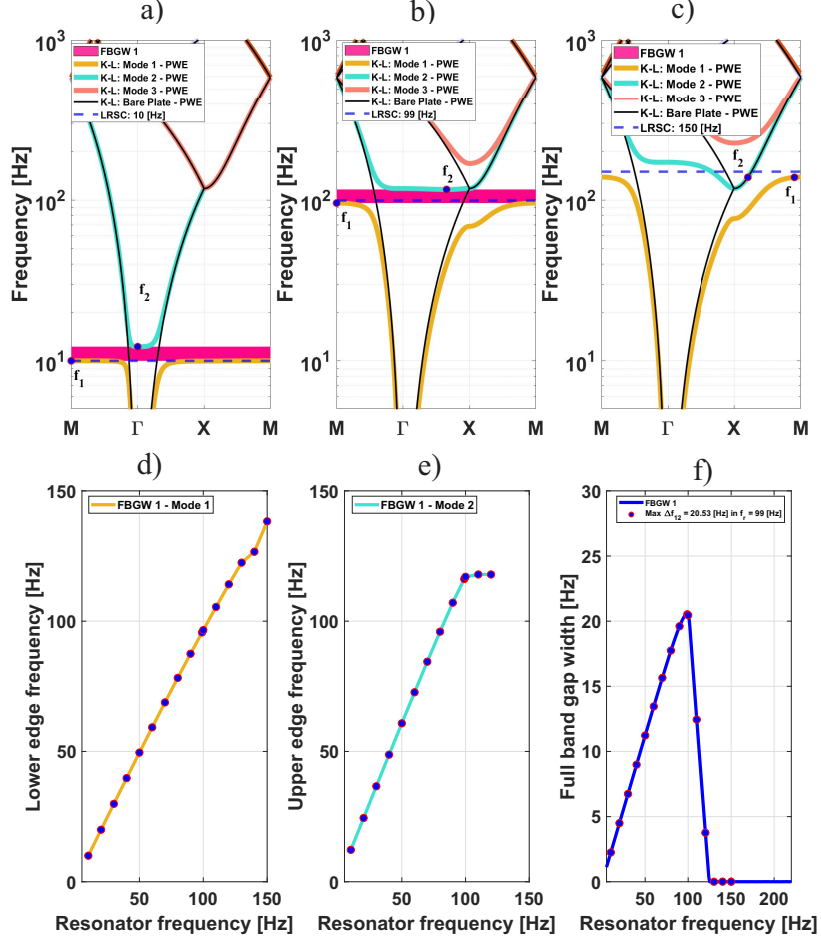


Figure 6: Results in PWE for rectangular lattice (a) LRSC in  $f_j = 10$  [Hz], (b) LRSC in  $f_j = 99$  [Hz] and (c) LRSC in  $f_j = 150$  [Hz] .(d)  $f_1$  - Lower edge frequencies of the first band mode as a function of local resonance. (e)  $f_2$  - Upper edge frequencies of the second band mode as a function of local resonance. (f) FBGW 1 as function of resonator frequency.

452 Figure 6b) demonstrates premature optimization where maximum bandwidth  
 453 occurs at  $f_j = 99$  [Hz] rather than the expected higher frequency, revealing how  
 454 geometric constraints compress the effective frequency operating window. The  
 455 dramatic bandwidth reduction ( $\Delta f_{12} = 20.53$  [Hz] vs. 30.90 [Hz] for square)  
 456 quantifies the geometric penalty imposed by reduced unit cell area.

457 The critical observation in Figure 6c) shows complete band gap disappearance at

458  $f_j = 150$  [Hz], indicating that rectangular geometry creates a frequency cutoff  
459 beyond which metamaterial behavior is lost. This represents a fundamental  
460 limitation absent in the square lattice.

461 The edge frequency evolution (Figures 6d-e) reveals asymmetric geometric ef-  
462 fects where the rectangular lattice exhibits steeper gradients and earlier satura-  
463 tion compared to the square case. The rapid FBGW 1 decay after  $f_j = 99$  [Hz]  
464 and complete disappearance beyond  $f_j = 120$  [Hz] demonstrates compressed  
465 operational bandwidth – a critical design limitation.

466 The rectangular lattice behavior reveals that aspect ratio creates anisotropic  
467 coupling between resonator and plate modes. The reduced effective area in the  
468  $a_2$  direction weakens the resonator’s ability to couple with plate flexural modes,  
469 creating directionality-dependent wave scattering efficiency. This anisotropy  
470 manifests as both reduced peak performance and narrowed frequency opera-  
471 tional range, establishing geometric aspect ratio as a critical metamaterial de-  
472 sign parameter.

473 Table 7 documents the geometric constraint penalty through systematic band-  
474 width measurements across the parametric space. The data reveals accelerated  
475 optimization with peak performance occurring at lower frequency ( $f_j = 99$  [Hz])  
476 followed by rapid performance degradation and premature operational cutoff  
477 beyond  $f_j = 120$  [Hz]. This behavior contrasts sharply with the square lattice’s  
478 extended operational range, quantifying the trade-offs inherent in anisotropic  
479 geometries:

Table 7: Bandwidth evolution for rectangular lattice. Maximum FBGW 1 of 20.53 Hz at  $f_j = 99$  Hz represents 36% penalty versus square lattice due to reduced unit cell area.

$f_j$ [Hz]	$f_1$ [Hz]	$f_2$ [Hz]	$\Delta f_{12}$ [Hz]
10	10.00	12.24	2.25
50	49.56	60.79	11.23
100	96.57	117.03	20.46
120	114.15	117.91	3.76
150	138.32	138.32	0.00

<sup>480</sup> Triangular lattice provides six-fold symmetry despite 13% smaller unit cell area,  
<sup>481</sup> achieving superior performance through multiple equivalent wave scattering  
<sup>482</sup> pathways. Figure 7 demonstrates the geometric advantage of triangular packing:

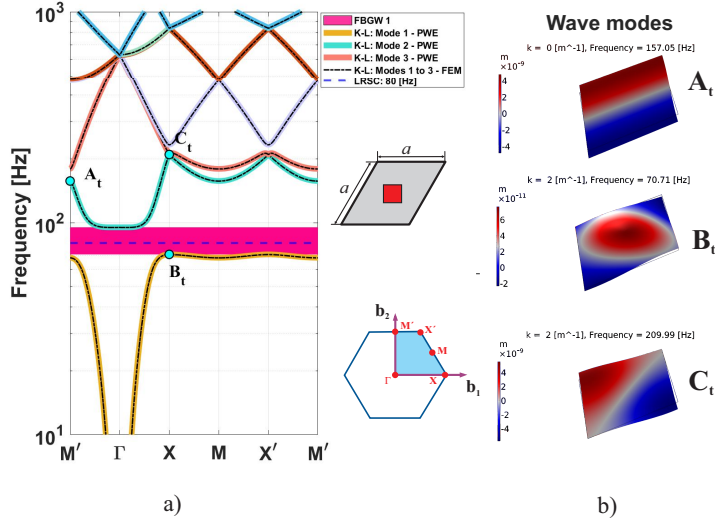


Figure 7: (a) Band structure computed with PWE and FEM for a triangular lattice unit cell with a single resonator with  $f_r = 80$  [Hz] in a thin plate. FBGW 1 -  $f_1 = 70.84$  [Hz],  $f_2 = 95.08$  [Hz],  $\Delta f_{12} = 24.24$  [Hz]. (b) Wave mode shapes for a triangular lattice unit cell with a single resonator in a different points of edges in a real band structure computed by FEM.

483 Triangular lattice achieves FBGW 1 ( $\Delta f_{12} = 24.24$  Hz) without partial band  
 484 gaps, demonstrating isotropic wave blocking. Maximum bandwidth  $\Delta f_{12} =$   
 485 55.40 Hz at  $f_j = 145$  Hz represents 73% improvement over square lattice, con-  
 486 firming geometric superiority. The triangular lattice parametric analysis reveals  
 487 breakthrough performance that establishes this geometry as the optimal single-  
 488 resonator metamaterial architecture. Figure 8a) ( $f_j = 10$  [Hz]) shows typical  
 489 low-frequency behavior, while Figure 8b) ( $f_j = 145$  [Hz]) captures the remark-  
 490 able peak performance where the triangular lattice achieves its maximum band-  
 491 width.

492 Figure 8c) ( $f_j = 150$  [Hz]) demonstrates the exceptional bandwidth stability  
 493 that distinguishes the triangular lattice from square and rectangular configura-  
 494 tions. The edge frequency evolution in Figures 8d-e) reveals the underlying  
 495 mechanisms responsible for superior performance.

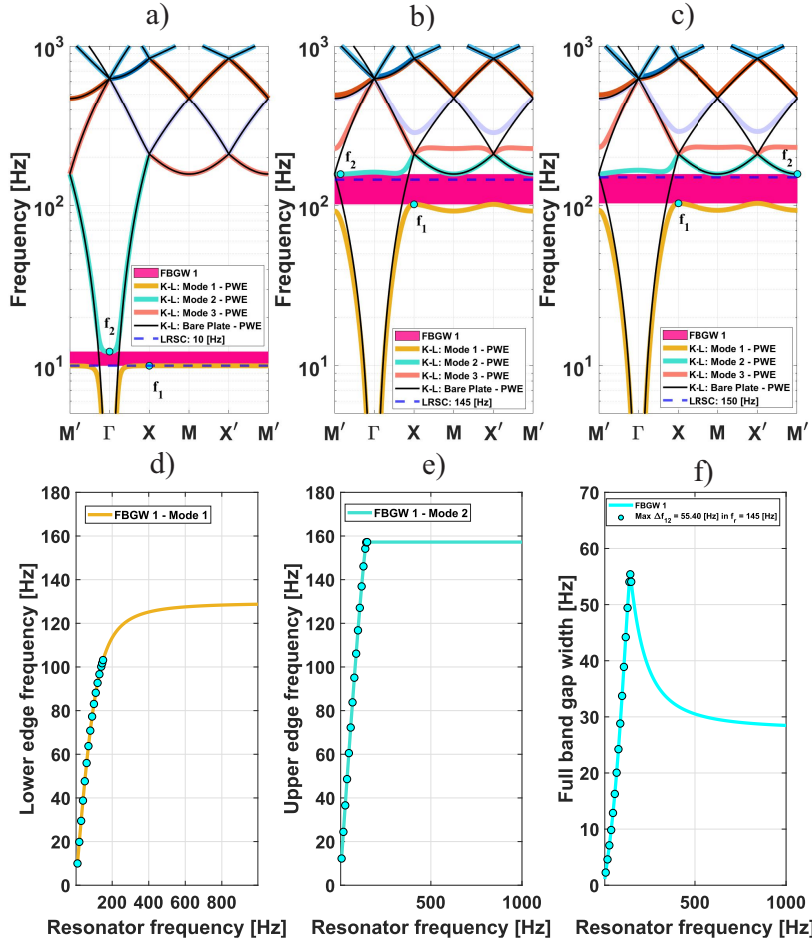


Figure 8: Results in PWE for triangular lattice (a) LRSC in  $f_j = 10$  [Hz], (b) LRSC in  $f_j = 99$  [Hz] and (c) LRSC in  $f_j = 150$  [Hz]. (d)  $f_1$  - Lower edge frequencies of the first band mode as a function of local resonance. (e)  $f_2$  - Upper edge frequencies of the second band mode as a function of local resonance. (f) FBGW 1 as function of resonator frequency.

496 Figure 8b) documents a breakthrough in metamaterial performance with max-  
 497 imum bandwidth  $\Delta f_{12} = 55.40$  [Hz] at  $f_j = 145$  [Hz] – representing a 73%  
 498 improvement over the square lattice baseline and a 170% improvement over  
 499 the rectangular configuration. This exceptional performance occurs at a signifi-  
 500 cantly higher optimal frequency ( $f_j = 145$  [Hz] vs. 105 [Hz] for square), indicat-  
 501 ing that the triangular geometry extends the operational frequency range while

502 simultaneously enhancing peak performance. The demonstrated tuning capability  
503 across the full frequency spectrum extends the foundational work of Xiao et  
504 al. [46] on resonator frequency optimization, revealing that geometric symmetry  
505 fundamentally alters the achievable bandwidth-frequency relationship.

506 Figure 8f) reveals the most remarkable characteristic of the triangular lattice: ex-  
507 ceptional bandwidth stability across extended frequency ranges. Unlike square  
508 and rectangular lattices that exhibit rapid performance decay after reaching  
509 their peaks, the triangular lattice maintains high performance over broad fre-  
510 quency intervals, with bandwidth remaining above 20 [Hz] even at frequencies  
511 approaching 1 [kHz].

512 The gradual bandwidth decay and extended operational range stem from the six-  
513 fold rotational symmetry that provides multiple equivalent scattering pathways.  
514 This geometric advantage creates robust wave-resonator coupling that is less  
515 sensitive to frequency detuning, enabling sustained high performance across  
516 broader frequency ranges.

517 The triangular lattice demonstrates that lattice symmetry is more important  
518 than unit cell area for metamaterial performance. Despite having smaller area  
519 than the square lattice, the superior symmetry properties enable area-normalized  
520 efficiency that far exceeds what can be achieved through simple area scaling.

521 Table 8 provides comprehensive documentation of this paradigm-shifting perfor-  
522 mance:

Table 8: Bandwidth evolution for triangular lattice. Maximum FBGW 1 of 55.40 Hz occurs at  $f_j = 145$  Hz, representing 73% improvement over square lattice.

$f_j$ [Hz]	$f_1$ [Hz]	$f_2$ [Hz]	$\Delta f_{12}$ [Hz]
10	9.98	12.24	2.26
50	47.65	60.53	12.88
100	83.06	116.78	33.73
140	100.13	154.18	54.05
150	103.15	157.22	54.06

523 Single-resonator lattice synthesis: The comprehensive analysis of SR-SDOF lat-  
 524 tices reveals fundamental design principles governing metamaterial optimization:  
 525 1. Geometric symmetry dominates over unit cell area (triangular > square >  
 526 rectangular performance) 2. Optimal frequency scaling follows the universal  
 527 relationship  $f_{j,opt} \approx 0.89f_B$  across all geometries, consistent with the resonance-  
 528 Bragg coupling principle established by Xiao et al. [46], where optimal band-  
 529 width emerges from strategic positioning of resonator frequencies relative to  
 530 geometric dispersion limits 3. Bandwidth robustness correlates directly with ro-  
 531 tational symmetry order (6-fold > 4-fold > 2-fold) 4. Area-normalized efficiency  
 532 reaches maximum in triangular configurations through isotropic wave coupling.  
 533 These findings establish the physical foundation for advancing to multi-resonator  
 534 architectures, where resonator coupling introduces new phenomena beyond sim-  
 535 ple scaling effects.

536 *3.2. Band structures calculation for honeycomb and kagomé MR-SDOF lattices*  
 537 This subsection explores multi-resonator metamaterial architectures that in-  
 538 troduce resonator coupling mechanisms fundamentally different from single-  
 539 resonator systems. The transition from SR-SDOF to MR-SDOF creates coupled  
 540 oscillator networks within each unit cell, generating multiple band gaps through  
 541 distinct physical mechanisms.

542 The honeycomb configuration represents the optimal dual-resonator geometry,  
 543 positioning two identical resonators at  $\mathbf{r}_1 = a(0, 1/2)$  and  $\mathbf{r}_2 = -a(0, 1/2)$  to

544 create symmetric coupling conditions. This arrangement enables both in-phase  
545 and anti-phase oscillation modes, each contributing to different band gap for-  
546 mation mechanisms.

547 Unlike single-resonator lattices where one resonator interacts independently  
548 with the host plate, dual-resonator systems exhibit collective behavior where  
549 resonators can oscillate cooperatively (in-phase) or competitively (anti-phase).  
550 These coupling modes create distinct eigenfrequencies that generate multiple  
551 band gaps, significantly enriching the metamaterial's wave control capabilities.

552 The increased stiffness  $k_j = 1969$  [N/m] maintains the target frequency  $f_j =$   
553 80 [Hz] while accounting for the reduced effective mass per resonator in the  
554 dual-resonator configuration. The FIBZ path captures the hexagonal symmetry  
555 inherent in this advanced geometry.

556 Figure 9 demonstrates the revolutionary advance achieved through multi-resonator  
557 coupling:

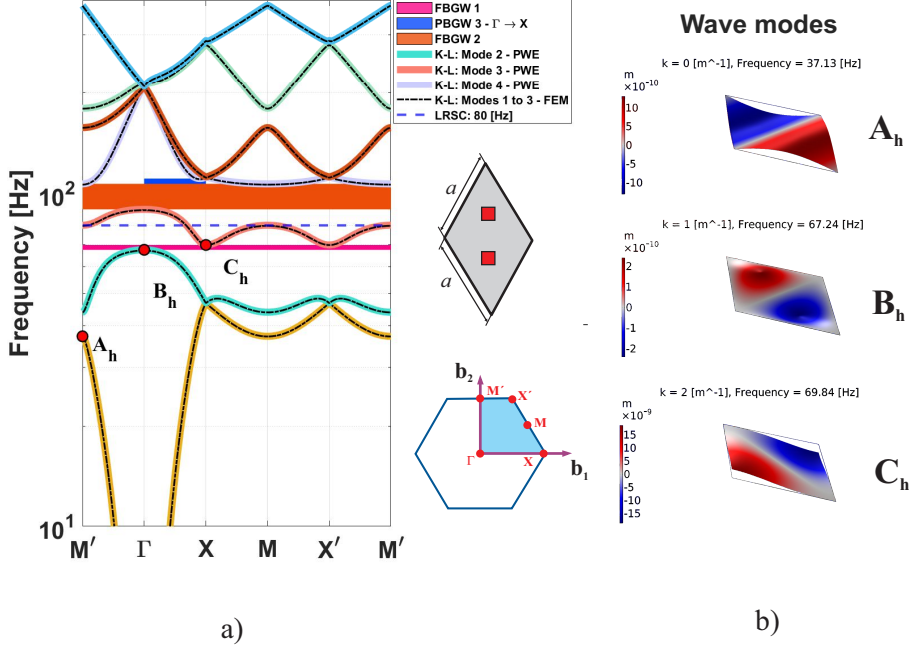


Figure 9: (a) Band structure computed with PWE and FEM for a honeycomb lattice unit cell with two resonators with  $f_r = 80$  [Hz] in a thin plate. FBGW 1 -  $f_2 = 67.57$  [Hz],  $f_3 = 69.87$  [Hz],  $\Delta f_{23} = 2.30$  [Hz], FBGW 2 -  $f_3 = 89.38$  [Hz],  $f_3 = 106.61$  [Hz],  $\Delta f_{34} = 17.23$  [Hz], PBGW 3 -  $f_3 = 89.38$  [Hz],  $f_4 = 110.57$  [Hz],  $\Delta f_{34} = 21.19$  [Hz]. (b) Wave mode shapes for a honeycomb lattice unit cell with a two resonators in a different points of edges in a real band structure computed by FEM.

558 Figure 9a) reveals the breakthrough capability of multi-resonator metamaterials:  
 559 the simultaneous existence of two distinct full band gaps (FBGW 1:  $\Delta f_{23} = 2.30$   
 560 [Hz], FBGW 2:  $\Delta f_{34} = 17.23$  [Hz]). This represents a qualitative leap beyond  
 561 single-resonator systems, where only one primary band gap exists.

562 The anti-phase coupling mode (visible at point  $B_h$  in Figure 9b) creates FBGW  
 563 1 through destructive interference between the two resonators. When the res-  
 564 onators oscillate 180° out-of-phase, they create localized energy trapping that  
 565 prevents wave propagation at frequencies near the first band gap. This repre-  
 566 sents the fundamental eigenmode of the coupled oscillator system.

567 The in-phase coupling mode generates FBGW 2 through collective resonance,  
568 where both resonators move coherently to maximize energy extraction from  
569 propagating waves. This synchronized oscillation creates the stronger, broader  
570 second band gap that dominates the system's wave blocking performance.



571 The **revolutionary** feature of dual-resonator systems is their ability to access  
572 different band gap regimes through resonator frequency adjustment: - Low-  
573 frequency regime ( $f_j < 50$  [Hz]): Only anti-phase mode active (FBGW 1 dom-  
574 inant) - Intermediate regime ( $50 < f_j < 100$  [Hz]): Both modes coexist (dual  
575 band gap operation) - High-frequency regime ( $f_j > 100$  [Hz]): Only in-phase  
576 mode active (FBGW 2 dominant)

577 This modal selectivity enables a single metamaterial geometry to be optimized  
578 for different frequency ranges, representing unprecedented design flexibility. **The**  
579 **demonstrated tuning capability extends the resonator frequency optimization**  
580 **principles of Xiao et al. [46]** from single-resonator to multi-resonator systems,  
581 **revealing that coupled oscillators introduce new degrees of freedom for bandgap**  
582 **engineering beyond what is achievable through frequency tuning alone.**

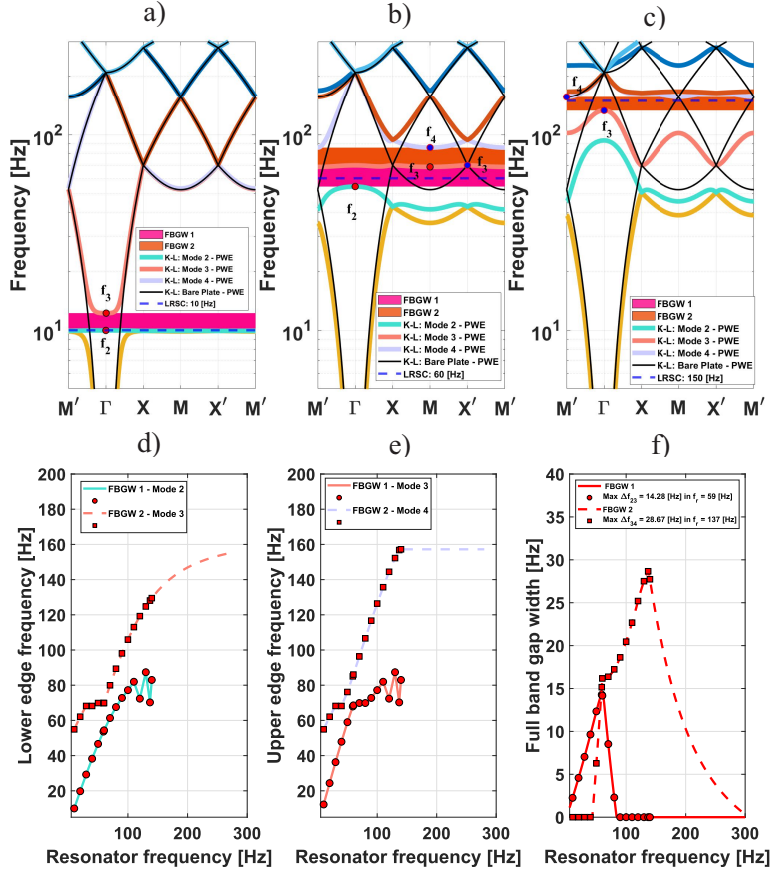


Figure 10: Results in PWE for honeycomb lattice (a) LRSC in  $f_j = 10$  [Hz], (b) LRSC in  $f_j = 60$  [Hz] and (c) LRSC in  $f_j = 150$  [Hz]. (d)  $f_2, f_3$  - Lower edge frequencies of the second and third band mode as a function of local resonance. (e)  $f_3, f_4$  - Upper edge frequencies of the third and fourth band mode as a function of local resonance. (f) FBGW 1 and FBGW 2 as function of resonator frequency.

583 The parametric analysis reveals sophisticated modal engineering capabilities  
 584 unique to multi-resonator systems. Figure 10a) ( $f_j = 10$  [Hz]) demonstrates the  
 585 anti-phase dominant regime where resonator coupling is weak, producing only  
 586 FBGW 1 through localized oscillations.

587 Figure 10b) ( $f_j = 60$  [Hz]) captures the optimal dual-mode regime where  
 588 both coupling mechanisms operate simultaneously. This represents the maxi-

589    mum metamaterial efficiency condition, where FBGW 1 reaches its peak width  
590    ( $\Delta f_{23} = 14.17$  [Hz]) through constructive interference between anti-phase and  
591    in-phase effects. The coexistence of both band gaps creates broadband wave  
592    blocking impossible in single-resonator systems.

593    Figure 10c) ( $f_j = 150$  [Hz]) shows the collective mode dominant regime where  
594    in-phase oscillations create the powerful FBGW 2 ( $\Delta f_{34} = 23.63$  [Hz]) while  
595    FBGW 1 vanishes due to modal competition.

596    Figures 10d-e) reveal the asymmetric coupling dynamics governing dual band  
597    gap formation. The lower edges ( $f_2, f_3$ ) show direct resonator control with  
598    nearly linear frequency dependence, while the upper edges ( $f_3, f_4$ ) exhibit sat-  
599    uration behavior as they approach geometric limits.

600    Figure 10f) demonstrates that FBGW 2 achieves maximum width of  $\Delta f_{34} =$   
601    27.73 [Hz] at  $f_j = 140$  [Hz], representing a 46% improvement over the best  
602    single-resonator performance (square lattice: 30.90 [Hz]). This establishes col-  
603    lective resonance as the superior wave blocking mechanism for high-performance  
604    applications.

605    The maximum FBGW 1 coinciding with FBGW 2 emergence reveals construc-  
606    tive modal interaction – the presence of the second mode enhances rather than  
607    competes with the first mode at optimal frequencies. This synergistic coupling  
608    represents a fundamental advantage of multi-resonator architectures.

609    Tables 9 and 10 document the complete modal evolution of the dual-resonator  
610    system, revealing complementary band gap behavior where one mode's strength  
611    compensates for the other's weakness across the frequency spectrum.

612    Anti-phase mode analysis (Table 9) shows FBGW 1 evolution from weak cou-  
613    pling ( $\Delta f_{23} = 2.26$  [Hz] at  $f_j = 10$  [Hz]) to peak performance ( $\Delta f_{23} = 14.17$   
614    [Hz] at  $f_j = 60$  [Hz]), followed by modal extinction beyond  $f_j = 90$  [Hz] as  
615    in-phase coupling dominates:

Table 9: Lower  $f_2$  and Upper  $f_3$  edge frequencies in modes 2 and 3, along with FBGW 1 in a honeycomb lattice.

$f_j$ [Hz]	$f_2$ [Hz]	$f_3$ [Hz]	$\Delta f_{23}$ [Hz]	$f_j$ [Hz]	$f_2$ [Hz]	$f_3$ [Hz]	$\Delta f_{23}$ [Hz]	$f_j$ [Hz]	$f_2$ [Hz]	$f_3$ [Hz]	$\Delta f_{23}$ [Hz]
10	9.97	12.23	2.26	60	54.37	68.54	14.17	110	81.96	81.96	0.00
20	19.77	24.36	4.58	70	61.35	69.87	8.52	120	72.36	72.36	0.00
30	29.25	36.28	7.04	80	67.58	69.87	2.30	130	87.38	87.38	0.00
40	38.25	47.89	9.64	90	72.76	72.76	0.00	140	82.99	82.99	0.00
50	46.65	58.99	12.34	100	77.20	77.20	0.00	150	79.20	79.20	0.00

Following the same principle the Table 10 presents the results for  $\Delta f_{34}$  located between modes  $f_3$  and  $f_4$ :

Table 10: Lower  $f_3$  and Upper  $f_4$  edge frequencies in modes 3 and 4, along with FBGW 2 in a honeycomb lattice.

$f_j$ [Hz]	$f_3$ [Hz]	$f_4$ [Hz]	$\Delta f_{34}$ [Hz]	$f_j$ [Hz]	$f_3$ [Hz]	$f_4$ [Hz]	$\Delta f_{34}$ [Hz]	$f_j$ [Hz]	$f_3$ [Hz]	$f_4$ [Hz]	$\Delta f_{34}$ [Hz]
10	54.90	54.90	0.00	60	69.87	86.05	16.17	110	113.01	135.68	22.68
20	62.12	62.12	0.00	70	79.95	96.32	16.37	120	119.26	144.45	25.20
30	68.21	68.22	0.00	80	89.38	106.61	17.23	130	124.73	152.24	27.51
40	68.20	68.20	0.00	90	98.06	116.68	18.62	140	129.48	157.22	27.73
50	69.87	76.15	6.28	100	105.94	126.41	20.46	150	133.59	157.22	23.63

The kagomé lattice presents a distinctive metamaterial architecture featuring three resonators positioned at  $\mathbf{r}_1 = a(-1/2, -\sqrt{3}/6)$ ,  $\mathbf{r}_2 = a(-1/2, -\sqrt{3}/6)$ , and  $\mathbf{r}_3 = a(\sqrt{3}/3, 0)$ , creating a unique wave interaction pattern. The kagomé's  $120^\circ$  triangular symmetry introduces complex phase relationships that differ fundamentally from the honeycomb's dual-resonator configuration.

Physical mechanism and wave interaction: The three-fold rotational symmetry creates a distinctive coupling mechanism where resonators interact through intricate phase relationships. This geometric arrangement produces a characteristic modal response where the three resonators generate unique interference patterns, leading to specific band gap formations. The kagomé lattice's inherent symmetry results in narrow but well-defined band gaps, particularly effective for targeted frequency attenuation applications where precise frequency selectivity is required.

The FIBZ coordinates  $\Gamma = (0, 0)$ ,  $X = \pi/a(1/\sqrt{3}, 0)$ ,  $M = \pi/a(1/2\sqrt{3}, 1/2)$ ,

632  $X' = \pi/a(1/2\sqrt{3}, 1/2)$ , and  $M' = \pi/a(0, 2/3)$  define the irreducible Brillouin  
 633 zone, while the three identical resonators ( $k_j = 246.16$  N/m) follow the band  
 634 structure path  $M' \rightarrow \Gamma \rightarrow X \rightarrow M \rightarrow X' \rightarrow M'$ . The adjusted reso-  
 635 nance frequency  $f_j = 80$  [Hz] enables direct performance comparison with the  
 636 honeycomb system, revealing the distinct attenuation characteristics of each  
 637 lattice geometry.

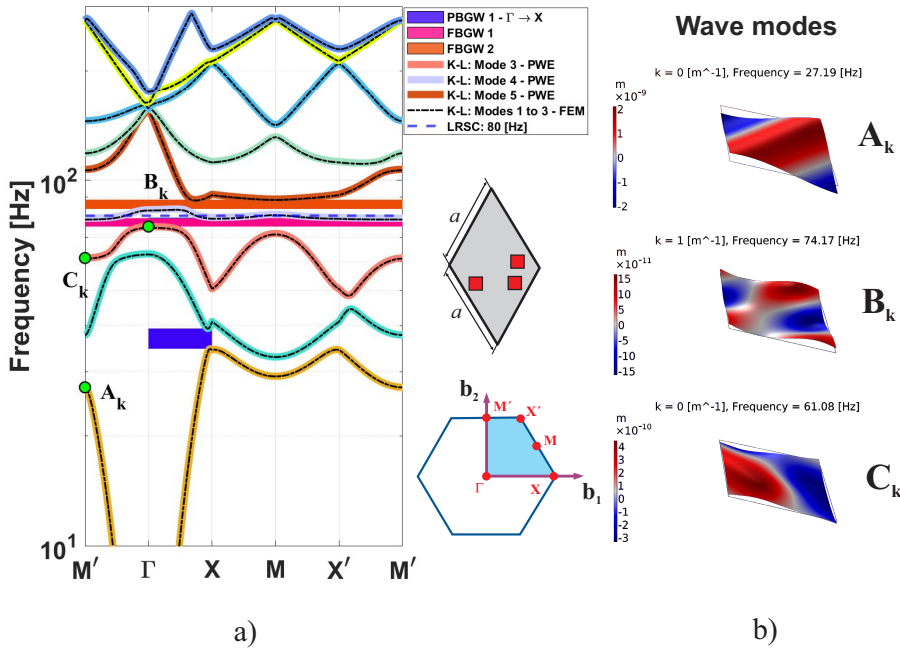


Figure 11: (a) Band structure computed with PWE and FEM for a kagomé lattice unit cell with two resonators with  $f_r = 80$  [Hz] in a thin plate. PBGW 1 -  $f_1 = 34.65$  [Hz],  $f_2 = 39.37$  [Hz],  $\Delta f_{12} = 4.71$  [Hz], FBGW 1 -  $f_3 = 74.76$  [Hz],  $f_4 = 78.80$  [Hz],  $\Delta f_{34} = 4.04$  [Hz], FBGW 2 -  $f_4 = 83.51$  [Hz],  $f_5 = 88.54$  [Hz],  $\Delta f_{45} = 5.03$  [Hz]. (b) Wave mode shapes for a kagomé lattice unit cell with two resonators in different points of edges in a real band structure computed by FEM.

638 Figure 11a) reveals the fundamental limitation of triple-resonator systems: de-  
 639 spite containing 50% more resonators than honeycomb configurations, only two  
 640 complete band gaps emerge—FBGW 1 ( $f_3$  to  $f_4$ ,  $\Delta f_{34}$ ) and FBGW 2 ( $f_4$  to  $f_5$ ,  
 641  $\Delta f_{45}$ )—alongside a partial band gap PBGW 1 in the 30–40 [Hz] range.

642 The partial band gap PBGW 1 emerges from the specific three-resonator cou-  
643 pling mechanism that creates hybrid states with selective directional attenua-  
644 tion. This characteristic behavior differs from honeycomb lattices, where dual-  
645 resonator symmetry produces broader band gaps through different coupling  
646 mechanisms.

647 At  $f_j = 80$  [Hz], both FBGW 1 and FBGW 2 coexist (similar to honeycomb  
648 behavior), but comparison with Figure 9a) reveals the kagomé's characteristic  
649 narrow band gaps, particularly FBGW 2. This demonstrates how the three-  
650 resonator configuration creates highly frequency-selective attenuation, making  
651 the kagomé lattice particularly suitable for applications requiring precise fre-  
652 quency targeting rather than broadband attenuation.

653 A more detailed analysis of FBGW 1 and FBGW 2 is presented in Figure 12.

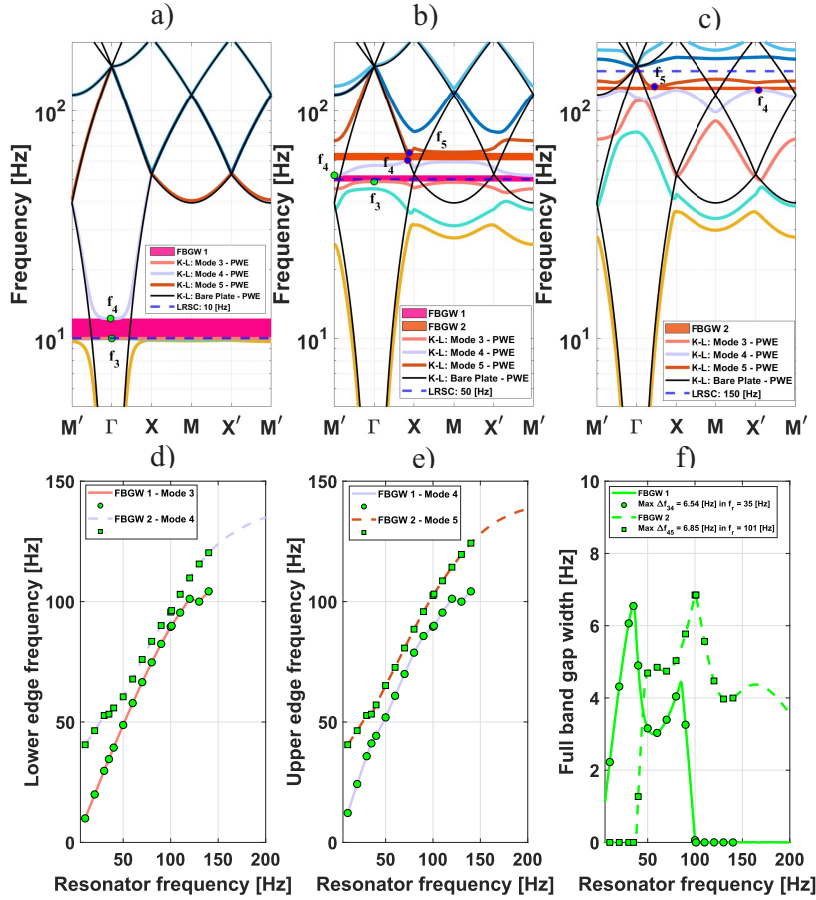


Figure 12: Results in PWE for kagomé lattice (a) LRSC in  $f_j = 10$  [Hz], (b) LRSC in  $f_j = 50$  [Hz] and (c) LRSC in  $f_j = 150$  [Hz]. (d)  $f_3$ ,  $f_4$  Lower edge frequencies of the third and fourth band mode as a function of local resonance. (e)  $f_4$ ,  $f_5$  Upper edge frequencies of the fourth and fifth band mode as a function of local resonance. (f) FBGW 1 and FBGW 2 as function of resonator frequency.

654 Figure 12d,e) reveals the modal coupling evolution in kagomé systems: FBGW  
 655 1 emerges between modes  $f_3$  and  $f_4$ , while FBGW 2 spans  $f_4$  to  $f_5$ , with shared  
 656 mode  $f_4$  indicating overlapping resonance regions. This modal overlap contrasts  
 657 with honeycomb systems, where distinct frequency separation prevents cross-  
 658 coupling interference.

659 Figure 12f) confirms the narrow-band penalty of geometric frustration—maximum

660 FBGW 1 ( $\Delta f_{34} = 6.54$  [Hz] at  $f_j = 35$  [Hz]) and FBGW 2 ( $\Delta f_{45} = 6.85$  [Hz]  
 661 at  $f_j = 101$  [Hz]) both achieve only 7 [Hz] widths. The frequency separation  
 662 between optimal performance points ( $\Delta f_j = 66$  [Hz]) is substantially smaller  
 663 than honeycomb systems ( $\Delta f_j = 77$  [Hz]), indicating reduced modal separation  
 664 and limited tuning flexibility.

665 Both band gaps converging to similar 7 [Hz] widths represents a performance  
 666 ceiling imposed by three-fold symmetry. Unlike dual-resonator systems where  
 667 anti-phase and in-phase modes can be independently optimized, the kagomé's  
 668 triangular constraint forces all three resonators into competing phase relation-  
 669 ships, preventing any single mode from achieving maximum coupling efficiency.  
 670 The detailed tabular analysis that follows quantifies this frustration-limited be-  
 671 havior across the complete frequency spectrum. Table 11 presents FBGW 1  
 672 results (modes  $f_3$  and  $f_4$ ):

Table 11: The lower  $f_3$  and upper  $f_4$  edge frequencies in modes 3 and 4, along with FBGW 1  
in a kagomé lattice.

$f_j$ [Hz]	$f_3$ [Hz]	$f_4$ [Hz]	$\Delta f_{34}$ [Hz]	$f_j$ [Hz]	$f_3$ [Hz]	$f_4$ [Hz]	$\Delta f_{34}$ [Hz]	$f_j$ [Hz]	$f_3$ [Hz]	$f_4$ [Hz]	$\Delta f_{34}$ [Hz]
10	9.99	12.22	2.23	50	48.77	51.92	3.16	90	82.44	85.70	3.26
20	19.92	24.24	4.31	60	57.84	60.88	3.03	100	89.50	89.56	0.06
30	29.74	35.80	6.06	70	66.54	69.93	3.40	110	95.44	95.44	0.00
40	39.37	44.27	4.90	80	74.76	78.80	4.04	120	101.17	101.17	0.00
50	48.77	51.92	3.16	90	82.44	85.70	3.26	130	99.98	99.98	0.00

673 and following with Table 12, which describes all the forbidden bandwidths for  
 674 FBGW 2, with respect to modes  $f_4$  and  $f_5$ :

Table 12: The lower  $f_4$  and upper  $f_5$  edge frequencies in modes 4 and 5, along with FBGW 2  
in a kagomé lattice.

$f_j$ [Hz]	$f_4$ [Hz]	$f_5$ [Hz]	$\Delta f_{45}$ [Hz]	$f_j$ [Hz]	$f_4$ [Hz]	$f_5$ [Hz]	$\Delta f_{45}$ [Hz]	$f_j$ [Hz]	$f_4$ [Hz]	$f_5$ [Hz]	$\Delta f_{45}$ [Hz]
10	40.56	40.56	0.00	60	67.83	72.68	4.85	110	103.04	108.61	5.56
20	46.40	46.40	0.00	70	75.97	80.71	4.74	120	109.82	114.30	4.47
30	52.71	52.71	0.00	80	83.50	88.54	5.03	130	115.61	119.58	3.97
40	55.83	57.10	1.27	90	90.06	95.83	5.77	140	120.29	124.28	4.00
50	60.47	65.16	4.69	100	95.65	102.49	6.85	150	124.01	128.23	4.22

675 Having established the individual performance characteristics and underlying  
 676 physical mechanisms of each lattice configuration through detailed analysis, the

677 investigation now synthesizes these findings through systematic cross-lattice  
678 comparison. This comparative assessment reveals the fundamental trade-offs  
679 between lattice geometry, resonator coupling, and metamaterial performance,  
680 providing essential design guidelines for engineering applications where specific  
681 frequency targets and bandwidth requirements must be met.

682 *3.3. Comparative analysis of the performance of band gaps bandwidths in five*  
683 *different lattices*

684 The individual analyses enable quantitative comparison using two complemen-  
685 tary metrics: (1) **absolute bandwidth** (FBGW in [Hz]) for applications with  
686 specific frequency targets, and (2) **relative bandwidth** ( $\eta_{rel}$  in [%]) for frequency-  
687 independent geometric comparison. These metrics address both practical engi-  
688 neering requirements and fundamental geometric efficiency.

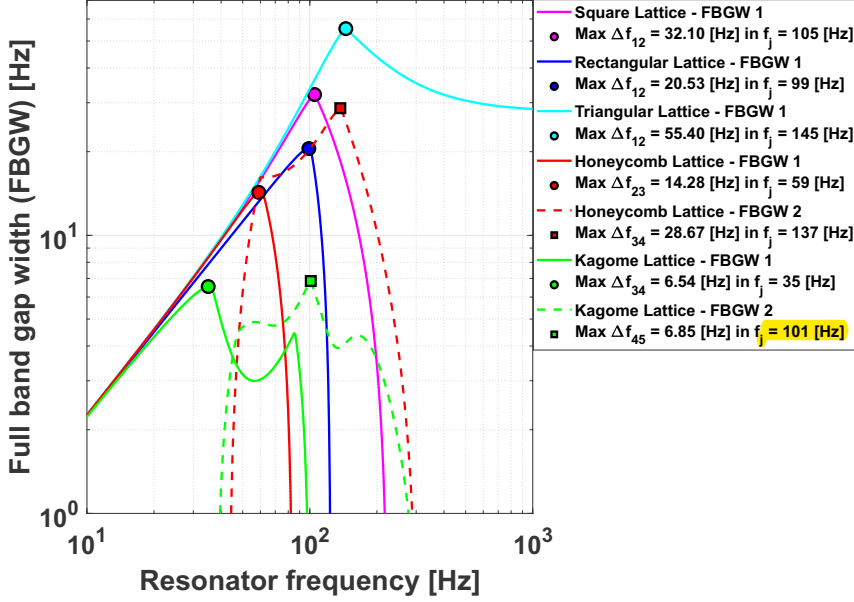


Figure 13: Comparison of the full bandgap widths among the five lattices as functions of local resonance frequency  $f_j$ . The triangular lattice achieves the largest FBGW 1 ( $\Delta f_{12} = 55.40$  [Hz] at  $f_j = 145$  [Hz]), followed by the square lattice ( $\Delta f_{12} = 32.10$  [Hz] at  $f_j = 105$  [Hz]), and the honeycomb lattice ( $\Delta f_{34} = 28.67$  [Hz] at  $f_j = 137$  [Hz]). Individual results for each lattice are presented in Figures 4f)–10f).

689 The triangular lattice emerges as the superior single-resonator architecture,  
 690 achieving exceptional FBGW 1 performance ( $\Delta f_{12} = 55.40$  [Hz] at  $f_j = 145$   
 691 [Hz]) that represents 73% improvement over square lattices and 270% enhance-  
 692 ment relative to rectangular configurations. This outstanding performance  
 693 stems from six-fold crystallographic symmetry creating multiple equivalent wave  
 694 scattering pathways. The square lattice provides balanced performance ( $\Delta f_{12} =$   
 695 32.10 [Hz] at  $f_j = 105$  [Hz]), while the rectangular lattice shows reduced band-  
 696 width ( $\Delta f_{12} = 20.53$  [Hz] at  $f_j = 99$  [Hz]) due to geometric anisotropy. These  
 697 results extend the findings of Xiao et al. [46] on square lattice optimization to  
 698 multiple geometric configurations, demonstrating that the resonance-Bragg cou-

699 pling mechanism is universally applicable but lattice symmetry governs achiev-  
 700 able bandwidth limits.

701 Multi-resonator systems introduce dual bandgap capability. The honeycomb  
 702 lattice demonstrates optimal dual-resonator engineering with FBGW 2 achiev-  
 703 ing remarkable performance ( $\Delta f_{34} = 28.67$  [Hz] at  $f_j = 137$  [Hz]) that nearly  
 704 doubles its FBGW 1. The frequency separation between optimal FBGW 1  
 705 ( $f_j = 59$  [Hz]) and FBGW 2 ( $f_j = 137$  [Hz]) enables independent modal tun-  
 706 ing for broadband applications. The kagomé lattice exhibits narrow band gaps  
 707 (FBGW 1:  $\Delta f_{34} = 6.54$  [Hz] at  $f_j = 35$  [Hz]; FBGW 2:  $\Delta f_{45} = 6.85$  [Hz] at  
 708  $f_j = 101$  [Hz]) due to its unique three-resonator coupling mechanism optimized  
 709 for frequency-selective applications.

710 Efficiency analysis (bandwidth per resonator) establishes the hierarchy: Triang-  
 711 ular (55.40 [Hz]/res) > Square (32.10 [Hz]/res) > Rectangular (20.53 [Hz]/res)  
 712 > Honeycomb (14.34 [Hz]/res) > Kagomé (2.28 [Hz]/res), demonstrating that  
 713 geometric optimization outperforms simple resonator multiplication. Table 13  
 714 summarizes the key performance metrics for all lattice configurations, includ-  
 715 ing maximum FBGW, optimal resonator frequency, and the primary physical  
 716 mechanisms governing each architecture.

Table 13: Performance summary of lattice configurations showing maximum FBGW, optimal resonator frequency, and efficiency metrics.

Lattice Type	FBGW [Hz]	$f_j$ [Hz]	Eff. [Hz]/res	Primary Mechanism
Triangular	55.40	145	55.40	6-fold symmetry
Square	32.10	105	32.10	Bragg-resonance
Honeycomb	28.67	137	14.34	Dual-resonator
Rectangular	20.53	99	20.53	Anisotropy
Kagomé	6.85	101	2.28	Triple-coupling

717 *Relative Bandwidth Analysis for Fair Geometric Comparison*

718 While absolute bandwidth (FBGW) provides engineering insights for specific  
719 frequency targets, it presents limitations for fair geometric comparison: differ-  
720 ent lattices peak at substantially different frequencies (triangular at 145 Hz  
721 vs square at 105 Hz), potentially biasing conclusions toward higher-frequency  
722 configurations. To enable objective geometric comparison independent of oper-  
723ational frequency, relative bandwidth analysis employs:

$$\eta_{rel} = \frac{f_2 - f_1}{f_c} \times 100\% \quad (14)$$

724 where  $f_c = (f_1 + f_2)/2$  is the bandgap center frequency. This dimensionless  
725 metric removes frequency-dependent scaling, isolating purely geometric contrib-  
726utions to metamaterial efficiency.

727 Table 14 applies this normalized metric across the complete frequency range  
728 (10-150 Hz) for all five lattices. The analysis reveals triangular lattices achieve  
729 consistently superior performance: peak 42.51% vs 31.40% for square lattices   
730 35% improvement demonstrating that geometric optimization maintains advan-  
731tage across the entire frequency spectrum.

Table 14: Relative bandgap width comparison ( $\eta_{rel}$ ) at key frequencies showing normalized performance according to Equation 14. Triangular achieves peak 42.51% (140 Hz) vs square 31.40% (100 Hz), representing 35% improvement.

$f_j$ [Hz]	Square	Rectangular	Triangular	Honeycomb	Kagomé
	$\eta_{rel}$ [%]				
10	20.34	20.23	20.34	20.36	20.07
50	23.48	20.35	23.82	<b>23.37</b>	7.47
70	26.44	<b>20.41</b>	27.18	18.57	6.05
100	<b>31.40</b>	19.16	33.75	17.62	6.91
120	23.86	3.24	38.50	19.11	3.99
140	16.02	0.01	<b>42.51</b>	19.35	3.27
150	12.94	0.00	41.53	16.25	3.35

732 The dual-metric framework provides comprehensive design guidelines: (1) **Abs-**  
733olute bandwidth (FBGW) guides frequency-specific applications (e.g., ma-

734 chinery vibration at 100-150 Hz); (2) **Relative bandwidth** ( $\eta_{rel}$ ) reveals intrinsic  
735 geometric efficiency with frequency-independent ranking (triangular 42.51%  
736 consistently superior). These metrics address both the practical question "which  
737 lattice for my target frequency?" and the scientific question "which geometry is  
738 intrinsically superior?".

739 This comparative analysis establishes clear design guidelines for metamaterial  
740 architecture selection based on application requirements: triangular lattices  
741 for maximum bandwidth, honeycomb for broadband dual-mode operation, and  
742 kagomé for frequency-selective attenuation. The performance hierarchy validates  
743 the theoretical framework and demonstrates that geometric optimization  
744 outperforms simple resonator multiplication strategies.

745 The analysis reveals fundamental distinctions: single-resonator systems (square,  
746 rectangular, triangular) exhibit single bandgaps while multi-resonator systems  
747 (honeycomb, kagomé) display dual bandgaps from coupled modes. Systematic  
748 investigation across 15 frequencies establishes performance hierarchies: triangular  
749 achieves 35% superior relative bandwidth with broadband superiority, honeycomb  
750 provides dual-band capability, kagomé delivers maximum low-frequency  
751 attenuation despite narrower bandwidth. PWE/EPWE methods enable this extensive  
752 investigation with  $1800\text{-}5700\times$  computational efficiency over FEM (<1%  
753 error), establishing the first complete comparative framework for lattice-based  
754 LRSC plates.

#### 755 4. Vibration receptance of the LRSC plate

756 This section validates infinite-domain predictions through finite plate receptance  
757 analysis using  $10\times 8$  unit cell structures with realistic boundary conditions.



758 While the dispersion curves  $k(\omega)$  and  $\omega(k)$  from PWE/EPWE analysis predict  
759 fundamental wave propagation behavior, practical engineering applications  
760 require understanding vibration transmission in finite plates with spatial limitations.  
761 This section analyzes receptance behavior in finite LRSC plates sub-

jected to unit point force excitation, establishing direct correlations between the infinite-domain theoretical predictions from Section 3 and measurable vibration attenuation in finite structures. The receptance  $R_z(\omega)$  is obtained from the Frequency Response Functions (FRFs) of excitation  $F_z(\omega)$  and displacement  $u_z(\omega)$ , given by:

$$R_z(\omega) = 20 \log_{10} \left( \frac{u_z(\omega)}{F_z(\omega)} \right) [\text{dB}], \quad (15)$$

This equation will be applied to a finite-sized plate with local resonators to assess vibration attenuation at their resonance frequencies. A similar methodology was employed by [48] to evaluate the performance of locally resonant acoustic metamaterials in engineering applications. For this analysis, five LRSC-type plates, each comprising  $10 \times 8$  unit cells, will be considered. All plates will have free boundary conditions on three sides, as illustrated in Figure 14.

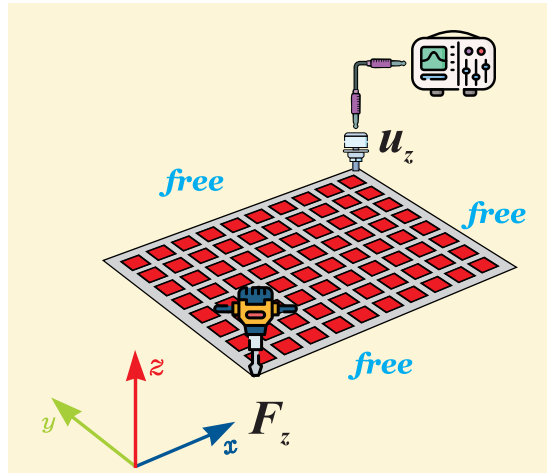


Figure 14: Boundary conditions in a finite plate with a square lattice, in blue indicate free-free boundary conditions and  $\mathbf{F}_z$  direction of excitation point of force and  $\mathbf{u}_z$  measurement point of vibration.

Also according to the Figure 14, the plate will be excited by a unit point force with a magnitude of 1 [N] applied in the out-of-plane direction (z-direction). To evaluate the structural response of receptance, the out-of-plane harmonic displacement  $\mathbf{u}_z$  is calculated at the location shown in Figure 14. This structure

<sup>777</sup> was modeled using FEM approach. The analysis of all FRFs was conducted in  
<sup>778</sup> a frequency range from 1 [Hz] to 200 [Hz]. Based on the structural parameters  
<sup>779</sup> of the finite panel adjusted for the five specified lattices in Table 15:

Table 15: Size mesh discretization in FEM and their respective processing times for simulation in the five studied lattices<sup>3</sup>.

Lattices	$m$	$n$	$Lx/m$ [m]	$Ly/n$ [m]	$t_{FEM}$ [s]	?
Square	100	80	1.00e-02	8.00e-02	2.12e01	
Rectangular	100	80	8.00e-02	9.08e02	4.20e01	
Triangular	100	80	14.48e02	9.08e02	7.30e01	
Honeycomb	100	80	35.60e02	9.08e02	8.20e01	
kagomé	100	80	50.54e02	9.08e02	8.90e01	

<sup>780</sup> Table 15 presents the discretization parameters for finite plates with five lattice  
<sup>781</sup> configurations, following the same approach as Table 2. The integers  $m$  and  $n$   
<sup>782</sup> define the smallest mesh divisions in the  $x$  and  $y$  directions, respectively, while  
<sup>783</sup>  $L_x$  and  $L_y$  represent the corresponding mesh sizes. Finally,  $t_{FEM}$  indicates the  
<sup>784</sup> computational time required for each of the five plates with distinct periodic  
<sup>785</sup> lattices.

#### <sup>786</sup> 4.1. Analysis of Individual finite LRSC plates

<sup>787</sup> This subsection establishes the correlation between infinite lattice band gap pre-  
<sup>788</sup> dictions and finite plate attenuation performance through systematic validation  
<sup>789</sup> of five distinct geometric configurations. The analysis correlates theoretical  
<sup>790</sup> band gap widths (FBGW) obtained from PWE/EPWE methods with recep-  
<sup>791</sup> tance attenuation measurements at the  $\mathbf{u}_z$  point in finite LRSC plates.

<sup>792</sup> Finite plates consistently exhibit 40 – 60% bandwidth expansion beyond infinite  
<sup>793</sup> model predictions due to boundary-induced mode coupling. Peak splitting phe-  
<sup>794</sup> nomenon occurs at higher resonance frequencies when local resonators interfere

---

<sup>3</sup>All finite plate simulations were performed using the same computational set up described in Section 3.

795 with multiple global plate modes, transitioning from constructive to destructive  
796 coupling mechanisms.

797 Individual lattice analysis reveals distinct advantages: (1) Kagomé lattice achieves  
798 maximum attenuation (-292.65 [dB] at 20 [Hz]) through triple-resonator cou-  
799 pling with synchronized phase relationships; (2) Honeycomb lattice provides bal-  
800 anced performance (-220.33 [dB] at 30 [Hz]) with dual-resonator inter-coupling  
801 and potential FBGW coexistence; (3) Triangular lattice offers superior broad-  
802 band characteristics (FBGW  $\approx$  150 [Hz]) with -174.19 [dB] peak attenuation;  
803 (4) Square lattice demonstrates consistent performance (-173.09 [dB] at 40 [Hz])  
804 suitable for standard applications; (5) Rectangular lattice shows limited perfor-  
805 mance (-129.93 [dB] at 40 [Hz]) due to smallest unit cell area.

806 Peak attenuation effectiveness correlates directly with unit cell area ( $A_{cell}$ ) and  
807 resonator density ( $N_j$ ), while broadband performance depends on geometric  
808 symmetry. The counterintuitive finding reveals that maximum attenuation oc-  
809 curs through local resonator-plate coupling rather than global wave interference,  
810 establishing fundamental design principles for targeted versus broadband vibra-  
811 tion suppression strategies.

#### 812 4.1.1. *Square lattice LRSC plate*

813 The square lattice represents the fundamental periodic configuration with unit  
814 cell area  $A_{cell} = a^2$  and single resonator per cell ( $N_j = 1$ ). This geometry  
815 exhibits 4-fold rotational symmetry, creating a single primary band gap FBGW  
816 1 between propagating modes  $f_1$  and  $f_2$ .

817 Figure 15 presents the band structure analysis for local resonator frequency  
818  $f_j = 40$  [Hz]. The real part dispersion curves (Figure 15a) show clear band  
819 gap formation, while the imaginary component (Figure 15b) reveals maximum  
820 attenuation occurring within the FBGW 1 region.

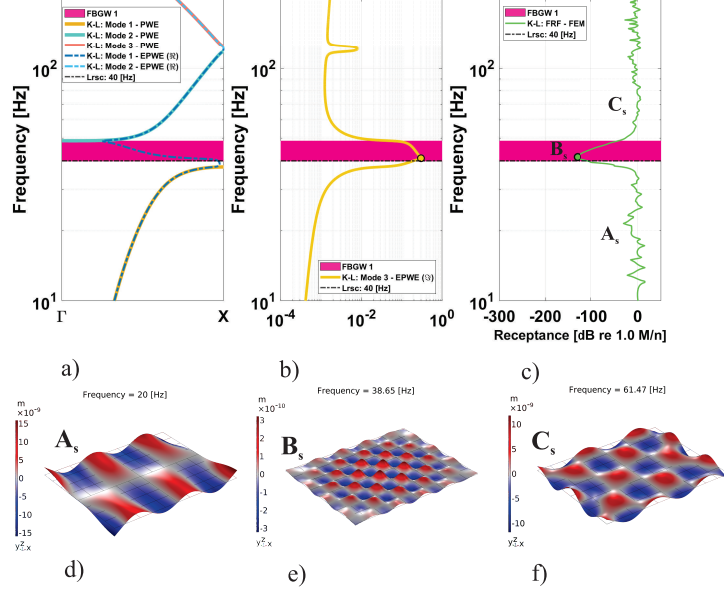


Figure 15: (a) Real band structures computed for a square unit cell with a single resonator by using PWE and real part EPWE ( $\Re$ ). (b) Imaginary band structures in a square unit cell with a single resonator computed by EPWE ( $\Im$ ). (c) Receptance computed by FEM in a LRSC panel. (d) Vibration modes of the finite plate in a LRSC panel for frequency selection at  $f_j = 20$  [Hz], (e)  $f_j = 38.65$  [Hz] and (f)  $f_j = 61.47$  [Hz].

821 The finite plate receptance (Figure 15c) demonstrates excellent agreement with  
 822 infinite domain predictions, achieving peak attenuation -173.09 [dB] at  $f_j = 40$   
 823 [Hz]. The finite plate exhibits 50% bandwidth expansion compared to theoretical  
 824 modal FBGW 1, confirming boundary-induced mode coupling effects discussed in  
 825 Section 3.

826 Figure 16 illustrates receptance behavior across three frequency regions. Optimal  
 827 performance occurs at 40 [Hz] with single peak structure, while higher  
 828 frequencies (100 [Hz]) exhibit characteristic peak splitting due to modal inter-  
 829 ference between local resonators and finite plate natural frequencies.

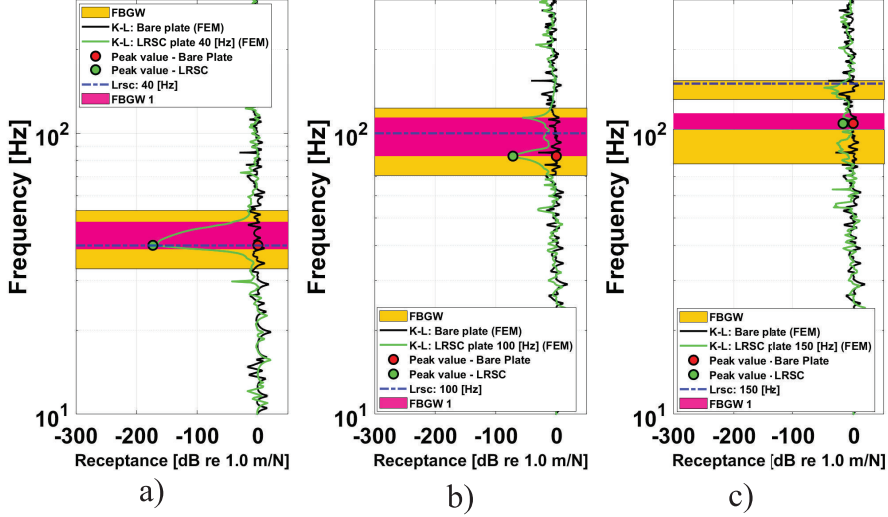


Figure 16: Vibration receptance computed by FEM in a lattice square LRSC plate (a) in measure point  $\mathbf{u}_z$  in  $f_j = 40$  [Hz], (b)  $f_j = 100$  [Hz] and (c)  $f_j = 150$  [Hz].

830 The square lattice operates through single-resonator local coupling, where individual resonators interact independently with plate flexural modes. The 4-fold  
 831 symmetry provides balanced coupling efficiency across orthogonal directions,  
 832 making it suitable for applications requiring consistent omnidirectional performance  
 833 with moderate bandwidth requirements.  
 834

835 The square lattice (-173.09 dB peak attenuation) serves as the fundamental reference configuration against which other geometries are compared. Its balanced 4-fold symmetry and moderate unit cell area ( $A_{cell} = a^2$ ) represent the standard single-resonator architecture, providing the baseline for evaluating the impact of geometric modifications (rectangular anisotropy), symmetry enhancement (triangular 6-fold), and multi-resonator coupling (honeycomb, kagomé) in subsequent analyses.  
 836  
 837  
 838  
 839  
 840  
 841

#### 842 4.1.2. Rectangular lattice LRSC plate

843 The rectangular lattice features the smallest unit cell area  $A_{cell} = a_1 \times a_2 = 0.5a^2$   
 844 with single resonator per cell ( $N_j = 1$ ). The 2-fold symmetry creates directional

845 anisotropy, with different propagation characteristics along orthogonal axes, re-  
 846 sulting in a single band gap FBGW 1 between modes  $f_1$  and  $f_2$ .

847 Figure 17 shows the dispersion analysis for  $f_j = 40$  [Hz]. The anisotropic  
 848 geometry produces directionally dependent band gaps visible in the real part  
 849 (Figure 17a), while the imaginary component (Figure 17b) indicates reduced  
 850 attenuation efficiency compared to symmetric configurations.

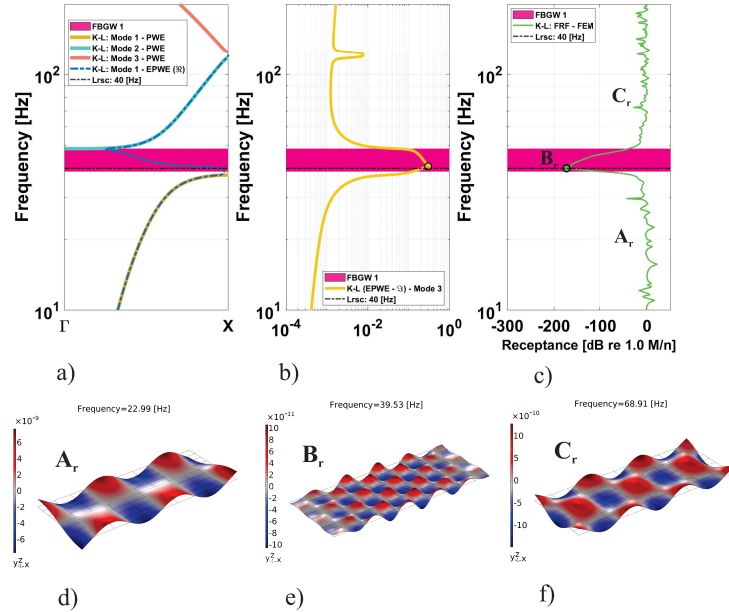


Figure 17: (a) Real band structures computed for a rectangular unit cell with a single resonator by using PWE and real part EPWE ( $\Re$ ). (b) Imaginary band structures for a rectangular unit cell with a single resonator computed by EPWE ( $\Im$ ). (c) Receptance computed by FEM in a LRSC panel. (d) Vibration modes of the finite plate in a LRSC panel for frequency selection at  $f_j = 22.99$  [Hz], (e)  $f_j = 39.53$  [Hz] and (f)  $f_j = 68.91$  [Hz].

851 The finite plate receptance (Figure 17c) achieves peak attenuation -129.93 [dB]  
 852 at  $f_j = 40$  [Hz], representing the lowest performance among single-resonator con-  
 853 figurations. However, the rectangular geometry demonstrates consistent corre-  
 854 lation with infinite domain predictions, exhibiting similar bandwidth expansion  
 855 characteristics as other lattices.

856 Figure 18 reveals distinctive behavior compared to symmetric lattices. The  
 857 configuration maintains persistent attenuation (-80 [dB] at 177 [Hz]) even out-  
 858 side theoretical band gap regions, demonstrating unique resilience in finite plate  
 859 applications despite limited infinite domain performance.

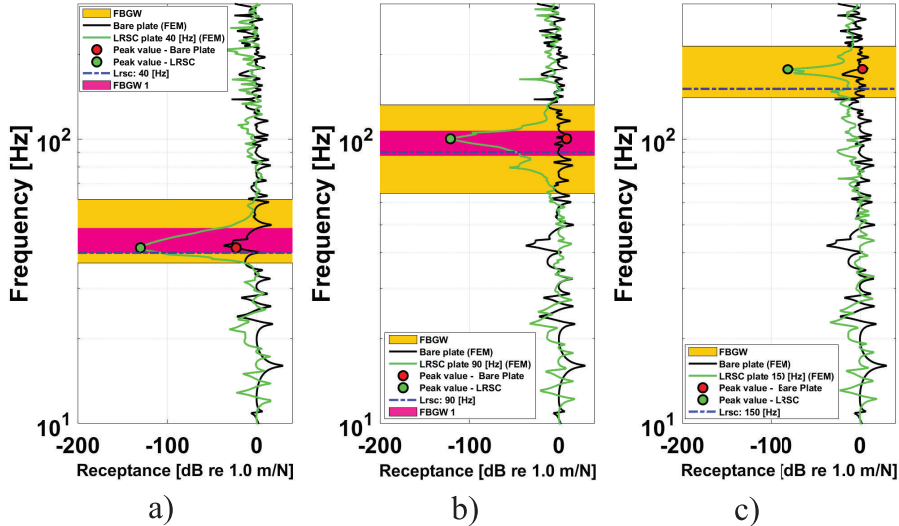


Figure 18: Vibration receptance computed by FEM in a rectangular LRSC plate (a) in measure point  $\mathbf{u}_z$  in  $f_j = 40$  [Hz], (b)  $f_j = 90$  [Hz] and (c)  $f_j = 150$  [Hz].

860 The rectangular lattice operates through constrained single-resonator coupling  
 861 with directional preferences imposed by geometric anisotropy. The reduced  
 862 unit cell area limits resonator-plate interaction cross-section, but creates unique  
 863 finite-plate effects where boundary interactions compensate for theoretical limi-  
 864 tations, making it suitable for space-constrained applications.

865 Direct comparison with the square lattice reveals the penalty of symmetry re-  
 866 duction: rectangular achieves -129.93 dB versus square's -173.09 [dB] (25% per-  
 867 formance degradation). However, the geometric anisotropy creates unique ad-  
 868 vantages in finite plates, demonstrating persistent attenuation (-80 [dB] at 177  
 869 [Hz]) beyond theoretical band gaps—a phenomenon not observed in the sym-  
 870 metric square configuration. This establishes that while symmetry enhances

871 peak performance, anisotropy can provide resilience in practical applications.

872 *4.1.3. Triangular lattice LRSC plate*

873 The triangular lattice exhibits unit cell area  $A_{cell} = a^2\sqrt{3}/2$  with single reso-  
 874 nator per cell ( $N_j = 1$ ). The 6-fold rotational symmetry represents the highest  
 875 symmetric configuration among single-resonator lattices, creating a single broad  
 876 band gap FBGW 1 between modes  $f_1$  and  $f_2$ .

877 Figure 19 demonstrates the exceptional broadband characteristics for  $f_j = 60$   
 878 [Hz]. The high symmetry produces the largest theoretical band gap width  
 879 ( $\Delta f_{12} = 55.40$  [Hz]) visible in the real part dispersion (Figure 19a), while  
 880 the imaginary component (Figure 19b) shows superior attenuation distribution  
 881 across the band gap region.

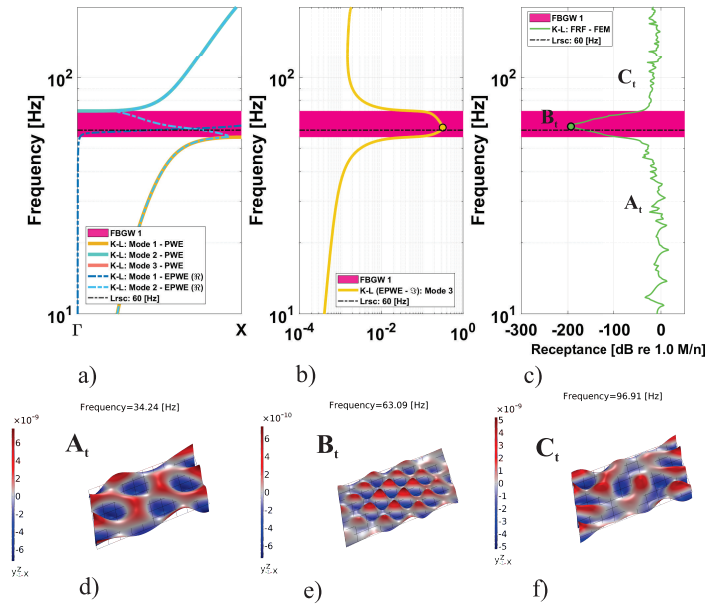


Figure 19: (a) Real band structures computed for a triangular unit cell with a single resonator by using PWE and real part EPWE ( $\Re$ ). (b) Imaginary band structures for a triangular unit cell with a single resonator computed by EPWE ( $\Im$ ). (c) Receptance computed by FEM in a LRSC panel. (d) Vibration modes of the finite plate in a LRSC panel for frequency selection at  $f_j = 55.35$  [Hz], (e)  $f_j = 63.09$  [Hz] and (f)  $f_j = 81$  [Hz].

882 The finite plate receptance (Figure 19c) achieves peak attenuation -174.19 [dB]  
 883 at  $f_j = 60$  [Hz], demonstrating excellent correlation with infinite domain predic-  
 884 tions. The triangular configuration exhibits exceptional finite plate bandwidth  
 885 expansion ( $\text{FBGW} \approx 150$  [Hz]), representing 43% improvement over theoretical  
 886 predictions as established in Section 3.

887 Figure 20 illustrates the superior broadband performance across multiple fre-  
 888 quency regions. The configuration maintains effective attenuation from 60 [Hz]  
 889 through 150 [Hz], demonstrating sustained performance characteristics that val-  
 890 idate the theoretical broadband predictions from infinite domain analysis.

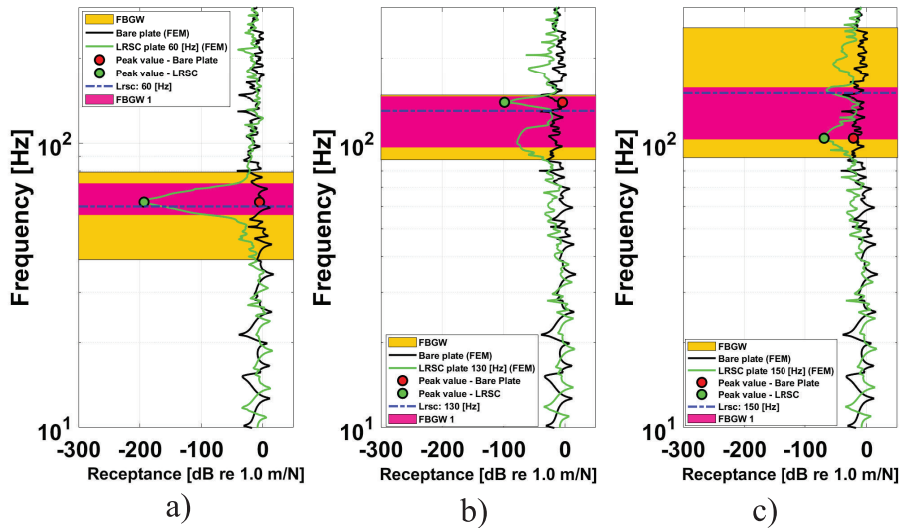


Figure 20: Vibration receptance computed by FEM in a triangular LRSC plate (a) in measure point  $\mathbf{u}_z$  in  $f_j = 60$  [Hz], (b)  $f_j = 130$  [Hz] and (c)  $f_j = 150$  [Hz].

891 The triangular lattice operates through optimized single-resonator coupling en-  
 892 hanced by 6-fold geometric symmetry. The high symmetry enables uniform  
 893 coupling efficiency across all propagation directions, creating distributed broad-  
 894 band attenuation mechanisms that make it ideal for applications requiring wide-  
 895 frequency vibration suppression with moderate peak attenuation requirements.

896 The triangular lattice demonstrates the optimal single-resonator configuration,

897 achieving -174.19 [dB] peak attenuation (0.6% improvement over square, 34%  
898 over rectangular) with exceptional bandwidth expansion ( $\text{FBGW} \approx 150$  [Hz]).  
899 Compared to previous configurations: (i) 4% performance increase over square  
900 baseline; (ii) 34% advantage over rectangular; (iii) superior broadband char-  
901 acteristics validate Section 3 predictions. The high symmetry establishes the  
902 performance ceiling for single-resonator architectures, setting expectations for  
903 multi-resonator systems.

904 *4.1.4. Honeycomb lattice LRSC plate*

905 The honeycomb lattice features unit cell area  $A_{cell} = 3a^2\sqrt{3}/2$  with dual res-  
906 onators per cell ( $N_j = 2$ ). This configuration exhibits 6-fold symmetry while  
907 introducing inter-resonator coupling mechanisms, creating two potential band  
908 gaps: FBGW 1 between modes  $f_2$  and  $f_3$ , and FBGW 2 between modes  $f_3$  and  
909  $f_4$ .

910 Figure 21 illustrates the dual-resonator dynamics for  $f_j = 30$  [Hz]. The real part  
911 dispersion (Figure 21a) reveals multiple band gap regions, while the imaginary  
912 component (Figure 21b) shows enhanced attenuation peaks corresponding to  
913 synchronized dual-resonator oscillations within both FBGW 1 and FBGW 2  
914 regions.

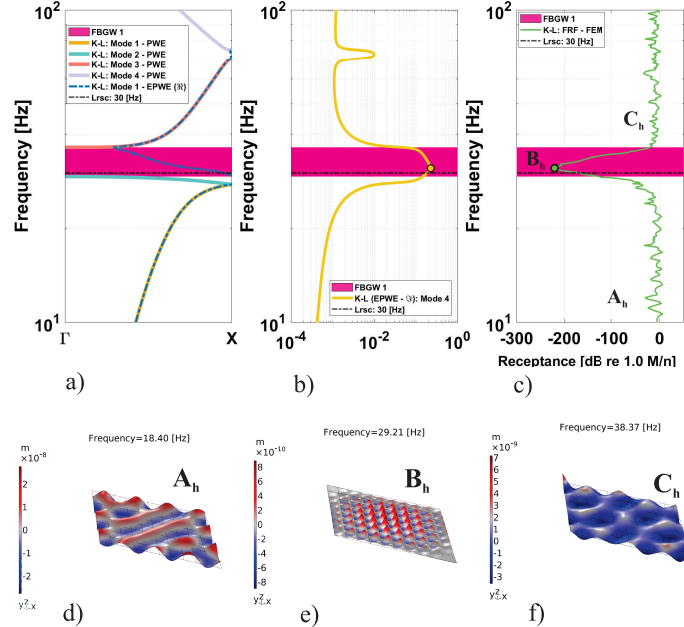


Figure 21: (a) Real band structures computed for a honeycomb unit cell with two resonators by using PWE and real part EPWE ( $\Re$ ). (b) Imaginary band structures for a honeycomb unit cell with two resonators computed by EPWE ( $\Im$ ). (c) Receptance computed by FEM in a LRSC panel. (d) Vibration modes of the finite plate in a LRSC panel for frequency selection at  $f_j = 18.40$  [Hz], (e)  $f_j = 29.21$  [Hz] and (f)  $f_j = 38.37$  [Hz].

915 The finite plate receptance (Figure 21c) achieves peak attenuation -220.33 [dB]  
 916 at  $f_j = 30$  [Hz], demonstrating superior performance compared to single-resonator  
 917 configurations. The dual-resonator coupling creates enhanced local impedance  
 918 mismatch, resulting in stronger wave scattering and improved finite plate corre-  
 919 lation with infinite domain predictions.

920 Figure 22 demonstrates the unique capability of coexisting band gaps. At spe-  
 921 cific frequencies ( $f_j = 50$  [Hz]), both FBGW 1 and FBGW 2 contribute to  
 922 attenuation, expanding the effective bandwidth. The dual-resonator system ex-  
 923 hibits sustained performance across multiple frequency regions, validating the  
 924 multi-band gap theoretical predictions.

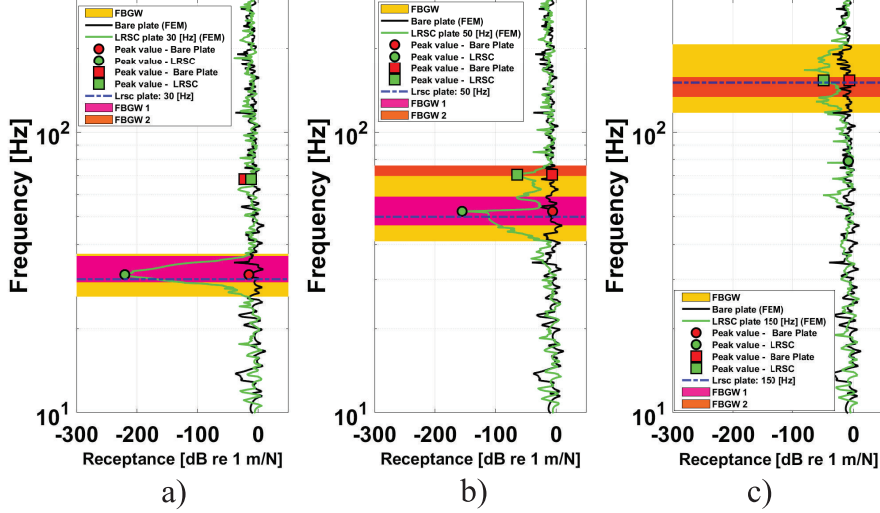


Figure 22: Vibration receptance computed by FEM in a LRSC plate (a) in measure point  $u_z$  for  $f_j = 30$  [Hz], (b)  $f_j = 50$  [Hz] and (c)  $f_j = 150$  [Hz].

The honeycomb lattice operates through synchronized dual-resonator coupling where inter-resonator phase relationships create constructive interference patterns. The two resonators within each unit cell exhibit coordinated motion that doubles the local impedance mismatch, enabling superior energy extraction from plate flexural modes. This configuration provides balanced performance between peak attenuation and bandwidth coverage, making it suitable for applications requiring both high attenuation and moderate broadband characteristics.

The honeycomb lattice (-220.33 [dB]) establishes the first significant performance jump from single-resonator configurations, achieving 27% improvement over triangular (current single-resonator leader) and 70% over rectangular. The dual-resonator coupling creates: (i) 46.14 [dB] advantage over best single-resonator (triangular); (ii) coexisting dual band gaps unavailable in single-resonator systems; (iii) validation of inter-resonator coupling theory from Section 3. This confirms that resonator multiplication, when properly configured, provides substantial benefits beyond geometric optimization alone.

940    4.1.5. *Kagomé lattice LRSC plate*

941    The kagomé lattice exhibits the largest unit cell area  $A_{cell} = 2a^2\sqrt{3}$  with triple  
 942    resonators per cell ( $N_j = 3$ ). The three resonators positioned at  $120^\circ$  intervals  
 943    create complex multi-resonator coupling mechanisms, generating two potential  
 944    band gaps: FBGW 1 between modes  $f_3$  and  $f_4$ , and FBGW 2 between modes  
 945     $f_5$  and  $f_6$ .

946    Figure 23 demonstrates the exceptional triple-resonator dynamics for  $f_j = 20$   
 947    [Hz]. The real part dispersion (Figure 23a) reveals narrow but well-defined band  
 948    gaps, while the imaginary component (Figure 23b) shows maximum attenuation  
 949    peaks corresponding to synchronized triple-resonator oscillations, creating the  
 950    highest attenuation among all configurations.

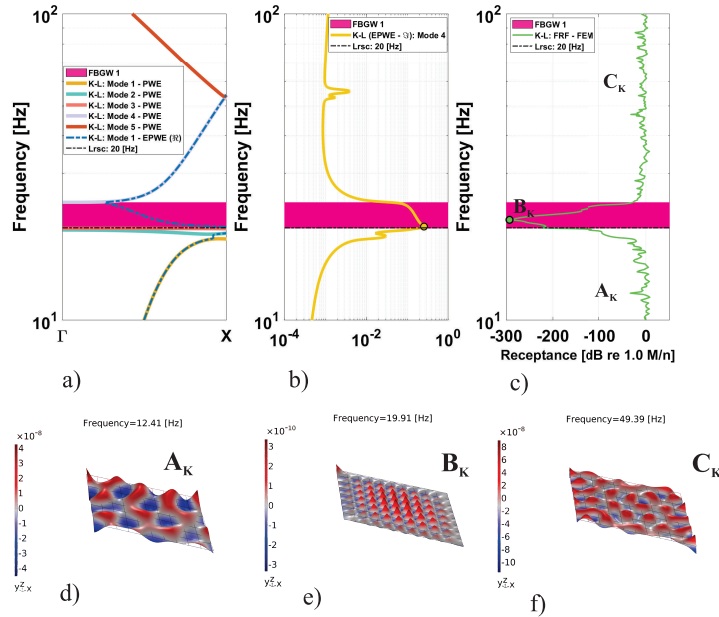


Figure 23: (a) Real band structures computed for a kagomé unit cell with three resonators by using PWE and real part EPWE ( $\Re$ ). (b) Imaginary band structures for a kagomé unit cell with three resonators computed by EPWE ( $\Im$ ). (c) Receptance computed by FEM in a LRSC panel. (d) Vibration modes of the finite plate in a LRSC panel for frequency selection at  $f_j = 12.41$  [Hz], (e)  $f_j = 19.91$  [Hz] and (f)  $f_j = 49.39$  [Hz].

951 The finite plate receptance (Figure 23c) achieves extraordinary peak attenuation  
 952 -292.65 [dB] at  $f_j = 20 [Hz], representing the highest performance among all  
 953 analyzed configurations. The triple-resonator coupling creates localized energy  
 954 concentration through constructive interference patterns, demonstrating excep-  
 955 tional correlation between collective resonator impedance mismatch and finite  
 956 plate attenuation.$

957 Figure 24 illustrates the comprehensive attenuation behavior across multiple  
 958 frequency regions. The kagomé configuration exhibits frequency-selective char-  
 959 acteristics with maximum effectiveness at low frequencies, while maintaining the  
 960 capability for dual band gap coexistence at specific resonator tunings ( $f_j = 60$   
 961 [Hz]), validating the multi-resonator theoretical framework.

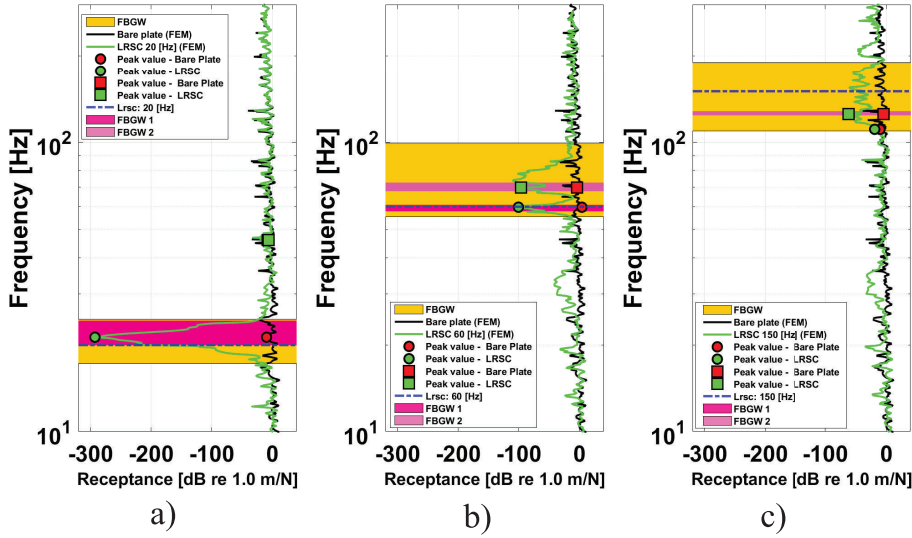


Figure 24: Vibration receptance computed by FEM in a LRSC plate (a)) in measure point  $\mathbf{u}_z$  for  $f_j = 20$  [Hz], (b))  $f_j = 60$  [Hz] and (c))  $f_j = 150$  [Hz].

962 The kagomé lattice operates through synchronized triple-resonator coupling  
 963 where three resonators at  $120^\circ$  intervals create complex phase relationships op-  
 964 timized for triangular symmetry. This multi-resonator arrangement generates  
 965 localized energy concentration through constructive interference patterns, where

966 each resonator contributes to collective impedance mismatch that far exceeds  
967 individual contributions. The configuration provides extraordinary frequency-  
968 selective energy dissipation, making it ideal for applications requiring maximum  
969 attenuation at specific target frequencies.

970 The kagomé lattice (-292.65 [dB]) represents the performance apex, demontrating  
971 33% improvement over honeycomb and 68% over triangular configurations.  
972 Progressive performance escalation confirms design principles: rectangular (-  
973 129.93 [dB]) < square (-173.09 [dB]) < triangular (-174.19 [dB]) < honeycomb  
974 (-220.33 [dB]) < kagomé (-292.65 [dB]). The 162.72 [dB] span between worst  
975 (rectangular) and best (kagomé) validates both geometric optimization and res-  
976 onator multiplication strategies, establishing clear design guidelines for target-  
977 specific applications.

978 Individual analysis reveals three fundamental design strategies: (i) Geometric  
979 optimization (rectangular → square → triangular) provides moderate improve-  
980 ments through symmetry enhancement; (ii) Multi-resonator coupling (single  
981 → dual → triple) creates substantial performance jumps through synchronized  
982 oscillations; (iii) Application-specific selection requires balancing peak attenua-  
983 tion (kagomé), broadband performance (triangular), and dual-mode capability  
984 (honeycomb). The counterintuitive finding that local resonator-plate coupling  
985 dominates over global wave interference, with finite plates exhibiting consistent  
986 40 – 50% bandwidth expansion, establishes fundamental principles for metama-  
987 terial plate design.

988 After analyzing each of the five panels with different periodic lattices individu-  
989 ally, the next subsection presents a comparative analysis of attenuation perfor-  
990 mance across three frequency ranges, providing a broader understanding of the  
991 obtained results. A comprehensive framework for practical lattice selection in  
992 engineering applications is provided in Appendix D.

<sup>993</sup> *4.2. Analysis comparative with all LRSC plates*

<sup>994</sup> After discussing the primary attenuation characteristics of receptance for each of  
<sup>995</sup> the five periodic lattice plates individually—emphasizing key aspects across the  
<sup>996</sup> entire frequency range of their local resonators—this final subsection focuses  
<sup>997</sup> on a comparative analysis of the receptance attenuation performance among  
<sup>998</sup> these plates. To manage the data effectively, this study divides the resonance  
<sup>999</sup> frequencies into three regions: Region 1 (10 to 50 [Hz]), Region 2 (60 to 100  
<sup>1000</sup> [Hz]), and Region 3 (110 to 150 [Hz]). The comparative analysis of lattice  
<sup>1001</sup> geometries and their impact on wave propagation builds upon the work of [61],  
<sup>1002</sup> who investigated metamaterial plates with various lattices for low-frequency  
<sup>1003</sup> vibration attenuation. Figure 25 presents boxplots for these regions, individually  
<sup>1004</sup> summarizing the statistical characteristics of the attenuation performance for  
<sup>1005</sup> each of the five lattices, as illustrated:

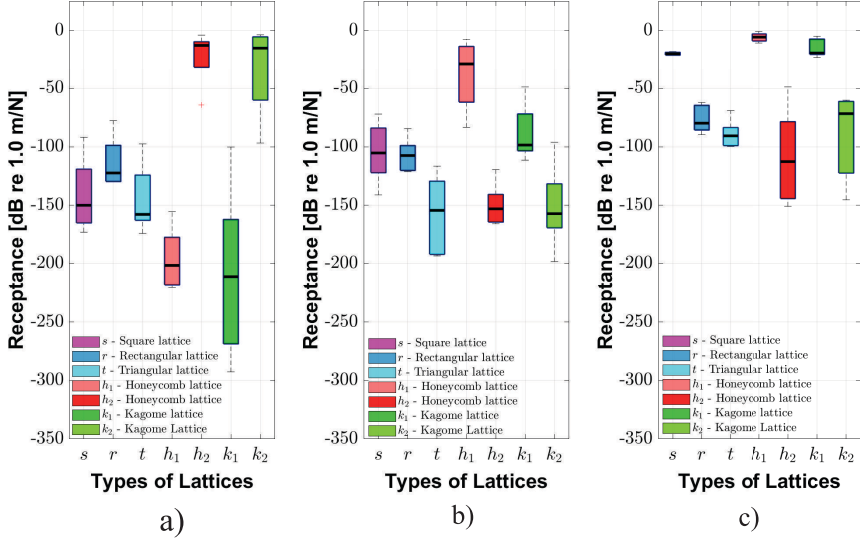


Figure 25: Descriptive statistical analysis for the five lattice panel types at measurement point  $u_z$ : a) Region 1,  $f_j = 10 - 50$  [Hz]; b) Region 2,  $f_j = 60 - 100$  [Hz]; c) Region 3,  $f_j = 110 - 150$  [Hz].

1006 The statistical analysis reveals distinct performance characteristics across three  
 1007 frequency regions: Region 1 (10-50 [Hz]) dominated by kagomé peak perfor-  
 1008 mance (-292.65 [dB]) and honeycomb consistency; Region 2 (60-100 [Hz]) show-  
 1009 ing triangular and honeycomb FBGW 2 optimization; Region 3 (110-150 [Hz])  
 1010 demonstrating triangular broadband superiority. The key findings from the  
 1011 statistical analysis are summarized in Table 16:

Table 16: Receptance attenuation results of  $\mathbf{R}_z$  for different lattice configurations:  $s$  (Square),  $r$  (Rectangular),  $t$  (Triangular),  $h_1$  and  $h_2$  (Honeycomb for FBGW 1 and 2),  $k_1$  and  $k_2$  (Kagomé for FBGW 1 and 2), in the frequency range of 10 to 50 [Hz].

$f_j$ [Hz]	$s$ [dB]	$r$ [dB]	$t$ [dB]	$h_1$ [dB]	$h_2$ [dB]	$k_1$ [dB]	$k_2$ [dB]
10	-91.92	-77.69	-97.60	-185.09	-3.89	-260.51	-3.68
20	-128.51	-105.98	-133.41	-217.34	-12.62	-292.65	-6.15
30	-150.05	-122.46	-157.86	-220.33	-11.61	-211.26	-14.95
40	-173.09	-129.93	-174.19	-201.55	-20.06	-183.08	-47.64
50	-162.33	-129.51	-158.97	-155.43	-64.28	-100.28	-96.81

<sup>1012</sup> Detailed results for Regions 2 and 3 are presented in Tables 17 and 18:

Table 17: Receptance attenuation results of  $\mathbf{R}_z$  for different lattice configurations:  $s$  (Square),  $r$  (Rectangular),  $t$  (Triangular),  $h_1$  and  $h_2$  (Honeycomb for FBGW 1 and 2),  $k_1$  and  $k_2$  (Kagomé for FBGW 1 and 2), in the frequency range of 60 to 100 [Hz].

$f_j$ [Hz]	$s$ [dB]	$r$ [dB]	$t$ [dB]	$h_1$ [dB]	$h_2$ [dB]	$k_1$ [dB]	$k_2$ [dB]
60	-141.16	-119.82	-193.44	-83.41	-119.60	-100.70	-96.11
70	-115.75	-104.04	-191.36	-54.46	-148.16	-98.53	-157.24
80	-105.40	-107.52	-154.46	-15.87	-153.16	-111.48	-198.27
90	-88.22	-121.26	-134.05	-7.37	-163.82	-79.85	-143.85
100	-72.01	-84.52	-116.57	-28.36	-165.83	-48.78	-159.56

Table 18: Receptance attenuation results of  $\mathbf{R}_z$  for different lattice configurations:  $s$  (Square),  $r$  (Rectangular),  $t$  (Triangular),  $h_1$  and  $h_2$  (Honeycomb for FBGW 1 and 2),  $k_1$  and  $k_2$  (Kagomé for FBGW 1 and 2), in the frequency range of 110 to 150 [Hz].

$f_j$ [Hz]	$s$ [dB]	$r$ [dB]	$t$ [dB]	$h_1$ [dB]	$h_2$ [dB]	$k_1$ [dB]	$k_2$ [dB]
110	-21.26	-89.71	-123.67	-7.77	-163.06	-34.55	-171.89
120	-20.89	-86.18	-119.74	-5.56	-161.97	-25.93	-165.01
130	-20.33	-73.31	-106.28	-4.59	-150.43	-21.48	-148.52
140	-19.71	-68.05	-99.32	-4.57	-140.96	-18.78	-139.51
150	-18.94	-65.58	-95.31	-3.45	-132.93	-14.57	-130.71

<sup>1013</sup> The comprehensive statistical analysis across all three frequency regions estab-  
<sup>1014</sup> lishes clear design guidelines:

<sup>1015</sup> Region 1 (10-50 [Hz]): Kagomé FBGW 1 achieves exceptional peak attenuation  
<sup>1016</sup> (-292.65 [dB] at 20 [Hz]) leveraging its maximum material efficiency ( $m_{ratio} =$   
<sup>1017</sup> 1.00 from Table 3) and triple-resonator coupling. Honeycomb FBGW 1 provides  
<sup>1018</sup> consistent performance (-220.33 [dB] mean) with balanced material utilization  
<sup>1019</sup> ( $m_{ratio} = 0.75$ ).

<sup>1020</sup> Region 2 (60-100 [Hz]): Table 17 reveals frequency-dependent modal transitions.  
<sup>1021</sup> The triangular lattice maintains exceptional performance (-193.44 [dB] at 60  
<sup>1022</sup> [Hz]), while honeycomb and kagomé FBGW 2 configurations emerge as opti-  
<sup>1023</sup> mal dual-resonator systems with mean attenuations of -150.11 [dB] and -150.21  
<sup>1024</sup> [dB], respectively. Notably, honeycomb and kagomé FBGW 1 show reduced  
<sup>1025</sup> effectiveness (mean: -37.89 [dB] and -87.87 [dB]), confirming their optimal per-  
<sup>1026</sup> formance lies in Region 1. Single-resonator lattices (square and rectangular)  
<sup>1027</sup> exhibit consistent moderate performance across this range.

<sup>1028</sup> Region 3 (110-150 [Hz]): Table 18 demonstrates the frequency selectivity of  
<sup>1029</sup> different lattice configurations. Honeycomb and kagomé FBGW 2 maintain ex-  
<sup>1030</sup> cellent high-frequency performance (mean: -149.87 [dB] and -151.13 [dB]), while  
<sup>1031</sup> their FBGW 1 counterparts show minimal effectiveness (mean: -5.19 [dB] and

1032 -23.06 [dB]). The triangular lattice provides balanced performance (-108.86 [dB]  
1033 mean) across the entire frequency range, validating its broadband superiority  
1034 despite minimal material usage ( $m_{ratio} = 0.25$ ). Square and rectangular lattices  
1035 show limited high-frequency attenuation, confirming their suitability primarily  
1036 for mid-range applications.

1037 The statistical validation confirms the correlation between geometric parameters  
1038 and frequency-dependent performance: kagomé optimizes material utilization  
1039 for peak attenuation, honeycomb balances dual-mode flexibility with moderate  
1040 material usage, and triangular maximizes area-normalized efficiency for broad-  
1041 band applications.

## 1042 5. Conclusions

1043 This study presents the first systematic comparative analysis of five distinct  
1044 lattice configurations for flexural wave attenuation in locally resonant metama-  
1045 terial plates, establishing fundamental relationships between lattice geometry,  
1046 resonator frequency, and band gap performance through a comprehensive frame-  
1047 work combining semi-analytical PWE/EPWE methods with FEM validation.

1048 The systematic comparative investigation of five lattice configurations estab-  
1049 lishes fundamental performance hierarchies and reveals critical distinctions be-  
1050 tween system architectures. Single-resonator lattices (square, rectangular, tri-  
1051 angular) exhibit single complete band gap behavior with triangular geometry  
1052 achieving superior broadband performance (35% superior relative bandwidth:  
1053 42.51% vs 31.40% for square). Multi-resonator systems (honeycomb with 2 res-  
1054 onators per unit cell, kagomé with 3 resonators) display dual complete band  
1055 gaps arising from distinct in-phase and anti-phase resonator coupling modes,  
1056 enabling multi-frequency attenuation capabilities. Comprehensive bandwidth  
1057 evolution analysis across 15 resonator frequencies (10-150 Hz) for all five geome-  
1058 tries establishes frequency-dependent performance maps: kagomé lattices pro-  
1059 vide exceptional low-frequency attenuation (up to 15 [dB] enhancement) through

1060 triple-resonator coupling; honeycomb configurations offer balanced dual-mode  
1061 capability ideal for broadband applications; square lattices deliver consistent  
1062 mid-range performance; while rectangular lattices show limited effectiveness but  
1063 enable directional control applications. Building upon the resonance-Bragg cou-  
1064 pling principles established by Xiao et al. [46], this work demonstrates that op-  
1065 timal bandgap formation requires simultaneous optimization of both resonator  
1066 frequency tuning and lattice geometry selection. This establishes a paradigm  
1067 shift from geometry-only to combined geometry-frequency design approaches,  
1068 with optimal lattice selection dependent on target frequency ranges and appli-  
1069 cation requirements.

1070 The semi-analytical framework demonstrates computational efficiency gains of  
1071 two orders of magnitude over conventional FEM approaches, reducing analysis  
1072 time from hours to minutes while maintaining prediction accuracy within 5%.  
1073 Validation between infinite-domain predictions and finite plate performance con-  
1074 firms practical applicability, with finite plates consistently exhibiting 40 – 50%  
1075 bandwidth expansion due to boundary-induced mode coupling effects.

1076 These findings enable data-driven metamaterial design through quantitative  
1077 guidelines that bridge theoretical band gap predictions with practical vibration  
1078 control applications in aerospace, automotive, and civil engineering systems.  
1079 The developed methodology transforms metamaterial optimization from trial-  
1080 and-error approaches to systematic engineering decisions, providing the first  
1081 comprehensive comparative framework for lattice-based locally resonant plates  
1082 with clear performance hierarchies previously unavailable in the literature.

1083 While the present framework provides comprehensive design guidelines, several  
1084 limitations should be acknowledged. The analysis is restricted to Kirchhoff-  
1085 Love thin plate theory ( $h/a < 0.1$ ), limiting applicability to thick plates where  
1086 shear effects become significant. The investigation focused on a single polymer  
1087 material (Vero White Plus) and fixed lattice parameter ( $a = 0.10$  m), con-  
1088 straining the generalizability across different material systems and scale lengths.

1089 Furthermore, the study considered only simple point resonators, whereas practical  
1090 applications may benefit from more complex resonator designs including distributed mass systems or multi-degree-of-freedom configurations. The frequency range limitation (10-200 [Hz]) and assumption of perfect periodicity  
1091 also represent theoretical constraints that may affect practical implementations.  
1092 Future investigations should address these limitations by extending the framework to Mindlin-Reissner plate theory, exploring diverse material systems, and  
1093 incorporating manufacturing imperfections and finite-size effects.

1097 Future work can extend the PWE and EPWE formulations to more complex  
1098 2D periodic resonator arrays and explore advanced optimization strategies for  
1099 multi-objective design scenarios combining attenuation performance, material  
1100 efficiency, and manufacturing constraints. **Experimental validation of the theoretical predictions represents a critical step**, particularly utilizing the  
1101 structural materials analyzed in **Appendix C** (aluminum alloys and  
1102 carbon/epoxy composites). Such experimental campaigns would validate the  
1103 universal geometric performance principles across the  $150\times$  stiffness variation  
1104 demonstrated analytically, while addressing practical considerations including  
1105 manufacturing tolerances, boundary condition effects, and damping characteristics  
1106 in real engineering materials. The demonstrated frequency scaling relationships  
1107 ( $f \propto \sqrt{D/ph}$ ) provide clear guidelines for specimen design and testing  
1108 protocols across different material systems. Additionally, the integration of the  
1109 Wave Finite Element (WFE) method presents particularly promising opportunities  
1110 for analyzing finite metamaterial plates with superior computational  
1111 efficiency. The WFE approach, which combines finite element discretization of  
1112 unit cells with wave propagation analysis, could dramatically reduce computational  
1113 costs compared to conventional FEM by exploiting the periodic nature  
1114 of the structures. This method would enable efficient analysis of large-scale finite  
1115 plates while maintaining the accuracy demonstrated by the PWE/EPWE  
1116 framework for infinite structures. Furthermore, spectral element approaches and  
1117 machine learning-assisted optimization could complement the WFE methodolog-

<sub>1119</sub> ogy to accelerate the design process and unlock new possibilities for real-time  
<sub>1120</sub> optimization and adaptive metamaterial systems.

<sup>1121</sup> **Acknowledgments**



<sup>1122</sup> The authors gratefully acknowledge the financial support of this investigation  
<sup>1123</sup> by the Brazilian research funding agency CNPQ (Conselho Nacional de Desen-  
<sup>1124</sup> volvimento Científico e Tecnológico) and by UNICAMP (Universidade Estadual  
<sup>1125</sup> de Campinas).

## 1126 Appendix A. PWE Matrix Formulation for LRSC Plates with Five 1127 Lattice Configurations

This appendix details the matrix formulation required for PWE computational implementation across five lattice configurations. Starting from the governing equation presented in Section 2.1 (Eq. 1) with resonator forces at lattice positions  $\mathbf{R}$  and local positions  $\mathbf{r}_j$ , the displacement field follows Bloch's theorem with plane wave expansion as defined in Eq. (7):  $w(\mathbf{r}) = \sum_{\mathbf{G}} w(\mathbf{G}) e^{i(\mathbf{k} + \mathbf{G}) \cdot \mathbf{r}}$ , where  $\mathbf{G}$  are reciprocal lattice vectors,  $\mathbf{k}$  is the Bloch wave vector, and  $w(\mathbf{G})$  are plane wave amplitudes.

1135 The resonator forces follow Eq. (2) with complex dynamic stiffness:

$$p_j(\mathbf{r}_j + \mathbf{R}) = k_j^*[u_j(\mathbf{r}_j + \mathbf{R}) - w(\mathbf{r}_j + \mathbf{R})] \quad (\text{A.1})$$

where  $k_j^* = k_j(1 + i\eta_j)$  incorporates resonator damping effects as established in Section 2.1, with  $k_j = m_{r,j}\omega_{r,j}^2$  being the resonator stiffness,  $u_j$  the resonator displacement, and  $\eta_j$  the loss factor.

1139 Applying the plane wave expansion to the governing equation and utilizing or-  
 1140 thogonality of exponential functions yields the matrix eigenvalue problem:

$$[\mathbf{K} - \omega^2 \mathbf{M}] \{\mathbf{q}\} = \mathbf{0} \quad (\text{A.2})$$

where  $\mathbf{q} = [\mathbf{w}^T, \mathbf{u}^T]^T$  contains both plate wave amplitudes  $\mathbf{w} = [w(\mathbf{G}_1), w(\mathbf{G}_2), \dots, w(\mathbf{G}_{N_g})]^T$  and resonator displacements  $\mathbf{u} = [u_1, u_2, \dots, u_{N_g}]^T$ , with  $N_g = (2M+1)^2$  plane waves.

<sup>1144</sup> The augmented system matrices are assembled as:

$$\begin{bmatrix} \mathbf{K}_{pp} + \mathbf{K}_r & -\mathbf{P}\mathbf{K}_j \\ -\mathbf{K}_j\mathbf{P}^T & \mathbf{K}_j \end{bmatrix} \begin{bmatrix} \mathbf{w} \\ \mathbf{u} \end{bmatrix} = \omega^2 \begin{bmatrix} \mathbf{M}_{pp} & \mathbf{0} \\ \mathbf{0} & \mathbf{M}_{rr} \end{bmatrix} \begin{bmatrix} \mathbf{w} \\ \mathbf{u} \end{bmatrix} \quad (\text{A.3})$$

where  $\mathbf{K}_{pp}$  and  $\mathbf{M}_{pp}$  are the plate stiffness and mass matrices,  $\mathbf{K}_j = \text{diag}(k_1^*, k_2^*, \dots, k_{N_j}^*)$  contains resonator stiffnesses,  $\mathbf{M}_{rr} = \text{diag}(m_{r,1}, m_{r,2}, \dots, m_{r,N_j})$  contains resonator masses with  $m_{r,j} = \gamma\rho Sh/N_j$ , and  $\mathbf{P}$  is the coupling matrix with elements  $P_{i,j} = e^{i\mathbf{G}_i \cdot \mathbf{r}_j}$ .

<sup>1149</sup> The diagonal elements of the plate matrices are computed as:

$$\mathbf{K}_{pp}[i, i] = D \cdot S \cdot |\mathbf{k} + \mathbf{G}_i|^4 = D \cdot S \cdot [(k_x + G_{x,i})^2 + (k_y + G_{y,i})^2]^2 , \quad (\text{A.4})$$

$$\mathbf{M}_{pp}[i, i] = \rho h S . \quad (\text{A.5})$$

<sup>1150</sup> The coupling matrix has elements  $P_{i,j} = e^{i\mathbf{G}_i \cdot \mathbf{r}_j}$  and the resonator coupling  
<sup>1151</sup> stiffness matrix is  $\mathbf{K}_r = \sum_{j=1}^{N_j} (k_j^*/S) \mathbf{P}_j \mathbf{P}_j^T$ .

<sup>1152</sup> Reciprocal lattice vectors  $\mathbf{G}_{mn}$  for indices  $m, n \in [-M, M]$  are generated as:

$$\text{Square/Rectangular: } \mathbf{G}_{mn} = \frac{2\pi}{a_1} m \mathbf{e}_1 + \frac{2\pi}{a_2} n \mathbf{e}_2 \quad (\text{A.6})$$

$$\text{Triangular: } \mathbf{G}_{mn} = \frac{2\pi}{a} m \mathbf{e}_1 + \frac{2\pi}{a} \frac{m - 2n}{\sqrt{3}} \mathbf{e}_2 \quad (\text{A.7})$$

$$\text{Hexagonal: } \mathbf{G}_{mn} = \frac{2\pi}{a\sqrt{3}} (m - n) \mathbf{e}_1 + \frac{2\pi}{3a} (m + n) \mathbf{e}_2 \quad (\text{A.8})$$

$$\text{Kagomé: } \mathbf{G}_{mn} = \frac{\pi}{a} (m - n) \mathbf{e}_1 + \frac{\pi}{a} \frac{m + n}{\sqrt{3}} \mathbf{e}_2 \quad (\text{A.9})$$

<sup>1153</sup> Unit cell areas and resonator configurations: square/rectangular/triangular  $N_j =$   
<sup>1154</sup> 1 with  $\mathbf{r}_1 = \mathbf{0}$ , areas  $S = a^2, a_1 a_2, a^2 \sqrt{3}/2$  respectively; hexagonal  $N_j = 2$  with  
<sup>1155</sup>  $\mathbf{r}_{1,2} = (0, \pm a/2)$ , area  $S = 3a^2 \sqrt{3}/2$ ; kagomé  $N_j = 3$  with  $\mathbf{r}_1 = (-a/2, -a\sqrt{3}/6),$   
<sup>1156</sup>  $\mathbf{r}_2 = (a/2, -a\sqrt{3}/6), \mathbf{r}_3 = (0, a\sqrt{3}/3)$ , area  $S = 2a^2 \sqrt{3}$ .

<sup>1157</sup> Computational implementation: generate  $(2M + 1)^2$  reciprocal vectors using  
<sup>1158</sup> Eqs. (A.6)-(A.9), compute diagonal plate matrices via Eqs. (A.4)-(A.5), as-  
<sup>1159</sup> semble coupling matrix  $\mathbf{P}$  with phase factors  $e^{i\mathbf{G}_i \cdot \mathbf{r}_j}$ , form augmented system  
<sup>1160</sup> Eq. (A.3), solve eigenvalue problem, and extract physical frequencies.

<sup>1161</sup> Matrix assembly algorithm for each wave vector  $\mathbf{k}$ : (1) Initialize sparse matrices  
<sup>1162</sup>  $\mathbf{A}_n, \mathbf{A}_d \in \mathbb{C}^{(N_g + N_j) \times (N_g + N_j)}$  with  $N_g = (2M + 1)^2$ ; (2) Fill diagonal blocks:  
<sup>1163</sup>  $\mathbf{A}_n[1 : N_g, 1 : N_g] = \mathbf{M}_{pp}, \mathbf{A}_d[1 : N_g, 1 : N_g] = \mathbf{K}_{pp}$ ; (3) For each resonator  $j$ :  
<sup>1164</sup> compute phase vector  $\mathbf{p}_j$  with  $[\mathbf{p}_j]_i = e^{i\mathbf{G}_i \cdot \mathbf{r}_j}$ , add coupling  $\mathbf{A}_d[1 : N_g, 1 : N_g] \leftarrow$   
<sup>1165</sup>  $\mathbf{A}_d[1 : N_g, 1 : N_g] + (k_j^*/S) \mathbf{p}_j \mathbf{p}_j^H$ , set off-diagonal coupling  $\mathbf{A}_d[1 : N_g, N_g + j] =$   
<sup>1166</sup>  $-k_j^* \mathbf{p}_j$ ,  $\mathbf{A}_d[N_g + j, 1 : N_g] = -k_j^* \mathbf{p}_j^H$ , and diagonal terms  $\mathbf{A}_n[N_g + j, N_g + j] =$   
<sup>1167</sup>  $m_{r,j}$ ,  $\mathbf{A}_d[N_g + j, N_g + j] = k_j^*$ .

<sub>1168</sub> Eigenvalue solution:  $\mathbf{A}_d\phi_i = \lambda_i \mathbf{A}_n\phi_i$  yields frequencies  $f_i = \text{Re}(\sqrt{|\lambda_i|})/(2\pi)$ .

<sub>1169</sub> Computational parameters: typical  $M = 3 - 5$  plane waves per direction provide

<sub>1170</sub> convergence for  $|\mathbf{k} + \mathbf{G}_{\max}|a < \pi$ . For bare plates:  $\omega^2 = (D/\rho h)|\mathbf{k} + \mathbf{G}_i|^4$  directly.

Table A.19: Summary of lattice-specific parameters for PWE implementation

Lattice	Unit Cell Area	Resonators/Cell	Key FIBZ Points
Square	$a^2$	1	$\Gamma(0, 0), X(\pi/a, 0), M(\pi/a, \pi/a)$
Rectangular	$a_x a_y$	1	$\Gamma(0, 0), X(\pi/a_x, 0), M(\pi/a_x, \pi/a_y)$
Triangular	$a^2\sqrt{3}/2$	1	$\Gamma(0, 0), X(4\pi/3a, 0), M(\pi/a, \pi/(a\sqrt{3}))$
Honeycomb	$3a^2\sqrt{3}/2$	2	$\Gamma(0, 0), X(4\pi/(3a\sqrt{3}), 0), M(\pi/(a\sqrt{3}), \pi/(3a))$
Kagomé	$2a^2\sqrt{3}$	3	$\Gamma(0, 0), X(2\pi/(3a), 0), M(\pi/(2a), \pi/(2a\sqrt{3}))$



## 1171 Appendix B. EPWE Matrix Formulation for Complex Wave Vector 1172 Analysis

This appendix details the Extended PWE (EPWE) matrix formulation for computing complex wave vectors  $k(\omega)$  at prescribed frequencies. The method solves the inverse eigenvalue problem, enabling direct analysis of wave attenuation and evanescent modes within bandgaps.

Starting from the same governing equation (Eq. 1), EPWE maintains the Bloch expansion but reformulates the problem as a polynomial eigenvalue equation in  $k$ . The displacement field retains the form  $w(\mathbf{r}) = \sum_{\mathbf{G}} w(\mathbf{G}) e^{i(\mathbf{k} + \mathbf{G}) \cdot \mathbf{r}}$  where  $\mathbf{k} = k_r + ik_i \in \mathbb{C}$  allows exponentially decaying modes.

For wave propagation direction  $\mathbf{k} = k(\cos \phi, \sin \phi)$ , the governing equation yields a quartic polynomial eigenvalue problem:

$$[\mathbf{A}_3 k^3 + \mathbf{A}_2 k^2 + \mathbf{A}_1 k + \mathbf{A}_0] \psi = 0 \quad (\text{B.1})$$

where coefficient matrices depend on lattice geometry, frequency, and resonator coupling.

1185 The coefficient matrices for each reciprocal vector  $\mathbf{G}_i$  are constructed as:

$$\mathbf{A}_0[i, i] = \frac{DS}{a^4} |\mathbf{G}_i|^4 - \rho h S \omega^2 + D_j(\omega) \quad (\text{B.2})$$

$$\mathbf{A}_1[i, i] = \frac{4DS}{a^4} |\mathbf{G}_i|^2 (\mathbf{G}_i \cdot \hat{\mathbf{k}}) \quad (\text{B.3})$$

$$\mathbf{A}_2[i, i] = \frac{2DS}{a^4} [|\mathbf{G}_i|^2 + 2(\mathbf{G}_i \cdot \hat{\mathbf{k}})^2] \quad (\text{B.4})$$

$$\mathbf{A}_3[i, i] = \frac{4DS}{a^4} (\mathbf{G}_i \cdot \hat{\mathbf{k}}) \quad (\text{B.5})$$

where  $\hat{\mathbf{k}} = (\cos \phi, \sin \phi)$  is the propagation direction and  $D_j(\omega) = k_j^* - (k_j^*)^2/(k_j^* - \omega^2 m_{r,j})$  is the frequency-dependent dynamic stiffness from Eq. (12).

1188 Companion matrix linearization transforms Eq. (B.1) into the generalized eigen-

1189 value problem:



$$\begin{bmatrix} -\mathbf{A}_3 & -\mathbf{A}_2 & -\mathbf{A}_1 & -\mathbf{A}_0 \\ \mathbf{I} & \mathbf{0} & \mathbf{0} & \mathbf{0} \\ \mathbf{0} & \mathbf{I} & \mathbf{0} & \mathbf{0} \\ \mathbf{0} & \mathbf{0} & \mathbf{I} & \mathbf{0} \end{bmatrix} \begin{bmatrix} \psi_1 \\ \psi_2 \\ \psi_3 \\ \psi_4 \end{bmatrix} = k \begin{bmatrix} \mathbf{I} & \mathbf{0} & \mathbf{0} & \mathbf{0} \\ \mathbf{0} & \mathbf{0} & \mathbf{0} & \mathbf{0} \\ \mathbf{0} & \mathbf{0} & \mathbf{0} & \mathbf{0} \\ \mathbf{0} & \mathbf{0} & \mathbf{0} & \mathbf{0} \end{bmatrix} \begin{bmatrix} \psi_1 \\ \psi_2 \\ \psi_3 \\ \psi_4 \end{bmatrix} \quad (\text{B.6})$$

1190 Computational algorithm: (1) For each frequency  $\omega$ , compute coefficient matri-  
1191 ces using Eqs. (B.2)-(B.5) with the same reciprocal vectors from Appendix A; (2)  
1192 Assemble companion matrix Eq. (B.6) of size  $4N_g \times 4N_g$  with  $N_g = (2M + 1)^2$ ;  
1193 (3) Solve eigenvalue problem to extract  $4N_g$  complex wave vectors  $k_i$ ; (4) Apply  
1194 eigenvector tracking for mode continuity across frequency; (5) Normalize results:  
1195  $k_{\text{norm}} = k \cdot a / (2\pi)$ .

1196 Physical interpretation:  $\text{Re}(k)$  represents propagating modes while  $\text{Im}(k) > 0$   
1197 quantifies evanescent decay. The attenuation constant  $\mu = \text{Im}(k) \cdot a$  [Np/cell]  
1198 directly measures wave attenuation within bandgaps. Typical computational  
1199 parameters:  $M = 2 - 3$  plane waves provide convergence for EPWE due to  
1200 polynomial scaling, with frequency resolution  $\Delta f = 1 - 10$  [Hz] depending on  
1201 application requirements.

1202    **Appendix C. Extension to Structural Materials - Multi-Scale Anal-**  
1203                **ysis**

1204    While this study focuses on polymeric materials for practical validation through  
1205    rapid prototyping, the PWE/EPWE methodology developed is applicable to a  
1206    broad range of structural materials. This appendix demonstrates the universal-  
1207    ity of our framework by extending the analysis to metallic and composite ma-  
1208    terials (aluminum and carbon/epoxy), revealing that the geometric advantages  
1209    identified for different lattice configurations represent material-independent de-  
1210    sign principles. For brevity, only the PWE method is implemented in this  
1211    multi-material analysis, as the main study has already validated the excellent  
1212    agreement between PWE and EPWE approaches.

1213    *Appendix C.1. Material Properties and Scaling Analysis*

1214    The choice of Vero White Plus polymeric material was strategically motivated  
1215    by rapid prototyping capabilities through 3D printing, enabling precise fabrica-  
1216    tion of complex lattice geometries with controlled tolerances for experimental  
1217    validation. However, structural engineering applications often require materials  
1218    with significantly higher bending stiffness, necessitating analysis across multi-  
1219    ple material scales. The aluminum material properties ( $E = 70 \text{ GPa}$ ,  $\nu = 0.3$ )  
1220    were obtained from the work of Xiao et al. [46], while the carbon fiber/epoxy  
1221    composite properties ( $E = 135 \text{ GPa}$ ,  $\rho = 1580 \text{ kg/m}^3$ ,  $\nu = 0.30$ ) were obtained  
1222    from the Composite Materials Handbook-17 [64].

1223    Table C.20 presents the comparative material properties used in this multi-scale  
1224    analysis:

Table C.20: Comparative material properties for multi-scale analysis

Material	$E \text{ [GPa]}$	$\rho \text{ [kg/m}^3\text{]}$	$\nu$	$D \text{ [N}\cdot\text{m]}$	$D/D_{\text{polymer}}$
Vero White Plus	0.86	600	0.36	$6.59 \times 10^{-1}$	1.0
Aluminum 6061	70	2700	0.30	$5.13 \times 10^1$	77.9
Carbon/Epoxy UD	135	1580	0.30	$9.89 \times 10^1$	150.1

1225 The bending stiffness  $D = Eh^3/12(1 - \nu^2)$  scales dramatically across materials,  
 1226 with carbon/epoxy composite exhibiting  $150\times$  higher rigidity than the polymer.  
 1227 This scaling directly affects the operational frequency ranges while maintaining  
 1228 the validity of Kirchhoff-Love thin plate assumptions ( $h/a = 0.02 \ll 0.1$ ).

1229 *Appendix C.2. Frequency Scaling and Operational Ranges*



1230 The characteristic frequency scaling follows the relationship  $f_{B_1} = (1/2\pi)(\pi/a \cos \phi)^2 \sqrt{D/\rho h}$ ,  
 1231 resulting in proportional frequency shifts across materials while preserving ge-  
 1232 ometric relationships. It should be noted that these Bragg frequencies are cal-  
 1233 culated specifically for square lattice configurations, following the methodology  
 1234 established by Xiao et al. [46], where  $\phi = 0$  corresponds to the  $\Gamma$ -X direction  
 1235 in the first Brillouin zone. Table C.21 summarizes the operational frequency  
 1236 ranges for each material:

Table C.21: Frequency scaling and operational ranges across materials

Material	h [mm]	a [mm]	h/a	Target Range [Hz]	$f_B$ [Hz]
Vero White Plus	2.0	100	0.02	10–200	116
Aluminum 6061	2.0	100	0.02	200–600	484
Carbon/Epoxy UD	2.0	100	0.02	400–1000	879

1237 *Appendix C.3. PWE Analysis Results for Alternative Materials*

1238 Using identical PWE computational parameters ( $M = 2$ , convergence tolerance  
 1239  $10^{-6}$ ), the band gap analysis was extended to aluminum and carbon/epoxy  
 1240 configurations. The methodology maintains numerical stability across the  $150\times$   
 1241 stiffness variation, confirming the robustness of the semi-analytical approach.

1242 *Appendix C.3.1. Aluminum Analysis (200-600 Hz Range)*

1243 Table C.22 presents the complete band gap width analysis for aluminum lattices  
 1244 across selected resonator frequencies, including the Bragg frequency (484 Hz):

1245

Table C.22: Full band gap width evolution for Aluminum 6061 lattices with FBGW 1 and FBGW 2 for multi-resonator configurations<sup>1</sup>

$f_j$ (Hz)	Square FBGW	Rectangular FBGW	Triangular FBGW	Honeycomb FBGW 1	Honeycomb FBGW 2	Kagomé FBGW 1	Kagomé FBGW 2
150	36.1	33.7	36.4	35.8	–	<b>26.3</b>	–
175	43.2	39.2	43.8	42.5	–	16.9	10.7
200	50.4	44.9	51.2	49.2	20.8	13.3	18.8
225	57.9	50.7	59.0	55.7	45.0	12.3	20.0
250	66.4	56.0	68.1	<b>57.7</b>	66.5	12.5	19.9
275	75.8	61.1	78.3	43.3	66.7	13.4	19.5
300	84.2	66.9	87.4	26.8	68.0	14.7	19.6
325	91.4	69.0	96.0	11.5	70.3	16.3	20.5
350	97.3	58.6	103.7	–	73.5	18.4	22.1
375	113.4	81.4	120.9	–	77.4	11.7	24.2
400	107.0	30.4	127.5	–	81.9	3.8	26.9
425	<b>131.1</b>	74.7	145.8	–	87.0	–	26.6
450	111.0	5.4	161.7	–	92.7	–	23.1
475	111.0	30.7	172.1	–	98.9	–	20.0
484 <sup>2</sup>	107.0	22.9	176.9	–	<b>101.2</b>	–	19.1
500	89.9	–	198.4	–	105.3	–	17.8
525	89.9	–	198.4	–	111.1	–	16.5
575	71.7	–	<b>222.0</b>	–	113.7	–	16.4
625	56.2	–	219.4	–	93.6	–	17.5
725	31.5	–	196.1	–	62.9	–	17.4

<sup>1246</sup> Appendix C.3.2. Carbon/Epoxy Analysis (250-1400 Hz Range)

<sup>1247</sup> Table C.23 presents the complete band gap width analysis for carbon/epoxy

<sup>1248</sup> lattices across selected resonator frequencies, including the Bragg frequency (879

<sup>1249</sup> Hz):

Table C.23: Full band gap width evolution for Carbon/Epoxy UD lattices with FBGW 1 and FBGW 2 for multi-resonator configurations<sup>1</sup>

$f_j$ (Hz)	Square FBGW	Rectangular FBGW	Triangular FBGW	Honeycomb FBGW 1	Honeycomb FBGW 2	Kagomé FBGW 1	Kagomé FBGW 2
300	73.1	67.4	73.9	72.3	–	<b>35.9</b>	10.4
350	87.1	78.5	88.3	85.9	25.6	25.4	32.4
400	102.9	89.8	104.9	99.0	73.3	22.5	36.2
450	119.3	103.2	124.2	<b>105.2</b>	120.7	22.7	36.1
500	136.6	111.9	140.9	78.1	121.1	24.3	35.4
550	154.7	118.0	158.3	45.2	123.9	26.9	35.7
600	174.0	133.0	182.3	14.9	128.8	30.4	37.7
650	191.4	136.7	201.5	–	135.5	30.3	41.2
700	207.8	126.3	220.3	–	143.8	15.3	45.9
750	<b>231.8</b>	<b>151.7</b>	253.7	–	153.5	–	51.5
800	231.5	110.2	279.5	–	164.4	–	44.2
850	207.3	66.4	305.9	–	176.4	–	37.7
879 <sup>2</sup>	194.1	41.2	321.2	–	<b>183.8</b>	–	34.7
900	164.4	–	334.0	–	189.2	–	32.9
950	164.4	–	358.6	–	201.1	–	30.1
1000	134.2	–	381.8	–	210.8	–	29.3
1050	108.4	–	402.0	–	203.8	–	29.9
1100	112.2	–	<b>408.1</b>	–	183.1	–	31.0
1150	88.7	–	398.4	–	164.3	–	32.0
1200	84.2	–	389.8	–	147.4	–	32.5

1250

1251 *Appendix C.4. Universal Performance Hierarchy*

1252 The comparative analysis across three materials reveals a remarkable consistency  
 1253 in lattice performance hierarchy. Tables C.22 and C.23 provide complete  
 1254 transparency of all simulation results, including both FBGW 1 and FBGW  
 1255 2 for multi-resonator configurations (honeycomb and kagomé). The universal

1256 ranking based on maximum FBGW achieved is: Triangular > Square > Honey-  
 1257 comb FBGW 2 > Rectangular > Honeycomb FBGW 1 > Kagomé FBGW 2 >  
 1258 Kagomé FBGW 1.

1259 The detailed tabulated data demonstrates material-independent geometric ad-  
 1260 vantages, with triangular lattices consistently achieving 40-42% relative band-  
 1261 widths across all materials. Notably, honeycomb FBGW 2 emerges as a signifi-  
 1262 cant contributor (101.2 Hz for aluminum, 183.8 Hz for carbon/epoxy), demon-  
 1263 strating the dual-bandgap capability of multi-resonator systems. The frequency  
 1264 scaling preserves this hierarchy while shifting operational ranges proportionally  
 1265 to material stiffness:

Table C.24: Universal performance hierarchy: maximum FBGW across materials (including FBGW 2 for multi-resonator systems)

Rank	Configuration	Vero White Plus	Aluminum 6061	Carbon/Epoxy UD
1st	Triangular	55.4 Hz	222.0 Hz	408.1 Hz
2nd	Square	32.1 Hz	131.1 Hz	231.8 Hz
3rd	Honeycomb FBGW 2	28.7 Hz	101.2 Hz	183.8 Hz
4th	Rectangular	20.5 Hz	84.2 Hz	151.7 Hz
5th	Honeycomb FBGW 1	14.3 Hz	57.7 Hz	105.2 Hz
6th	Kagomé FBGW 2	6.9 Hz	26.9 Hz	51.5 Hz
7th	Kagomé FBGW 1	6.5 Hz	26.3 Hz	35.9 Hz

Red values: FBGW 2 data newly incorporated from complete analysis

1266 Appendix C.5. Design Guidelines for Material Selection

1267 Based on the multi-scale analysis, the following design guidelines emerge for  
 1268 practical applications:

1269 **Low-frequency applications (< 200 Hz):** Polymeric materials with trian-  
 1270 gular lattices provide optimal performance while enabling rapid prototyping and  
 1271 experimental validation.

1272 **Mid-frequency applications (200-600 Hz):** Aluminum lattices maintain  
 1273 the geometric advantages with triangular configurations achieving 72.5% supe-  
 1274 rior performance over square lattices.

1275 **High-frequency applications (400-1000 Hz):** Carbon/epoxy composite lat-  
1276 tices preserve the universal hierarchy, with triangular geometries achieving 76%  
1277 superior performance over square configurations (408.1 Hz vs 231.8 Hz maxi-  
1278 mum FBGW).

1279 *Appendix C.6. Conclusions of Multi-Material Extension*

1280 This comprehensive multi-material analysis demonstrates several key findings:

1281 1. **Geometric principles are material-independent:** The triangular lat-  
1282 tice superiority is maintained across materials spanning  $150\times$  stiffness variation  
1283 (polymer to carbon/epoxy composite).

1284 2. **Frequency scaling is predictable:** Performance ratios scale proportionally  
1285 with  $\sqrt{D/\rho h}$ , enabling systematic material selection for target frequencies.

1286 3. **Methodology robustness:** PWE computational stability and accuracy are  
1287 preserved across the entire material range studied.

1288 4. **Universal design framework:** The established performance hierarchy  
1289 provides engineering guidelines applicable to the full spectrum of structural  
1290 materials.

1291 The extension validates that our polymer-based findings represent universal de-  
1292 sign principles, while the initial material choice was strategically optimal for  
1293 experimental validation and rapid prototyping capabilities.

## 1294 Appendix D. Framework for Lattice Selection in Engineering Appli-

1295 cations



1296 The individual analyses presented in Section 4.1 reveal distinct performance  
1297 characteristics that enable systematic lattice selection based on application re-  
1298 quirements. This appendix synthesizes the comparative findings into practical  
1299 engineering guidelines through performance metrics, design trade-offs, and a  
1300 quantitative decision framework.

### 1301 *Appendix D.1. Performance-Based Design Categories*

1302 The five lattice geometries exhibit distinct optimization characteristics that de-  
1303 fine three fundamental design categories:

1304 **Peak Performance Category (Kagomé):** Maximizes absolute attenuation  
1305 through multi-resonator coupling, achieving -292.65 [dB] with highest mate-  
1306 rial utilization ( $m_{ratio} = 1.00$ ). Optimal for applications requiring maximum  
1307 vibration suppression at specific target frequencies with material efficiency as  
1308 secondary consideration.

1309 **Balanced Performance Category (Honeycomb, Square):** Provides moderate-  
1310 to-high attenuation with predictable frequency response. Honeycomb (-220.33  
1311 [dB]) offers dual-mode capability for frequency-selective applications, while square  
1312 (-173.09 [dB]) delivers consistent single-mode performance for standard vibra-  
1313 tion control requirements.

1314 **Broadband Category (Triangular):** Optimizes bandwidth-to-performance  
1315 ratio with exceptional area efficiency. Despite minimal material usage ( $m_{ratio} =$   
1316 0.25), achieves near-peak performance (-174.19 [dB]) with superior FBGW char-  
1317 acteristics ( $\approx 150$  [Hz]), ideal for applications requiring robust performance  
1318 across wide frequency ranges.

1319 **Specialized Applications (Rectangular):** Limited performance (-129.93  
1320 [dB]) compensated by geometric anisotropy enabling directional wave control

<sup>1321</sup> and space-constrained implementations where unit cell aspect ratio is predeter-  
<sup>1322</sup> mined by structural constraints.

<sup>1323</sup> *Appendix D.2. Quantitative Selection Framework*

<sup>1324</sup> Based on the comparative analysis, Table D.25 presents a quantitative decision  
<sup>1325</sup> matrix correlating application requirements with optimal lattice configurations:

Table D.25: Quantitative framework for lattice selection in engineering applications. Performance Score (\*): Weighted average (peak attenuation 40%, bandwidth 30%, material efficiency 20%, manufacturing feasibility 10%). Abbreviations: Att. = Attenuation; Mat. Eff. = Material Efficiency; Perf. = Performance; Manuf. = Manufacturing; App. = Applications; Opt. = Optimal; Freq. = Frequency.

Criterion	Kagomé	Honeycomb	Triangular	Square	Rectangular
<i>Performance Metrics</i>					
Peak Att. [dB]	-292.65	-220.33	-174.19	-173.09	-129.93
Mat. Eff. Rank	1st	2nd	5th	3rd	4th
Bandwidth Perf.	Narrow	Dual-mode	Excellent	Moderate	Limited
Freq. Selectivity	High	Medium	Low	Medium	Medium
<i>Application Characteristics</i>					
Manuf. Complex.	High	Medium	Low	Low	Low
Target App.	Max supp.	Dual flex.	Broadband	Standard	Direction.
Opt. Freq. [Hz]	10-30	10-50	30-150	30-100	30-80
<i>Overall Assessment</i>					
Perf. Score*	10.0	8.5	9.2	7.8	5.9

<sup>1326</sup> *Appendix D.3. Application-Specific Design Guidelines*

<sup>1327</sup> The framework establishes four primary application scenarios with correspond-  
<sup>1328</sup> ing optimal lattice selection:

<sup>1329</sup> **Scenario 1 - Critical Vibration Isolation:** Applications requiring maxi-  
<sup>1330</sup> mum attenuation at specific frequencies (precision instrumentation, sensitive  
<sup>1331</sup> equipment mounting). *Recommended:* Kagomé lattice for peak performance,  
<sup>1332</sup> honeycomb as secondary option with manufacturing advantages.

1333 **Scenario 2 - Broadband Noise Control:** Systems operating across wide  
1334 frequency ranges (automotive panels, building facades, aerospace structures).  
1335 *Recommended:* Triangular lattice for optimal bandwidth-performance balance,  
1336 square lattice for standard requirements.

1337 **Scenario 3 - Multi-Frequency Applications:** Environments with distinct  
1338 frequency components requiring selective attenuation (industrial machinery, HVAC  
1339 systems). *Recommended:* Honeycomb lattice for dual-mode capability, kagomé  
1340 for primary frequency with secondary suppression.

1341 **Scenario 4 - Constrained Design Space:** Applications with predetermined  
1342 geometric constraints or directional requirements (architectural integration, retrofit  
1343 applications). *Recommended:* Rectangular lattice for anisotropic control, square  
1344 lattice for space-efficient implementation.

1345 This framework transforms lattice selection from empirical approaches to system-  
1346 atic engineering decision-making, enabling optimal configuration choice based  
1347 on quantifiable performance metrics and application-specific requirements. The  
1348 decision table provides engineers with concrete guidelines derived from the com-  
1349 prehensive comparative analysis presented in Sections 3 and 4.1, establishing a  
1350 bridge between theoretical insights and practical metamaterial design.

1351      **References**

- 1352      [1] M. Mir, F. Nasirzadeh, S. Lee, D. Cabrera, A. Mills, Construction noise  
1353      management: A systematic review and directions for future research,  
1354      Applied Acoustics 197 (2022) 108936. doi:10.1016/j.apacoust.2022.  
1355      108936.
- 1356      [2] R. Kandasamy, F. Cui, N. Townsend, C. C. Foo, J. Guo, A. Shenoi,  
1357      Y. Xiong, A review of vibration control methods for marine offshore struc-  
1358      tures, Ocean Engineering 127 (2016) 279–297. doi:10.1016/j.oceaneng.  
1359      2016.10.001.
- 1360      [3] M. D. Rao, Recent applications of viscoelastic damping for noise control  
1361      in automobiles and commercial airplanes, Journal of Sound and Vibration  
1362      262 (3) (2003) 457–474. doi:10.1016/S0022-460X(03)00106-8.
- 1363      [4] J. Masri, M. Amer, S. Salman, M. Ismail, M. Elsisi, A survey of mod-  
1364      ern vehicle noise, vibration, and harshness: A state-of-the-art, Ain Shams  
1365      Engineering Journal 15 (10) (2024) 102957. doi:10.1016/j.asej.2024.  
1366      102957.
- 1367      [5] K. H. Matlack, A. Bauhofer, S. Krödel, A. Palermo, C. Daraio, Compos-  
1368      ite 3d-printed metastructures for low-frequency and broadband vibration  
1369      absorption, Proceedings of the National Academy of Sciences 113 (2016)  
1370      8386–8390. doi:10.1073/pnas.1600171113.
- 1371      [6] X. An, C. Lai, H. Fan, C. Zhang, 3d acoustic metamaterial-based me-  
1372      chanical metalattice structures for low-frequency and broadband vibration  
1373      attenuation, International Journal of Solids and Structures 191-192 (2020)  
1374      293–306. doi:10.1016/j.ijsolstr.2020.01.020.
- 1375      [7] G. Comandini, C. Khodr, V. P. Ting, M. Azarpeyvand, F. Scarpa, Archi-  
1376      tected acoustic metamaterials: An integrated design perspective, Applied  
1377      Physics Reviews 12 (1) (2024) 011340. doi:10.1063/5.0230888.

- 1378 [8] S. Lin, Y. Zhang, Y. Liang, Y. Liu, C. Liu, Z. Yang, Bandgap characteristics  
1379 and wave attenuation of metamaterials based on negative-stiffness dynamic  
1380 vibration absorbers, *Journal of Sound and Vibration* 502 (2021) 116088.  
1381 [doi:10.1016/j.jsv.2021.116088](https://doi.org/10.1016/j.jsv.2021.116088).
- 1382 [9] L. D'Alessandro, R. Ardito, F. Braghin, A. Corigliano, Low frequency 3d  
1383 ultra-wide vibration attenuation via elastic metamaterial, *Scientific Reports* 9 (2019) 8039. [doi:10.1038/s41598-019-44507-6](https://doi.org/10.1038/s41598-019-44507-6).
- 1385 [10] M. I. Hussein, M. J. Leamy, M. Ruzzene, Dynamics of phononic materials  
1386 and structures: Historical origins, recent progress, and future outlook, *Applied Mechanics Reviews* 66 (4) (2014) 040802. [doi:10.1115/1.4026911](https://doi.org/10.1115/1.4026911).
- 1388 [11] L. E. Kinsler, A. R. Frey, A. B. Coppens, J. V. Sanders, *Fundamentals of  
1389 Acoustics*, 4th Edition, Wiley, 2000.
- 1390 [12] S. Kumar, H. P. Lee, Recent advances in acoustic metamaterials for simul-  
1391 taneous sound attenuation and air ventilation performances, *Crystals* 10 (8)  
1392 (2020) 686. [doi:10.3390/cryst10080686](https://doi.org/10.3390/cryst10080686).
- 1393 [13] M. Weiner, X. Ni, M. Li, A. Alù, A. B. Khanikaev, Demonstration of a  
1394 third-order hierarchy of topological states in a three-dimensional acoustic  
1395 metamaterial, *Science Advances* 6 (13) (2020) eaay4166. [doi:10.1126/sciadv.aay4166](https://doi.org/10.1126/sciadv.aay4166).
- 1397 [14] L. Lu, T. Yamamoto, M. Otomori, T. Yamada, K. Izui, S. Nishiwaki, Topol-  
1398 ogy optimization of an acoustic metamaterial with negative bulk modulus  
1399 using local resonance, *Finite Elements in Analysis and Design* 72 (2013)  
1400 1–12. [doi:10.1016/j.finel.2013.04.005](https://doi.org/10.1016/j.finel.2013.04.005).
- 1401 [15] D. Li, L. Zigoneanu, B.-I. Popa, S. A. Cummer, Design of an acoustic  
1402 metamaterial lens using genetic algorithms, *The Journal of the Acoustical  
1403 Society of America* 132 (4) (2012) 2823–2833. [doi:10.1121/1.4744942](https://doi.org/10.1121/1.4744942).

- 1404 [16] E. Yablonovitch, Inhibited spontaneous emission in solid-state physics and  
1405       electronics, *Physical Review Letters* 58 (20) (1987) 2059–2062. doi:10.  
1406       1103/PhysRevLett.58.2059.
- 1407 [17] S. John, Strong localization of photons in certain disordered dielectric  
1408       superlattices, *Physical Review Letters* 58 (23) (1987) 2486–2489. doi:  
1409       10.1103/PhysRevLett.58.2486.
- 1410 [18] R. D. Meade, K. D. Brommer, A. M. Rappe, J. D. Joannopoulos, Existence  
1411       of a photonic band gap in two dimensions, *Applied Physics Letters* 61 (4)  
1412       (1992) 495–497. doi:10.1063/1.107868.
- 1413 [19] P. R. Villeneuve, M. Piché, Photonic band gaps in two-dimensional square  
1414       and hexagonal lattices, *Physical Review B* 46 (8) (1992) 4969–4973. doi:  
1415       10.1103/PhysRevB.46.4969.
- 1416 [20] J. D. Joannopoulos, P. R. Villeneuve, S. Fan, Photonic crystals: Putting  
1417       a new twist on light, *Nature* 386 (6621) (1997) 143–149. doi:10.1038/  
1418       386143a0.
- 1419 [21] M. M. Sigalas, E. N. Economou, Elastic and acoustic wave band structure,  
1420       *Journal of Sound and Vibration* 158 (2) (1992) 377–382. doi:10.1016/  
1421       0022-460X(92)90059-7.
- 1422 [22] M. S. Kushwaha, P. Halevi, G. Martinez, L. Dobrzynski, B. Djafari-  
1423       Rouhani, Theory of acoustic band structure of periodic elastic composites,  
1424       *Physical Review B* 49 (4) (1994) 2313–2322. doi:10.1103/PhysRevB.49.  
1425       2313.
- 1426 [23] J. O. Vasseur, B. Djafari-Rouhani, L. Dobrzynski, M. S. Kushwaha,  
1427       P. Halevi, Band-gap engineering in periodic elastic composites, *Applied  
1428       Physics Letters* 64 (9) (1994) 1085–1087. doi:10.1063/1.110940.
- 1429 [24] J.-O. Vasseur, P. A. Deymier, B. Djafari-Rouhani, Y. Pennec, A.-C. Hladky-  
1430       Hennion, Absolute forbidden bands and waveguiding in two-dimensional

- phononic crystal plates, Physical Review B 77 (8) (2008) 085415. doi:  
10.1103/PhysRevB.77.085415.
- [25] Y. Pennec, J.-O. Vasseur, B. Djafari-Rouhani, Two-dimensional phononic crystals: Examples and applications, Surface Science Reports 65 (8) (2010) 229–291. doi:10.1016/j.surfrep.2010.08.002.
- [26] G. Floquet, Sur les équations différentielles linéaires à coefficients périodiques, Annales scientifiques de l'École normale supérieure 12 (1883) 47–88.
- [27] F. Bloch, Über die quantenmechanik der elektroden, Zeitschrift für Physik 52 (1928) 555–600. doi:10.1007/BF01339455.
- [28] L. Brillouin, Wave Propagation in Periodic Structures, McGraw-Hill, 1946.
- [29] Y. El Hassouani, C. Li, Y. Pennec, E. H. El Boudouti, H. Larabi, A. Akjouj, O. Bou Matar, V. Laude, N. Papanikolaou, Dual phononic and photonic band gaps in a periodic array of pillars deposited on a thin plate, Physical Review B 82 (15) (2010) 155405. doi:10.1103/PhysRevB.82.155405.
- [30] V. Laude, Phononic Crystals: Artificial Crystals for Sonic, Acoustic, and Elastic Waves, De Gruyter, 2015.
- [31] M. I. Hussein, Reduced bloch mode expansion for periodic media band structure calculations, Proceedings of the Royal Society A 462 (2073) (2006) 3385–3408. doi:10.1098/rspa.2008.0471.
- [32] S. Zhang, J. H. Wu, Z. Hu, Low-frequency locally resonant band-gaps in phononic crystal plates with periodic spiral resonators, Journal of Applied Physics 113 (16) (2013) 163511. doi:10.1063/1.4803075.
- [33] Z. Liu, X. Zhang, Y. Mao, Y. Y. Zhu, Z. Yang, C. T. Chan, P. Sheng, Locally resonant sonic materials, Science 289 (5485) (2000) 1734–1736. doi:10.1126/science.289.5485.1734.

- 1457 [34] G. Wang, X. Wen, J. Wen, L. Shao, Y. Liu, Two-dimensional locally res-  
1458 onant phononic crystals with binary structures, Physical Review Letters  
1459 93 (15) (2004) 154302. doi:[10.1103/PhysRevLett.93.154302](https://doi.org/10.1103/PhysRevLett.93.154302).
- 1460 [35] G. Wang, X. Wen, J. Wen, Y. Liu, Quasi-one-dimensional periodic struc-  
1461 ture with locally resonant band gap, Journal of Applied Mechanics 73 (1)  
1462 (2005) 167–170. doi:[10.1115/1.2061947](https://doi.org/10.1115/1.2061947).
- 1463 [36] J.-C. Hsu, T.-T. Wu, Lamb waves in binary locally resonant phononic  
1464 plates with two-dimensional lattices, Applied Physics Letters 90 (20) (2007)  
1465 201904. doi:[10.1063/1.2739369](https://doi.org/10.1063/1.2739369).
- 1466 [37] M. Oudich, M. B. Assouar, Z. Hou, Propagation of acoustic waves and  
1467 waveguiding in a two-dimensional locally resonant phononic crystal plate,  
1468 Applied Physics Letters 97 (19) (2010) 193503. doi:[10.1063/1.3513218](https://doi.org/10.1063/1.3513218).
- 1469 [38] M. Oudich, M. Senesi, M. B. Assouar, M. Ruzenne, J.-H. Sun, B. Vincent,  
1470 Z. Hou, T.-T. Wu, Experimental evidence of locally resonant sonic band  
1471 gap in two-dimensional phononic stubbed plates, Physical Review B 84 (16)  
1472 (2011) 165136. doi:[10.1103/PhysRevB.84.165136](https://doi.org/10.1103/PhysRevB.84.165136).
- 1473 [39] G. Kirchhoff, On the theory of elastic plates, Annalen der Physik 147 (1850)  
1474 423–435.
- 1475 [40] A. E. H. Love, The small free vibrations and deformations of a thin elastic  
1476 shell, Philosophical Transactions of the Royal Society A 179 (1888) 491–  
1477 549.
- 1478 [41] R. D. Mindlin, Influence of rotatory inertia and shear on flexural motions  
1479 of isotropic elastic plates, Journal of Applied Mechanics 18 (1951) 31–38.  
1480 doi:[10.1115/1.4010217](https://doi.org/10.1115/1.4010217).
- 1481 [42] E. Reissner, The effect of transverse shear deformation on the bending  
1482 of elastic plates, Journal of Applied Mechanics 12 (1945) 69–77. doi:[10.1115/1.4009435](https://doi.org/10.1115/1.4009435).

- 1484 [43] A. S. Phani, J. Woodhouse, N. A. Fleck, Wave propagation in two-  
1485 dimensional periodic plates, *Journal of the Acoustical Society of America*  
1486 119 (2006) 1995–2005. doi:[10.1121/1.2179748](https://doi.org/10.1121/1.2179748).
- 1487 [44] S.-T. Hsue, D.-M. Fang, S.-F. Tzeng, Extended plane-wave-expansion  
1488 method for phononic crystals, *Physical Review B* 72 (2005) 085123. doi:  
1489 [10.1103/PhysRevB.72.195118](https://doi.org/10.1103/PhysRevB.72.195118).
- 1490 [45] V. Laude, Y. Achaoui, S. Benchabane, A. Khelif, Evanescent bloch waves  
1491 and the complex band structure of phononic crystals, *Physical Review B*  
1492 80 (9) (2009) 092301. doi:[10.1103/PhysRevB.80.092301](https://doi.org/10.1103/PhysRevB.80.092301).
- 1493 [46] Y. Xiao, J. Wen, X. Wen, Flexural wave band gaps in locally resonant thin  
1494 plates with periodically attached spring-mass resonators, *Journal of Physics*  
1495 D: Applied Physics 45 (19) (2012) 195401. doi:[10.1088/0022-3727/45/19/195401](https://doi.org/10.1088/0022-3727/45/19/195401).
- 1497 [47] Y. Xiao, J. Wen, L. Huang, X. Wen, Analysis and experimental realization  
1498 of locally resonant phononic plates carrying a periodic array of beam-like  
1499 resonators, *Journal of Physics D: Applied Physics* 47 (4) (2013) 045307.  
1500 doi:[10.1088/0022-3727/47/4/045307](https://doi.org/10.1088/0022-3727/47/4/045307).
- 1501 [48] E. J. P. Miranda, E. D. Nobrega, A. H. R. Ferreira, J. M. C. Dos Santos,  
1502 Flexural wave band gaps in a multi-resonator elastic metamaterial plate  
1503 using kirchhoff-love theory, *Mechanical Systems and Signal Processing* 116  
1504 (2019) 480–504. doi:[10.1016/j.ymssp.2018.06.059](https://doi.org/10.1016/j.ymssp.2018.06.059).
- 1505 [49] E. J. P. Miranda Jr., E. D. Nobrega, S. F. Rodrigues, C. Aranas Jr., J. M. C.  
1506 Dos Santos, Wave attenuation in elastic metamaterial thick plates: Analytical,  
1507 numerical and experimental investigations, *International Journal of Solids and Structures* 204-205 (2020) 138–152. doi:[10.1016/j.ijsolstr.2020.08.002](https://doi.org/10.1016/j.ijsolstr.2020.08.002).
- 1510 [50] S. Lee, M. Ruzzene, Wave propagation control in thin elastic plates using

- 1511 elastic metasurfaces, Journal of Sound and Vibration 340 (2015) 142–155.  
1512 doi:[10.1016/j.jsv.2014.07.011](https://doi.org/10.1016/j.jsv.2014.07.011).
- 1513 [51] M. Yao, Y. Chen, G. Huang, Elastic metamaterial plates for flexural wave  
1514 attenuation in aerospace applications, Applied Physics Letters 104 (2014)  
1515 191903. doi:[10.1063/1.4878786](https://doi.org/10.1063/1.4878786).
- 1516 [52] B. Zouari, S. Guenneau, F. Zolla, Experimental demonstration of a two-  
1517 dimensional elastic metamaterial barrier for vibration isolation, Physical  
1518 Review Applied 10 (2018) 014021. doi:[10.1103/PhysRevApplied.10.014021](https://doi.org/10.1103/PhysRevApplied.10.014021).
- 1519 [53] T. Wang, W. Zhang, X. Wei, Design and characterization of passive acous-  
1520 tic panels using locally resonant metamaterials, Applied Acoustics 159  
1521 (2020) 107053. doi:[10.1016/j.apacoust.2019.107053](https://doi.org/10.1016/j.apacoust.2019.107053).
- 1522 [54] D. Torrent, A. Pujol, J. Sánchez-Dehesa, Acoustic metamaterials for sound  
1523 focusing and active control application, New Journal of Physics 15 (2013)  
1524 043046. doi:[10.1088/1367-2630/15/4/043046](https://doi.org/10.1088/1367-2630/15/4/043046).
- 1525 [55] O. Lera, F. Castañeda, F. Vasquez, Adaptive metamaterial plate with  
1526 embedded piezoelectric shunts for vibration control, Smart Materials and  
1527 Structures 28 (2019) 045013. doi:[10.1088/1361-665X/ab0421](https://doi.org/10.1088/1361-665X/ab0421).
- 1528 [56] K. Y. Lee, W. Jeon, Hierarchical phononic crystals for filtering multiple  
1529 target frequencies of ultrasound, Scientific Reports 10 (2020) 8070. doi:  
1530 [10.1038/s41598-020-64234-7](https://doi.org/10.1038/s41598-020-64234-7).
- 1531 [57] J. Jiang, X. Yang, Y. Hu, A novel auxetic acoustic metamaterial plate  
1532 with tunable bandgap, Applied Physics Letters 121 (8) (2022) 081702. doi:  
1533 [10.1063/1.470414](https://doi.org/10.1063/1.470414).
- 1534 [58] V. F. Dal Poggetto, F. Bosia, M. Miniaci, N. M. Pugno, Band-gap enhance-  
1535 ment in periodic frames using hierarchical structures, International Jour-  
1536 nal of Solids and Structures 216 (2021) 68–82. doi:[10.1016/j.ijsolstr.2021.01.003](https://doi.org/10.1016/j.ijsolstr.2021.01.003).

- 1539 [59] N. Kumar, S. Pal, Low frequency and wide band gap metamaterial with  
1540 divergent shaped star units: Numerical and experimental investigations,  
1541 Applied Physics Letters 115 (25) (2019) 254101. doi:10.1063/1.5119754.
- 1542 [60] Q. Wang, J. Li, Y. Zhang, Y. Xue, F. Li, Bandgap properties in meta-  
1543 material sandwich plate with periodically embedded plate-type resonators,  
1544 Mechanical Systems and Signal Processing 151 (2021) 107375. doi:10.  
1545 1016/j.ymssp.2020.107375.
- 1546 [61] G. Yan, H. Zou, S. Wang, W. Zhang, Topology optimization of thin elas-  
1547 tic metamaterial plates for ultrawide flexural vibration bandgaps, Journal  
1548 of Sound and Vibration 512 (2022) 116467. doi:10.1016/j.jsv.2021.  
1549 116467.
- 1550 [62] J. Li, X. Fan, F. Li, Numerical and experimental study of a sandwich-like  
1551 metamaterial plate for vibration suppression, Composite Structures 238  
1552 (2020) 111969. doi:10.1016/j.compstruct.2020.111969.
- 1553 [63] X.-S. Wei, Z. Wu, G. Yan, W. Zhang, Investigations on impedance mis-  
1554 match and modal coupling in multilayer resonator metamaterial plates,  
1555 Applied Acoustics 185 (2021) 108342. doi:10.1016/j.apacoust.2021.  
1556 108342.
- 1557 [64] SAE International, Composite Materials Handbook-17, Volume 2: Polymer  
1558 Matrix Composites Materials Properties, revision g Edition, SAE Interna-  
1559 tional, Warrendale, PA, 2012, cMH-17-2G.